UNIVERSIDADE FEDERAL DO CEARÁ
CENTRO DE CIÊNCIAS
DEPARTAMENTO DE FÍSICA
PROGRAMA DE PÓS-GRADUAÇÃO EM FÍSICA

CÁSSIO CÉSAR SILVA SOARES

ELECTRON-PHONON COUPLING IN LOW-DIMENSIONAL METAL HALIDE PEROVSKITES

FORTALEZA
2026

CÁSSIO CÉSAR SILVA SOARES

ELECTRON-PHONON COUPLING IN LOW-DIMENSIONAL METAL HALIDE PEROVSKITES

Ph.D. thesis presented to the Graduate Program in Physics of the Federal University of Ceará as part of the requisites for obtaining the Degree of Doctor in Physics. Concentration area: Condensed Matter Physics.

Advisor: Prof. Dr. Carlos William de Araújo Paschoal.
Co-advisor: Prof. Dr. Jose Antonio Souza.

FORTALEZA
2026

CÁSSIO CÉSAR SILVA SOARES

ELECTRON-PHONON COUPLING IN LOW-DIMENSIONAL METAL HALIDE PEROVSKITES

Ph.D. thesis presented to the Graduate Program in Physics of the Federal University of Ceará as part of the requisites for obtaining the Degree of Doctor in Physics. Concentration area: Condensed Matter Physics.

Approval date: 24/04/2026

THESIS COMMITTEE

_____
Prof. Dr. Carlos William de Araújo Paschoal (Advisor)
Universidade Federal do Ceará (UFC)

_____
Prof. Dr. Jose Antonio Souza (Co-advisor)
Universidade Federal do ABC (UFABC)

_____
Prof. Dr. Cristiano Fantini Leite
Universidade Federal de Minas Gerais (UFMG)

_____
Prof. Dr. Alejandro Pedro Ayala
Universidade Federal do Ceará (UFC)

_____
Prof. Dr. Eduardo Bedê Barros
Universidade Federal do Ceará (UFC)

Dedication

To God.

To my parents, Fernando e Vinólia.

To my fiancée, Richélita Duarte.

To all the people I love and who have shaped the person I am today.

ACKOWLEDGMENTS

First of all, I would like to thank God for everything He has helped me achieve and for giving me strength during my most difficult moments thus far.

I would like to thank my parents, Fernando and Vinólia, for the wonderful parenting and life lessons they gave me, which shaped the human being I am today, and for always believing in me, encouraging me, and helping me with the decisions I make. I love you all.

Words cannot fully express my gratitude to my fiancée, Richélita Duarte, who was a fundamental pillar in my journey during this doctorate. Thank you for all the support on the toughest days, for your understanding during my moments of absence, for supporting my decisions to follow my academic dreams, and for believing in my dreams. Thank you for always being with me and being part of yet another journey. You are an incredible partner. I love you.

I wish to express my sincere appreciation to my advisor, Prof. Dr. Carlos William, for trusting me as his student throughout my undergraduate, master's, and doctoral studies. Thank you for giving me the opportunity to learn not only about science but also about life. I will carry your advices with me forever and will be eternally grateful. I would also like to thank my co-advisor, Prof. Dr. Jose Antonio Souza, who welcomed me with open arms into his laboratory so that I could share and learn even more about research, allowing me to further evolve as a student, researcher, and person.

I would like to thank my laboratory and department colleagues, who were always very helpful and assisted me while allowing me to help with the routine research of the department. In particular, I would like to thank Juan Simón Rodríguez Hernández for all the support and conversations throughout these four years of the doctorate. Thank you very much.

I am deeply grateful to all the friends I made and kept during this journey, especially Lígia and Rômulo, who were with me through every step of my graduate studies and shared moments of joy, sadness, and, above all, happiness, making life much lighter. I love you.

I would like to extend my gratitude to the Federal University of Ceará and its Graduate Program in Physics for all the support with my studies, especially to the lab groups OPEMLab and LabCrEs from the physics department who contributed to my academic growth. Finally, I would like to thank my funding agency. This study was financed in part by the Coordenação de Aperfeiçoamento de Pessoal de Nível Superior - Brasil (CAPES) – Finance Code 001.

RESUMO

Perovskitas de haleto metálico (MHPs) são materiais versáteis e de baixo custo para aplicações optoeletrônicas como células solares e LEDs, oferecendo arquiteturas multifuncionais que aumentam a absorção óptica e a mobilidade de portadores de carga. Perovskitas de haleto metálico de baixa dimensionalidade (LDMHPs) têm ganhado bastante atenção principalmente por suas estabilidades superiores e confinamentos quânticos em nível molecular, onde restrições estruturais criam camadas bidimensionais (2D), cadeias unidimensionais (1D) ou aglomerados isolados (0D) das suas estruturas inorgânicas. A natureza "maleável" das LDMHPs facilita distorções estruturais rápidas após a excitação, à medida que os portadores de carga das quase-partículas chamadas éxcitons, formados por pares elétron-buraco ligados por forças de Coulomb, interagem com os íons da rede por meio de fônons. Essa relação é governada pelo acoplamento elétron-fônon (EPC), que gera quase-partículas chamadas polarons que ditam significativamente propriedades optoeletrônicas como a fotoluminescência (PL). Compreender os mecanismos e a força do EPC é, portanto, essencial para o desenvolvimento de materiais de alta eficiência, particularmente para fontes de iluminação de luz branca capazes de alcançar economias de energia globais substanciais. Neste contexto, esta tese foca no estudo do EPC em LDMHPs, referindo-se primariamente às suas propriedades optoeletrônicas, tais como PL a baixa temperatura. A primeira família de LDMHPs estudada foi a das perovskitas de haleto 0D A_2SnBr_6 (A = Cs, Rb). Para o composto Cs_2SnBr_6, as análises revelaram um EPC forte, conforme evidenciado por emissão de multifônons, levando a *overtones* superiores intensos até quarta ordem. Tal força do EPC foi confirmada pelo fator de Huang–Rhys S = 24,4 a partir do fenômeno de PL decorrente de éxcitons auto aprisionados (STE), com a contribuição de fônons relacionados ao estiramento assimétrico Sn–Br predominando na transição eletrônica. Além disso, para o composto Rb_2SnBr_6, medidas de PL dependentes da temperatura, complementadas por outras técnicas de caracterização e cálculos teóricos, revelaram uma emissão de banda larga com um deslocamento de Stokes significativo atribuído a estados de STE. O mecanismo de Fröhlich, mediado por interações entre portadores de carga dos éxcitons e fônons ópticos longitudinais (LO), foi o principal responsável pelo alargamento da emissão através da recombinação radiativa assistida por fônons. A força do EPC foi avaliada através do fator de Huang–Rhys S = 34, confirmando fortes correlações entre propriedades eletrônicas e vibracionais. O possível mecanismo de formação de STE foi avaliado pelo parâmetro de Fröhlich α de 2.78 para elétrons e 4.41 para buracos, o que apontou uma contribuição majoritária da quase-partícula buraco-polaron no aprisionamento de éxcitons. Por fim, a última

família de LDMHPs investigada consistiu em perovskitas de brometo de chumbo de baixa dimensionalidade com espaçadores quirais baseados em α-metilbenzilamina (MBA). Verificou-se que o uso de uma mistura racêmica desta molécula orgânica resultou em uma redução de dimensionalidade das fases 2D (R-/S-MBA)$_2$PbBr$_4$, obtidas ao usar os enantiômeros R- e S-MBA do espaçador orgânico, para a fase 1D (Rac-MBA)$_3$PbBr$_5$·H$_2$O, que exibiu um comportamento de PL diferente em comparação com as fases 2D e dois regimes de EPC com fatores de Huang–Rhys de S = 67 acima de 110 K e S = 189 abaixo deste limiar, que foram posteriormente correlacionados com o grau de distorções octaédricas da estrutura 1D inorgânica ao reduzir a temperatura. Os resultados obtidos através desta tese servem como um guia para o caminho do desenvolvimento de novos e aprimorados dispositivos e tecnologias voltados para aplicações optoeletrônicas.

Palavras-chave: perovskitas de haleto metálico; acoplamento elétron-fônon; éxcitons auto aprisionados; fatores de Huang–Rhys; distorções octaédricas.

ABSTRACT

Metal halide perovskites (MHPs) are versatile, low-cost materials for optoelectronic applications like solar cells and LEDs, offering tunable architectures that enhance optical absorption and carrier mobility. Low-dimensional metal halide perovskites (LDMHPs) have specifically gained attention for their superior stability and molecular-level quantum confinement, where structural constraints create 2D layers, 1D chains, or 0D clusters of the inorganic framework. The "soft" lattice nature of LDMHPs facilitates rapid structural distortions upon excitation as the charge carriers of the quasiparticles called excitons, formed by bound electron-hole pairs through Coulomb forces, interact with lattice ions through phonons. This relationship is governed by electron-phonon coupling (EPC), which forms quasiparticles called polarons that significantly dictate optoelectronic properties such as photoluminescence (PL). Understanding the mechanisms and strength of EPC is therefore essential for developing high-efficiency materials, particularly for white-light illumination sources capable of achieving substantial global energy savings. In this context, this thesis focuses on the study of EPC in LDMHPs, primarily concerning their optoelectronic properties, such as low-temperature PL. The first family of LDMHPs studied was the 0D halide perovskites A_2SnBr_6 (A = Cs, Rb). For Cs_2SnBr_6, the analysis revealed a strong EPC, as evidenced by multiphonon scattering, leading to intense overtones up to the fourth order. Such strength of the EPC was confirmed by the Huang–Rhys factor $S = 24.4$ from the PL phenomenon arising from self-trapped excitons (STE) with the contribution of phonon modes related to the Sn–Br asymmetric stretching predominating in the electronic transition. Furthermore, for Rb_2SnBr_6, temperature-dependent PL measurements, complemented by other characterization techniques and theoretical calculations, revealed broadband emission with a significant Stokes shift attributed STE state. The Fröhlich mechanism, mediated by interactions between excitonic charge carriers and longitudinal optical (LO) phonons, primarily accounted for the emission broadening through phonon-assisted radiative recombination. The EPC strength was evaluated through the Huang–Rhys factor $S = 34$, confirming strong correlations between electronic and vibrational properties. The possible mechanism of STE formation was evaluated by the Fröhlich parameter α of 2.78 for electrons and 4.41 for holes, which pointed out a major contribution of the hole-polaron quasiparticle on exciton trapping. Finally, the last family of LDMHPs investigated consisted of low-dimensional lead bromide perovskites with chiral spacers based on α-methylbenzylamine (MBA). It was found that the use of a racemic mixture of this organic molecule yielded a reduction of dimensionality from the 2D (R-/S-MBA)$_2$PbBr$_4$, obtained when

using the enantiomers R- and S-MBA of the spacer, to the 1D (Rac-MBA)$_3$PbBr$_5$·H$_2$O phase, which exhibited a different PL behavior compared to the 2D phases and two regimes of EPC with Huang–Rhys factors of S = 67 above 110 K and S = 189 below this threshold that were further correlated with the degree of octahedra distortions of the inorganic framework upon lowering temperature. The results obtained through this thesis pave the way for developing new and improved devices and technologies towards optoelectronic applications.

Keywords: metal halide perovskites; electron-phonon coupling; self-trapped excitons; Huang–Rhys factors; octahedra distortions.

LIST OF FIGURES

LIST OF TABLES

TABLE OF CONTENTS

1 INTRODUCTION

Metal halide perovskites (MHPs) have emerged as promising, versatile, and low-cost solutions for a variety of optoelectronic applications such as solar cells, photodetectors, light-emitting diodes (LEDs), spintronics, and scintillators [1–4]. These compounds comprise a vast combination of different elements and dimensionalities, as well as intriguing architectures that can boost optical absorption in the ultraviolet-visible-infrared range [5,6]. These features are relevant for applications concerning sunlight as an energy source and applications relying on quantum and dielectric confinements, carrier mobility, structural stability, and enhanced efficiency. Consequently, MHPs often surpass the performance of the most widely used optoelectronic devices commercially available [7,8].

The perovskite structure is characterized by the general formula ABX_3, where the A element occupies the cavities formed by a network of corner-sharing BX_6 octahedra [9], as shown in Figure 1. The term "perovskite" was first introduced in 1839 by Gustav Rose for the mineral $CaTiO_3$, which he named in honor of the mineralogist Count Lev Alekseyevich von Perovski. In 1926, Victor Goldschmidt extended the term to a general denotation for the crystal structure group. [10]. In the case of the most common MHPs, the A element denotes a monovalent organic molecule or inorganic alkali metal cation such as Cs^+, Rb^+, $CH_3NH_3^+$ (MA^+), and $CH(NH_2)_2^+$ (FA^+). The B element represents a divalent metal cation, such as the popular Pb^{2+} and Sn^{2+}, and the X element consists of the Cl^-, Br^-, I^-, and F^- halide anions [11].

Figure 1 – Standard aristotype cubic perovskite evidencing all atoms (left) and the BX_6 octahedral framework (right)

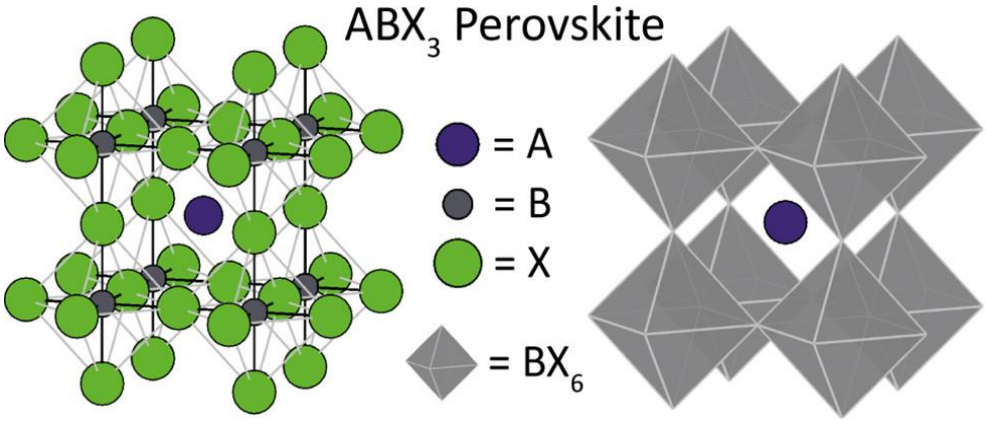

Source: adapted from reference [9].

The aristotype perovskite structure belongs to the cubic symmetry system, where the undistorted octahedra form a cuboctahedral space filled by the A element [9]. However, most perovskites possess a variety of polymorphs with reduced symmetries, which depend on the degree of octahedral tilting [12]. The ABX_3 perovskite structure can be geometrically predicted based on the ionic radii of its constituents through the Goldschmidt tolerance factor t [13,14]:

$$t = \frac{R_A + R_X}{\sqrt{2}(R_B + R_X)}. \quad (1)$$

In the Equation (1), R_A stands for the ionic radii of the A element, whereas R_B and R_X are the analogs for the B and X elements, respectively, as illustrated in Figure 2(a). The Goldschmidt tolerance factor is a century-old metric and has been used to assess phase stability, in which a perovskite structure is expected to be stable if t falls approximately in the range of $0.7 < t < 1$, although modifications to the tolerance factor have been made over time to account for cases where the factor failed to predict stable perovskites [14,15]. In any case, the size of the perovskite's constituents is essential in determining the symmetry of a given perovskite structure, especially when the halide anion is switched fully or partially (Figure 2(a)), as the optoelectronic properties and phase stability of MHPs depend on the choices made regarding anion exchange [16,17]. Another important factor in the crystal structure adopted by these systems concerns the temperature range, as illustrated in Figure 2(b). Perovskites tend to achieve different octahedral configurations as lattice contraction decreases the interatomic distance. This lowers the packing efficiency of ions, resulting in tilted octahedron configurations to maintain a stable corner-sharing octahedra framework. A further decrease in temperature can disrupt the octahedral connectivity in one or more directions, resulting in non-perovskite structures with a loss of octahedral bonding [18,19].

Figure 2 – (a) Archetypal cubic perovskite, which has $t = 1$, and anion exchange for ABX_3 perovskites that can introduce octahedral tilts to accommodate a pseudocubic distorted perovskite structure with t smaller than unity. (b) Schematic of reversible phase transitions in polymorphic perovskites, from pseudocubic structures consisted of octahedral tilting to a non-perovskite structure formed through bond breaking. (c) Overview of group-subgroup symmetries of tilted halide perovskites and some examples concerning the $APbX_3$ (A = MA, FA, and Cs; X = Cl, Br, and I), and $CsSnX_3$ (X = Cl, Br, and I) perovskites with comparison to the archetypal $CaTiO_3$ structure. The octahedra distortions are identified using Glazer's notation and the dashed lines indicate first-order transitions

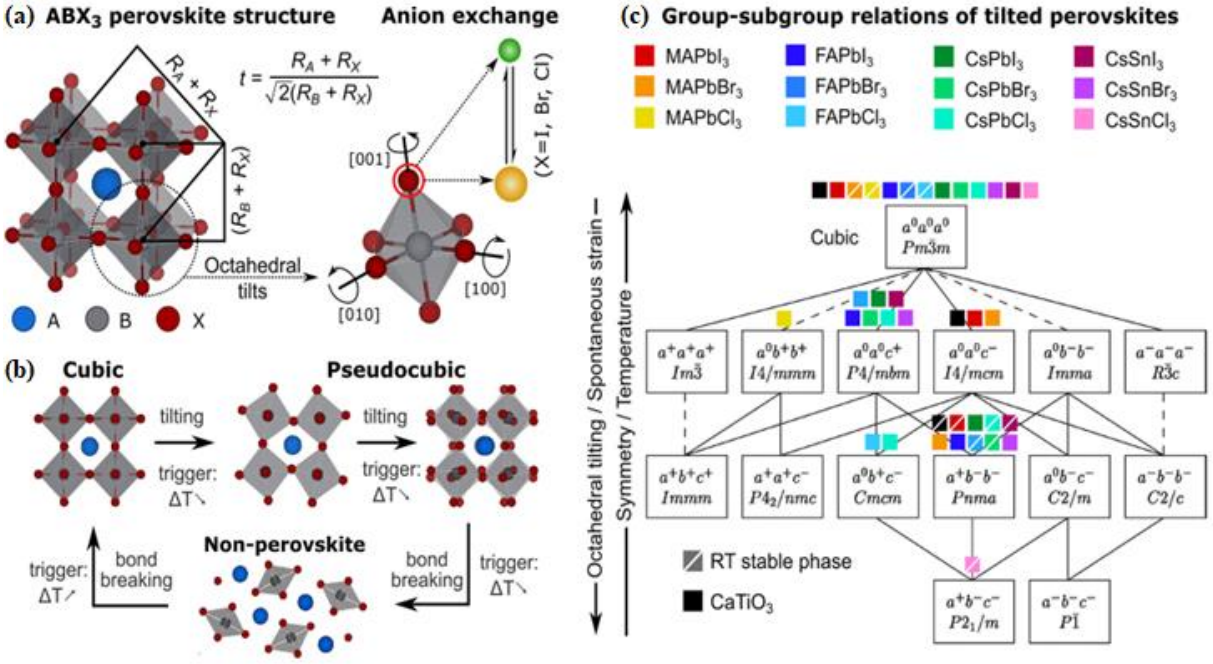

Source: adapted from reference [17].

Figure 2(c) shows an overview of 15 possible space groups in which a perovskite with tilted octahedra can be stabilized (tilted perovskites), along with their group-subgroup symmetries [17]. Octahedral distortions can modify the properties of perovskites, which makes an understanding of the structure, constituent elements, and temperature range essential. The Glazer's notation is used to classify the octahedral distortions, and some examples of MHPs are presented in comparison with the archetypal $CaTiO_3$ perovskite. Among the examples of perovskites shown in Figure 2(c), lead halide perovskites based on methylammonium (MA) and formamidinium (FA) have been used as the photoactive layer in solar cells with impressive power conversion efficiencies (PCE) surpassing those of commercially available silicon solar cells due to their high absorption coefficient and carrier mobility [20–22]. However, poor long-

term stability to light and moisture limits their commercial use [23,24]. Tin-based MHPs have been used as an alternative to replace the Pb metal cation because of its toxicity, although they achieve lower PCEs and present an additional concern regarding synthesis routes related to the Sn^{2+} cation that can easily oxidizes to Sn^{4+} upon exposure to air, which can result in non-perovskite structures with isolated octahedra that significantly reduce carrier mobility [25,26]. Cs-based lead halide perovskites have been applied successfully in photocatalysis and photodetector devices, as their increased stability compared to hybrid organic-inorganic perovskites (HOIPs), together with broad absorption in the solar spectrum range, makes them suitable for such applications [27,28].

MHPs have also attracted significant attention due to the phenomenon of exciton photoluminescence (PL), where photoexcited electrons and holes interacting through Coulomb forces that can undergo radiative recombination. A well-known example can be cited concerning the work of Protesescu *et al*. on tunable optical absorption and PL achieved by anion exchange in $CsPbX_3$ nanocrystals [16], as shown in Figures 3(a,b). As previously commented, halide switching can modify the emission properties of perovskites, which can cover the entire visible spectrum, as well as tune the optical absorption bandgap, which is attractive for device applications (Figure 3(c)). Additionally, unlike bulk compounds, reducing the size and morphology of the perovskites to quantum dots (QDs), nanocrystals, nanorods, and nanoplatelets can introduce quantum-size effects due to quantum confinement [29,30]. This also results in higher PL quantum yield (PLQY, the rate of emitted to absorbed photons) and longer PL lifetimes (Figure 3(d)) [31]. Taken together, quantum confinement and perovskite composition are versatile parameters that can be used to control different emission behaviors for a variety of applications such as LEDs, scintillators, lasers, and radiation detectors [32–34].

Figure 3 – (a) Colloidal solutions of $CsPbX_3$ nanocrystals (X = Cl, Br, and I) in toluene under UV excitation. (b) Normalized PL spectra of the samples. (c) Tunable absorption and PL spectra of the perovskites. (d) Time-resolved PL decays for the $CsPbX_3$ nanocrystals

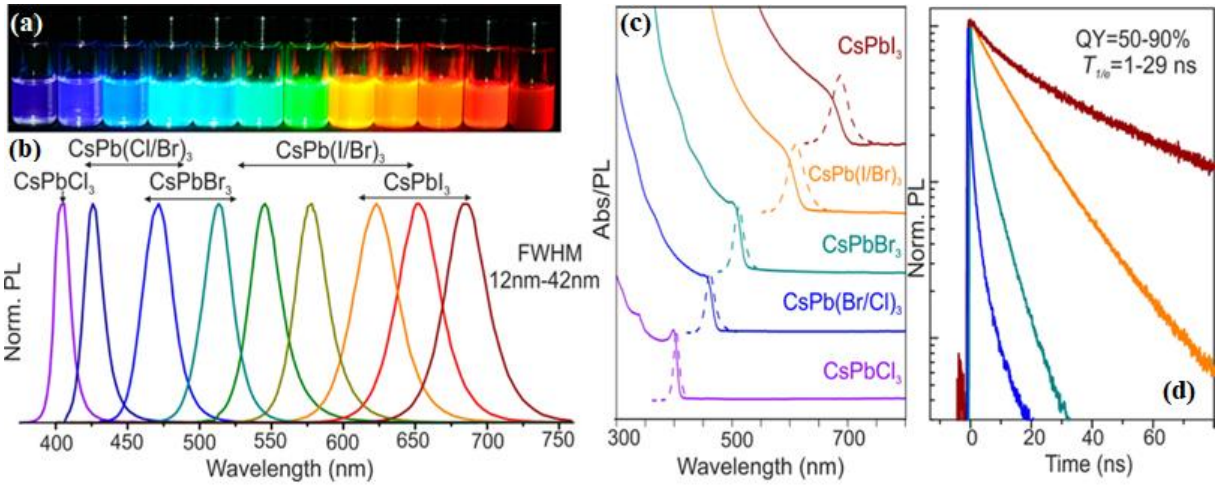

Source: adapted from reference [16].

Common approaches to control and modify the PL profile of MHPs include doping, particularly with a metal ion at the B-site of the ABX_3 structure [35,36], and the control of defects both within the bulk and on the surface [37,38]. These modifications introduce traps for capturing charge carriers or excitons (which are neutral quasiparticles), which modify the emission energies and dynamics. However, MHPs tend to have poor stability under exposure to light and moisture, as humidity and photoexcitation can induce the reduction of the B^{2+} cation to metallic B^0 and trigger bond breaking especially for HOIPs, resulting in halide salts BX_2 and AX with subsequent degradation of the organic product by interaction with oxygen [39–41]. Additionally, the stability of the organic surfactants needed to stabilize reduced-size morphologies also presents intriguing problems in achieving quantum-confined configurations, as light and heat can break the surfactant bonds and modify the anion composition of the perovskites [42,43]. Consequently, the choice of the most stable surfactants for nano-sized MHPs is still under debate.

Low-dimensional metal halide perovskites (LDMHPs) have gained much attention as an alternative to obtain both quantum confinement effects and better stability [44,45]. LDMHPs are characterized by quantum confinement at the molecular level rather than a morphological one, where the octahedral connections are broken in one or more directions, resulting in structures consisting of two-dimensional (2D) layers, one-dimensional (1D) chains, and zero-dimensional (0D) clusters of metal halide octahedra frameworks, as illustrated in Figure 4 [46–48]. They are not perovskites in the sense that they generally do not follow the

ABX_3 stoichiometry and do not have connected corner-sharing octahedra in all directions (3D). However, the term “perovskite” was historically misused and has been accepted to denominate these structures due to their similarities with the truly MHPs [9,49]. The low dimensionality is often achieved by using large organic molecules in the A-site, also known as organic spacers, or through the aid of metals within the B-site with different oxidation states than the commonly used divalent cations. This results in stronger hydrogen bonding between the organic molecules and the BX_6 octahedra, while also promoting a wrapped and protected layer that prevents octahedral dissociation upon exposure to air and light [45,50].

Figure 4 – Representative structures of 3D MHPs, 2D, 1D, and 0D LDMHPs and their typical PL spectra (left). Commonly used elements in MHPs and LDMHPs structures (right)

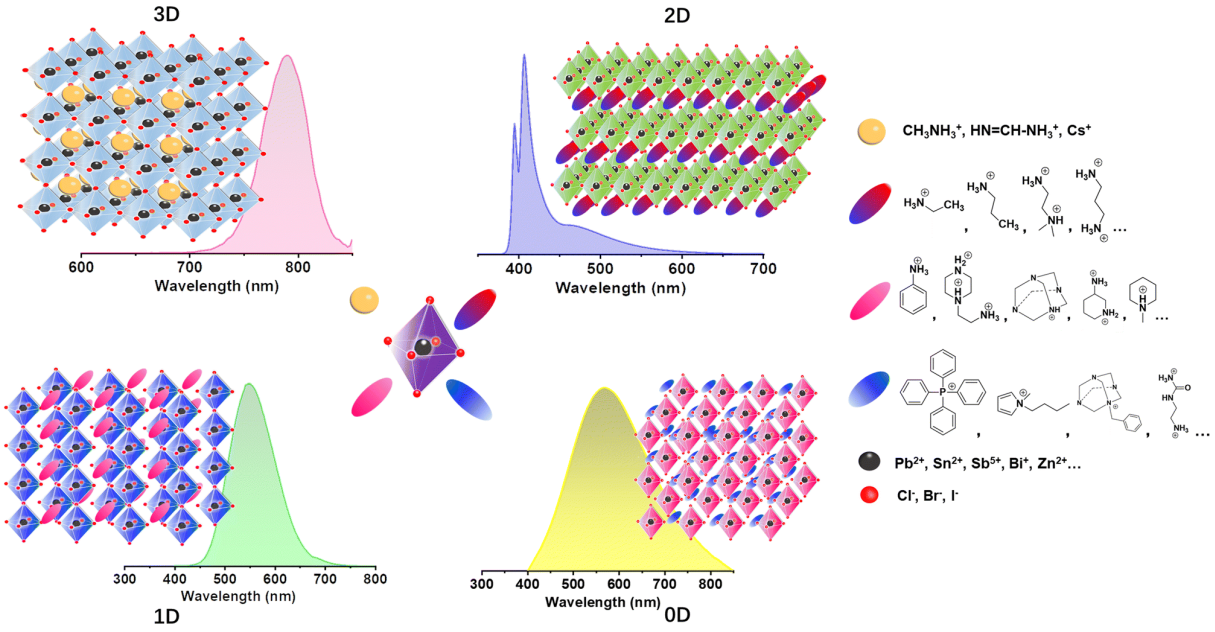

Source: adapted from reference [48].

This molecular engineering of the dimensionality promotes quantum confinement by restricting excitons within the octahedra framework, and increases their binding energy preventing dissociation at room temperature, which is feature desirable for devices operating under ambient conditions [51]. Furthermore, the soft nature of LDMHPs facilitates ultrafast structural distortion upon optical excitation, as the electrons and holes of the excitons interact with the lattice ions [52,53]. This induced-distortions can, in turn, interact with the exciton, and this interplay is reflected in changes to the PL linewidth that differ from the narrow emissions seen in 3D MHPs, as shown schematically in Figure 4. In some cases, where the interaction between the exciton’s charge carriers and the lattice distortions are particularly strong, the

distorted lattice can trap excitons in highly localized self-trapped exciton (STE) states [48,54,55]. These states exhibit characteristic broadband PL with a large Stokes shift, such as the representative 0D case illustrated in Figure 4.

The fundamental key to the interaction between excitons and lattice distortions, as well as their impact on PL emission, lies in the concept of electron-phonon coupling (EPC), which describes the mutual interaction between electrons and lattice vibrations [56–58]. This coupling creates a quasiparticle known as a polaron, that can be conceptualized as an electron moving within a phonon cloud, and can significantly influences the optoelectronic properties of LDMHPs by modifying the mass, mobility, and relaxation rate of photoexcited carriers [59–61]. Many authors employ the term “exciton-phonon coupling” to address the electron- and hole-phonon coupling of an exciton within the lattice, while others prefer to distinguish between electron-phonon and hole-phonon couplings when individual treatment is required. Here, EPC is used as a general term to all cases, unless specific distinction is necessary. Understanding the mechanisms and strength of EPC in LDMHPs is crucial for the deployment of these materials in optoelectronic devices involving PL phenomena, particularly for more efficient white-light illumination sources that could enable substantial energy savings in the current global scenario, where nearly 20% of electricity is consumed by lighting [55,62]. In this context, this thesis is structured as follows: Chapter 2 provides a brief review of polarons and EPC, alongside methods for quantifying the EPC strength through optoelectronic measurements. Chapter 3 describes the methodology used for sample preparation and characterization techniques in detail. Chapter 4 investigates the 0D halide perovskite family A_2SnBr_6 (A = Cs, Rb), using both experimental and theoretical approaches, focusing on the origin and strength of EPC, as well as its impacts upon the low-temperature PL properties of both compounds. Chapter 5 examines LDMHPs with chiral organic cations based on α-methylbenzylamine in the form of (R-/S-MBA)$_2$PbBr$_4$ and (Rac-MBA)$_3$PbBr$_5$·H$_2$O where the use of a racemic mixture led to dimensionality reduction and tunable optoelectronic properties, with particular STE emission with different EPC regimes investigated by structural and optoelectronic properties at low-temperatures. Finally, Chapter 6 presents the overall conclusions made throughout all the LDMHPs investigated concerning the EPC for each compound.

2 CARRIER-LATTICE INTERACTIONS AND EMISSION FEATURES

In the context of EPC in LDMHPs, polaron formation is typically classified by the range of interaction between electrons and lattice distortions. These are categorized as either large or small polarons, as illustrated in Figure 5. Large polarons involve long-range interactions where electrons couple with phonons across several lattice sites. In this case, the polaron is spatially extended, resulting in a more delocalized electronic state where carrier mobility is dominated by coherent transport. Conversely, small polarons are characterized by short-range interactions where the electron-induced lattice deformation induces a local shift in the band structure, leading to a localized state where mobility is governed by incoherent hopping [56,59,60].

Figure 5 – Isosurfaces of polaron densities in two-dimensional models for (a) large and (b) small polarons, showing their spatial extents relative to the lattice units

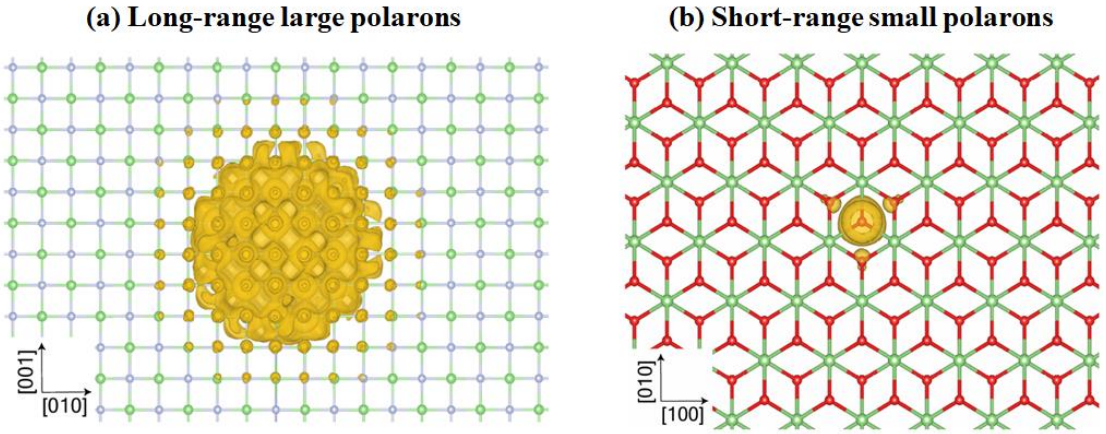

Source: adapted from reference [59].

Long-range interactions in LDMHPs are best described by the Fröhlich model, which occurs in ionic crystals and polar semiconductors with an ionic contribution to lattice energy, as for the bonding between metal cations and halide anions within the octahedral framework where optoelectronic phenomena take place [63]. The model is based on the long-range macroscopic electric field induced by long-wavelength longitudinal optical (LO) phonons [59,64]. As an electron moves, this electric field polarizes the surrounding lattice. The resulting polarization and charge carrier then travel together as a large polaron. Within this framework, the EPC strength is characterized by the dimensionless Fröhlich coupling constant, α, defined as [65]:

$$\alpha = \frac{e^2}{4\pi\varepsilon_0\hbar}\left(\frac{1}{\varepsilon_\infty} - \frac{1}{\varepsilon_s}\right)\sqrt{\frac{\bar{m}}{2\hbar\omega_{LO}}}, \tag{2}$$

where, in Equation (2), e is the electron charge, ħ is the reduced Planck constant, ε_0 is the vacuum permittivity, and $\bar{m}$ is the effective mass of the electron in the case of no interaction with phonons (bare band mass). The term ω_{LO} represents the characteristic LO phonon angular frequency, while ε_∞ and ε_s are the optical and static dielectric constants, respectively. The expression $(\varepsilon_\infty^{-1} - \varepsilon_s^{-1})$ accounts for the contribution of the ionic polarization arising from the vibration of ions that can interact with the electron in the lattice [64]. Weak EPC regimes are characterized by $\alpha \ll 1$, whereas very strong couplings typically fall within the $\alpha > 8$ range [66], and both the polaron energy shift Δ_p upon the bare electron energy and the polaron mass $\bar{m}_p$ are functions of α. For instance, in an intermediate coupling regime, $\Delta_p \approx -\alpha\hbar\omega_{LO}$ and $\bar{m}_p \approx (1 + 0.17\alpha + 0.025\alpha^2)m_0$, where m_0 is the electron rest mass [56]. The same theory applies equally to hole-phonon interactions by substituting the hole effective mass $\bar{m}$ and to obtain its corresponding Fröhlich constant.

The size of the polarization-deformed region that follows the electron in the polaron scenario is quantified by the polaron radius $r_p = (2\bar{m}\omega_{LO}\hbar^{-1})^{-\frac{1}{2}}$, which typically ranges from 1 – 1.5 nm, covering few lattice sites in a way that the Frohlich effectively describes long-range interactions using a dielectric continuum approach [64]. However, when the electron-induced lattice distortion is confined within a single lattice site, the continuum model fails to accurately describe the charge-lattice interaction and, in this regime, small polaron formation occurs via short-range interactions with acoustic phonons, triggering a local change in the band structure called deformation potential and the related energy shift δE is given by $\delta E = \Xi\nabla\boldsymbol{\xi}(\boldsymbol{r})$, where Ξ is the deformation potential constant and $\boldsymbol{\xi}(\boldsymbol{r})$ represents the local displacement in terms of the acoustic phonons at a position $\boldsymbol{r}$ in the lattice [67,68]. The deformation potential serves as a metric for the strength of short-range interactions of EPC in the small polaron case and, as with the Fröhlich model, it can be extended to the case of hole-phonon couplings where the carriers possess their respective values of Ξ, although theoretical and experimental calculations of this parameter are not straightforward [66,69].

In the case of excitons in LDMHPs, polaronic contributions affect exciton dynamics by screening the Coulombic attraction between electron-hole pairs. Combined with

the quantum confinement of the low-dimensionality, these interactions directly influence the exciton binding energy [70]. Furthermore, the coupling between the exciton's charge carriers and the lattice can shift the excited-state equilibrium position prior to recombination, resulting in a Stokes shift between the absorption and emission spectra [71]. Two primary mechanisms govern the broadening exciton emission linewidth, namely inhomogeneous and homogeneous broadening, the latter of which is fundamentally driven by polaronic effects.

Inhomogeneous broadening is related to the scattering between excitons and imperfections, such as external strain and defects, which are generally temperature-independent and contribute a constant term Γ_0 to the full width at half maximum (FWHM) of the emission profile [72]. Another source of inhomogeneous broadening involves ionized impurity donors or acceptors interacting with excitons. These ionized impurities provide a temperature-dependent contribution to the FWHM in the form $\Gamma_{imp} e^{-\frac{E_{imp}}{k_B T}}$ where k_B is the Boltzmann constant, T is the temperature, Γ_{imp} is a constant, and E_{imp} is the average binding energy of the impurities [73]. As said, these inhomogeneous contributions are extrinsic to the system, and they typically provide only minor contributions to the emission linewidth in high-purity samples.

The homogeneous contribution arises from the scattering of charge carriers with phonons through polaronic effects. This process involves both acoustic and LO phonons, and their contributions are proportional to the phonon population density defined by the Bose–Einstein distribution function $N(T) = \left(e^{\frac{\hbar\omega}{k_B T}} - 1\right)^{-1}$ for the corresponding phonon with angular frequency ω. For instance, the contribution from scattering with LO phonons is expressed as $\Gamma_{LO}\left(e^{\frac{\hbar\omega_{LO}}{k_B T}} - 1\right)^{-1}$, where Γ_{LO} is a constant representing the coupling between excitons and LO phonons through long-range Fröhlich interactions with a complex dependence on several parameters including ω_{LO}, $(\varepsilon_\infty^{-1} - \varepsilon_s^{-1})$, and the effective masses $\bar{m}_e$ and $\bar{m}_h$ of electron and hole, respectively [66,74]. Scattering with acoustic phonons follows a similar functional form. However, within a typically observable temperature range, acoustic phonons have significantly lower energies than $k_B T$, and a linear dependence on temperature is generally assumed from the phonon population density with resulting contribution given by $\Gamma_{ac} T$, where Γ_{ac} is a constant representing the short-range interactions which depends on quantities such as the acoustic phonon frequency, elastic constants, $\bar{m}_e$, $\bar{m}_h$, elastic constants, and the deformation potentials Ξ_e and Ξ_h of the electron and hole, respectively [66,75]. Together, the

inhomogeneous and homogeneous contributions define the temperature dependence of the exciton emission FWHM as follows [74]:

$$FWHM(T) = \Gamma_0 + \Gamma_{ac}T + \frac{\Gamma_{LO}}{e^{\frac{E_{opt}}{k_BT}} - 1} + \Gamma_{imp}e^{-\frac{E_{imp}}{k_BT}}, \quad (3)$$

with $E_{opt} = \hbar\omega_{LO}$. Equation (3) reflects all extrinsic contributions from inhomogeneous broadening caused by local variations in electronic properties across the lattice, and also accounts for intrinsic contributions from homogeneous broadening due to phonon scattering within the intra- and interband interactions of the exciton band [75]. In LDMPHs, general exciton creation and recombination follow the scheme shown in Figure 6. Upon excitation near or above the bandgap energy (upward purple arrow), electrons and holes are created in the conduction band (CB) and valence band (VB), respectively. These carriers interact through Coulomb forces, while polaronic effects on both particles relax the exciton into a lower energy free exciton (FE) state [76,77]. After, they can recombine radiatively with a narrow and small Stokes shifted emission (downward green arrow) [78].

Figure 6 – Exciton's luminescence phenomena, including free electron (e^-) and hole (h^+) carriers upon excitation, FE states of bonded electron-hole pairs and STE states in the lowest energy level

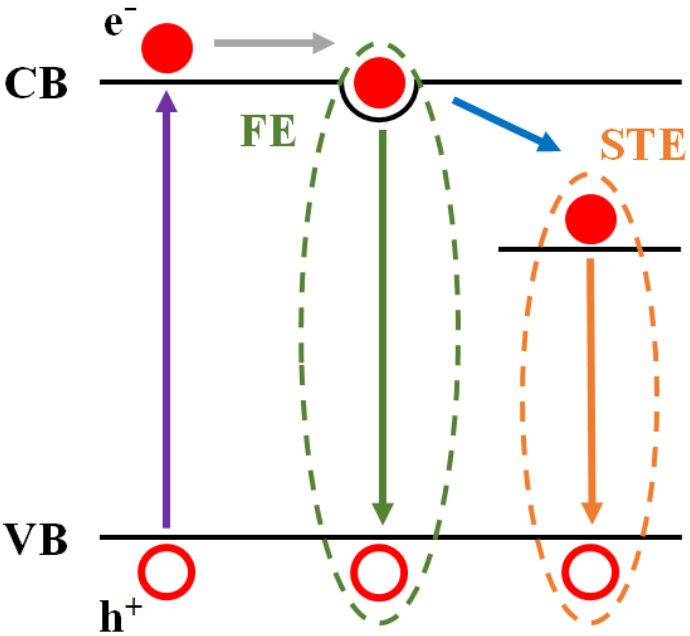

Source: elaborated by the author.

As mentioned in the previous chapter, if the interaction between exciton carriers and the lattice is sufficiently strong, electrons and holes can distort the lattice and trap the exciton in an even lower state called a self-trapped exciton (STE) [48]. The STE can undergo radiative recombination (downward orange arrow) which results in a large Stokes shifted and broad emission, followed by lattice relaxation. While EPC is always present during STE formation, other factors also influence self-trapping. These include extrinsic factors such as dopants and defects related to ion vacancies [79–81], external parameters like the conversion between FE and STE under varying temperature and pressure [82,83], and intrinsic features such as the degree of octahedral distortion, which promotes a favorable environment for self-trapping [84,85].

Usually, the STE mechanisms in LDMHPs rely on the trapping of one or both exciton carriers and, for this to occur, long- and short-range interactions must act together, although Fröhlich interactions typically provide the larger contribution. Upon excitation, B-X and X-X bonds between the metal B and halide X ions can become shorter, which can promote hole trapping, while the shortening of B-B bonds can induce electron trapping [48,86]. Regardless of which exciton carrier is trapped, the nature of an STE is similar to an electron trapped in a defect which, in this case, would be the localized distortion created by the carrier around the shortened bonds. This allows the interpretation of the STE recombination mechanism using a configuration coordinate diagram in a semiclassical model, similar to the theory of absorption and emission for a localized color center, as schematically represented in Figure 7 [64,66]. The nuclear coordinate Q represents a general coordinate associated with the displacements of ions related to a normal mode of vibration (phonon), which can be approximated as a classical harmonic oscillator with angular frequency ω and mass m around the equilibrium position. Through the Born-Oppenheimer approximation, the ions of the lattice are much heavier and move much slower than the electrons. Therefore, the solution of the Hamiltonian for a system consisting of electrons and ions can be separated into a solution for the electrons at a fixed ionic position and a solution for the ions moving on the adiabatic potential $W(Q)$ which consists of the sum of the electronic energy and the interaction potential between ions [66]. In this way, the curves $W_g(Q)$ and $W_{st}(Q)$ represent the system in the ground and STE states, respectively, where the electrons rapidly reorganize for each ionic position.

Figure 7 – Adiabatic potentials of the self-trapped and ground states related to STE emission mechanisms with vertical transitions following the Franck–Condon principle

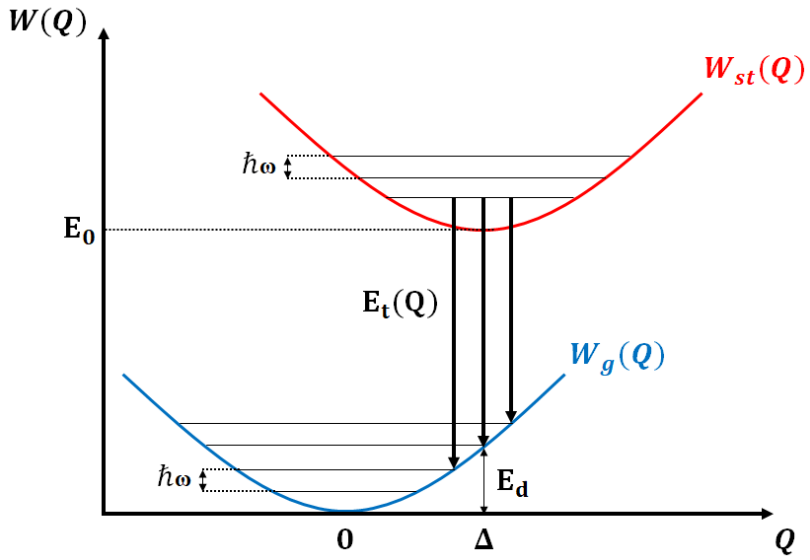

Source: elaborated by the author.

For the ground state where there is no distortion ($Q = 0$), $W_g(Q)$ can be approximated near the equilibrium point as $W_g(Q) = m\omega^2 Q^2/2$ ((setting the minimum energy to zero for simplicity). In the STE state, due to distortions, the new energy minimum is located at a new equilibrium position Δ such that $W_{st}(Q) = E_0 + m\omega^2(Q - \Delta)^2/2$, where E_0 is the energy difference between the minima of $W_g(Q)$ and $W_{st}(Q)$. According to the Franck–Condon principle [64], since electrons move much faster than ions, electronic transitions between $W_g(Q)$ and $W_{st}(Q)$ occur without an appreciable change in the ionic positions and represented vertically for a given Q. Thus, the transition energy $E_t(Q)$ between the STE state and the ground state is given as

$$E_t(Q) = W_{st}(Q) - W_g(Q) = E_0 + \frac{m\omega^2\Delta^2}{2} - m\omega^2\Delta Q. \quad (4)$$

The energy $W_g(\Delta) = m\omega^2\Delta^2/2$ of the ground state at which the transition from the STE state's energy minimum occurs is the lattice deformation energy E_d, which arises from the effect of the lattice distortions upon the ground state [66]. The variance σ_t^2 of the emission energy is therefore given by the variance of $E_t(Q)$, such that

$$\sigma_t^2 = \overline{E_t(Q)^2} - \left(\overline{E_t(Q)}\right)^2 = 2m\omega^2 E_d \sigma_Q^2, \tag{5}$$

where $\sigma_Q^2 = \overline{Q^2} - (\bar{Q})^2$ is the variance of Q. In the quantum harmonic oscillator representing $W_g(Q)$, the eigenstates are characterized by the index n (n = 0, 1, 2, 3, …) with respective energies $E_n = \hbar\omega\left(n + \frac{1}{2}\right)$. For a given quantum state, $\bar{Q} = 0$ as the system has an equal probability of being found at displacements Q and $-Q$, while $\overline{Q^2} = \hbar\left(n + \frac{1}{2}\right)/(m\omega)$. At $W_g(\Delta) = E_d$ after emission, the system relaxes to the minimum energy $W_g(0)$ through phonon emissions, where the average number S of emitted phonons is such that $E_d = S\hbar\omega$. Here, S is the Huang–Rhys factor, a metric to the EPC that quantifies the degree of lattice distortion ($S \propto \Delta^2$) in the case of exciton self-trapping and represents the coupling strength of the phonons with the STE [66,87]. Generally, $S \leq 1$ refers to a weak coupling regime, whereas $S \geq 20$ is considered a strong EPC case [64].

Taking all the above results together, it is found that $\sigma_t^2 = S(\hbar\omega)^2(2n + 1)$. However, in the case of finite temperatures, the thermal average $\langle\sigma_t^2\rangle$ of the emission energy variance depends on the average number of phonons $\langle n\rangle$ at a given temperature, which is given by the Bose–Einstein distribution function $\langle n\rangle = N(T)$. Therefore:

$$\langle\sigma_t^2\rangle = S(\hbar\omega)^2(2\langle n\rangle + 1) = S(\hbar\omega)^2\left(\frac{2}{e^{\frac{\hbar\omega}{k_B T}} - 1} + 1\right) = S(\hbar\omega)^2 \coth\left(\frac{\hbar\omega}{2k_B T}\right). \tag{6}$$

At zero temperature, the emission spectrum $F(E)$ consists of the superposition of many individual emissions centered at $E_0 - n\hbar\omega$ with intensities proportional to the Franck–Condon factors $e^{-S}S^n/n!$ [87] in such a way that

$$F(E) = e^{-S}\sum_n \frac{S^n}{n!} f\left(E, n, \sigma_{ph}\right), \tag{7}$$

where $f(E, n, \sigma)$ is a function of E, n, and the broadening σ_{ph} of each individual emission. In the case of strong coupling (large S) and for $T > 0$, Toyozawa [66,88] showed that the emission spectra are independent of the lineshape of the individual emissions and possess a Gaussian profile of the form

$$F(E) \propto e^{-\left(\frac{E-(E_0-S\hbar\omega)}{2\langle\sigma_t^2\rangle}\right)}, \tag{8}$$

which has a variance defined by Equation (6). In this case, the FWHM of the emission spectra is given by the expression analogous to that of a Gaussian function:

$$FWHM(T) = 2\sqrt{2\ln(2)\langle\sigma_t^2\rangle} \approx 2.36\sqrt{S}E_{ph}\sqrt{\coth\left(\frac{E_{ph}}{2k_BT}\right)}, \tag{9}$$

with $E_{ph} = \hbar\omega$. Together, Equations (3) and (9) describe the role and strength of the EPC in exciton processes within emission phenomena, which are related to intraband scattering through acoustic and optical phonons, as well as interband contributions through multiphonon emissions and lattice distortions. They provide a quantitative way to characterize the interaction between carriers and the lattice in LDMHPs, which has been widely used to compare and design new structures for light-emitting applications [89–92].

3 EXPERIMENTAL AND COMPUTATIONAL METHODS

This chapter provides an overview about the experimental setup and computational details employed throughout this thesis and is divided into three parts: the synthesis of different LDMHPs, the characterization of the synthesized compounds using a range of room- and temperature-dependent techniques, and the computational studies performed to complement the experimental analysis.

3.1 Synthesis method

The LDMHPs investigated in this study were synthesized via the slow evaporation method. All reactants were purchased from Sigma-Aldrich and Alfa Aesar and used without further purification.

0D A_2SnBr_6 (A = Cs, Rb) perovskites: For the synthesis of Cs_2SnBr_6, 0.47 mmol of CsBr and 0.47 mmol of $SnBr_2$ were dissolved using 5 mL hydrobromic acid (HBr, 47 wt% in H_2O) and 10 mL of distilled water. The solution was heated at 70 °C for 1 hour under rigorous stirring and then kept at room temperature in a beaker sealed with a paraffin film for 5 days. Light-yellow prismatic crystals formed on the bottom of the beaker were collected and cleaned with a cold bath of HBr. After the cold bath of HBr, the crystals were kept at 100 °C in a vacuum furnace to avoid any HBr residue. For the synthesis of Rb_2SnBr_6, 0.18 mmol of Rb_2SO_4 and 0.18 mmol of $SnBr_2$ were dissolved using 5 mL of HBr and 5 mL of and distilled water. The solution was heated at 80 °C for 1 hour under rigorous stirring and then cooled slowly to room temperature in a beaker sealed with paraffin film. The solution was left undisturbed for 3 days. Clear light-yellow microcrystals grown at the bottom of the beaker were collected and cleaned with ethyl ether and dried overnight at 60 °C in a vacuum furnace.

2D A_2PbBr_4 (A = R-MBA, S-MBA) perovskites: For the synthesis of $(S\text{-}MBA)_2PbBr_4$, 1 mmol of PbO was dissolved in 5 mL of HBr at 120 °C under vigorous stirring for 15 minutes. After dissolution, 2 mmol of (S)-(-)-α-methylbenzylamine (S-MBA, 98%) was added dropwise and the solution was then stirred for 1 hour before being slowly cooled to room temperature and kept undisturbed for 1 day. Colorless microcrystals grown on the bottom of the beaker were collected and washed several times with ethyl ether to remove any residual solvent and left to dry overnight. The same synthesis procedure was used to obtain the $(R\text{-}MBA)_2PbBr_4$

compound, in the form of colorless microcrystals, replacing S-MBA for (R)-(+)-α-methylbenzylamine (R-MBA, ≥99.0%).

1D $(Rac\text{-}MBA)_3PbBr_5 \cdot H_2O$ perovskite: Similar to the synthesis of the 2D perovskites mentioned before, 1 mmol of PbO was dissolved in 5 mL of HBr at 120 °C under vigorous stirring for 15 minutes. After dissolution, 2 mmol of (±)-α-methylbenzylamine (Rac-MBA, 99%) was added dropwise and the solution was stirred for 1 hour before being slowly cooled to room temperature and kept undisturbed for 1 day. Colorless microcrystals grown on the bottom of the beaker were collected and washed several times with ethyl ether to remove any residual solvent and left to dry overnight.

3.2 Experimental measurements

Single crystal X-ray diffraction (SCXRD): SCXRD measurements were performed on a Bruker D8 Venture X-ray diffractometer equipped with a Photon II Kappa detector and Mo $K\alpha_1$ radiation (λ = 0.71073 Å) microfocus source. Suitable crystals from each sample were chosen and mounted on a MiTeGen MicroMount using immersion oil. The APEX 6 software was used for unit cell determination and data collection. The data reduction and global cell refinement were made using the Bruker $SAINT^+$ software package, and a numerical absorption correction was performed with SADABS [93,94]. The structures were solved by intrinsic phasing method using SHELXT [95], allowing the location of most of the atoms. The remaining atoms were located from difference Fourier maps calculated from successive full-matrix least-squares refinement cycles on F^2 with SHELXL [96] and refined using anisotropic displacement parameters under the graphical interface Olex2 [97]. Hydrogen atoms were placed according to geometrical criteria and treated using the riding model. The VESTA software [98] was used to prepare the artwork representations of the crystal structures.

Powder X-ray diffraction (PXRD): Room-temperature PXRD data were collected using a diffractometer D8 focus, Bruker AXS, using Cu $K\alpha_1$ radiation source and wavelength λ = 1.5406 Å. Rietveld refinements were performed on EXPO2014 and GSAS-II software programs. For the $(S\text{-}MBA)_2PbBr_4$ data, refinements from the crystallographic information file (CIF) of $(S\text{-}MBA)_2PbI_4$ (CCDC 607741) and $(S\text{-}MBA)PbBr_3$ (CCDC 1877054) were used where the iodide halide was switched for the bromide one. The same procedure was adopted for the case of $(R\text{-}MBA)_2PbBr_4$, using the CIFs from $(R\text{-}MBA)_2PbI_4$ (CCDC 607740) and (R-

MBA)$PbBr_3$ (CCDC 1877050).

Temperature-dependent PXRD measurements were performed on a STADI-P (Stoe®, Darmstadt, Germany) diffractometer operating in Debye-Scherrer geometry. The instrument is equipped with a curved Ge(111) monochromator to select the Cu $K\alpha_1$ radiation (λ = 1.54056 Å). The powdered sample was loaded into a 0.3 mm diameter glass capillary. Measurements were performed at several discrete temperatures stabilized and controlled by an Oxford Cryostream 1000 series cryostat. Diffraction patterns were recorded in the $2.000° \leq 2\theta \leq 93.335°$ angular range, with step sizes of 0.015° and an acquisition time of 50 s for each 1.05° scan window. Structural analysis and Rietveld refinements were conducted using the TOPAS-Academic v.7 software [99].

Raman spectroscopy: Room- and low-temperature Raman-active spectra were collected using a T64000 Jobin–Yvon spectrometer equipped with an Olympus microscope and an LN_2-cooled CCD for scattered light detection in a single mode. The spectrometer slits were set to give a spectral resolution better than 2 cm^{-1}. All measurements were performed using a long working distance plan-achromatic objective of 20x. The spectra were generated by exciting the samples with Argon and Krypton ion lasers operating at different wavelengths of 458, 488, 514 and 647 nm. He-compressed closed-cycle cryostat with a Lakeshore 330 temperature controller with the precision of ±0.1 K were employed to achieve low-temperature conditions. Each low-temperature Raman spectra were deconvoluted for data analysis in the sum of Voight functions using Fityk software [100].

Infrared (IR) spectroscopy: A Bruker Vertex 70 V Fourier-transform spectrometer was used to acquire the IR reflectance spectrum. Data in the far-IR region were collected using a mercury (Hg) lamp as the light source, while signal detection was carried out using DLaTGS pyroelectric detectors. The dataset was obtained through 256 scans and a spectral resolution of 2 cm^{-1}. The treatment of data was performed using the IRFit and KKG softwares.

Absorption spectroscopy: For the samples Cs_2SnBr_6 and Rb_2SnBr_6, room-temperature absorption spectra were recorded through via diffuse reflectance spectroscopy (DRS) using a Shimadzu UV-2600 spectrophotometer equipped with an ISR-2600 Plus integrating sphere. The reflectance spectrum obtained was further processed by the Kubelka–Munk function to transform it into an absorption spectrum [101]. For the samples (R-/S-MBA)$_2PbBr_4$ and (Rac-MBA)$_3PbBr_5 \cdot H_2O$, absorption spectra were recorded in the transmission mode using a Thermo

Fisher Evolution 220 spectrophotometer.

Photoluminescence (PL) spectroscopy: For the samples Cs_2SnBr_6 and Rb_2SnBr_6, room- and low-temperature PL measurements were performed using the same setup for Raman spectra acquisition. A T64000 Jobin–Yvon spectrometer equipped with an Olympus microscope and an LN_2-cooled CCD to detect the emitted radiation of the sample in a single mode were used to collect the PL data. He-compressed closed-cycle cryostat with a Lakeshore 330 temperature controller with the precision of ±0.1 K were employed to achieve low-temperature conditions. Cs_2SnBr_6 samples were excited with an Argon ion laser operating at wavelengths of 458, 488, 514 nm for room-temperature data, and with excitation of 457 nm for the low-temperature regime. For the Rb_2SnBr_6 samples, room- and low-temperature PL spectra were recorded with an excitation from an external lamp operating at 405 nm and power-dependent PL spectra at 10 K was recorded using the Argon ion laser at a wavelength of 457 nm, digitally tuning the laser power and measuring its real value at laser focus with a Coherent LaserCheck Power Meter, keeping low intensities to avoid laser damage. Each PL spectra were deconvoluted for data analysis in the sum of Gaussian functions using Fityk software.

For the (R-/S-MBA)$_2$PbBr$_4$ and (Rac-MBA)$_3$PbBr$_5$·H$_2$O samples, room-temperature PL spectra were recorded using a Horiba FluoroMax Plus spectrofluorometer equipped with a 150 W continuous-wave Xenon arc lamp. The low-temperature PL spectra of the (Rac-MBA)$_3$PbBr$_5$·H$_2$O samples were obtained in a closed-cycle Janis CCS-150 cryostat. A continuous-wave linearly-polarized CNI laser with a photon energy of 3.88 eV (320 nm) was used to excite the sample. The photoluminescence signal was focused on an Andor Shamrock SR-500i spectrometer coupled with an Andor CCD (iDus DU420A-BU).

Circular dichroism (CD): CD spectra were collected using a JASCO J-815 spectropolarimeter. To perform the measurement, thin films were prepared by dissolving the samples in N,N-dimethylformamide (DMF, 99.8%) at a concentration of 25 mg of the samples per 100 μL of DMF. After, a 10 μL aliquot of the solutions were drop-cast onto quartz substrates, which were subsequently heated at 65°C for 1 hour.

Differential scanning calorimetry (DSC): DSC measurements were performed on a Q2000 calorimeter (TA Instruments). The experiment was conducted at a rate of 5 °C min^{-1} over the temperature range of 70–180 °C under a nitrogen atmosphere using 5 mg of the sample for each run.

Scanning electron microscopy (SEM): SEM analysis was performed in a JSM-6010LA microscope model operating at a 12 kV accelerating voltage. To ensure electrical conductivity and minimize charging effects, the samples were mounted onto conductive carbon tape. Images were acquired using a secondary electron detector at different magnifications.

3.2 Computational details

Concerning the Rb_2SnBr_6 perovskite, first-principles calculations were performed using the Cambridge Serial Total Energy Package (CASTEP) code [102], within the framework of Density Functional Theory (DFT) [103]. The Generalized Gradient Approximation (GGA) functional described by Perdew–Burke–Ernzerhof (PBE) was applied to simulate the exchange-correlation potential [104]. van der Waals (vdW) dispersive interactions were included via the Tkatchenko–Scheffler (TS) scheme [105] to reliably predict the structural parameters in the A_2BX_6 perovskites due to contribution of vdW forces between the $[BX_6]^{2-}$ octahedra [106]. Calculations were performed including the influence of spin-orbit coupling (SOC) due to the presence of the heavy Sn element. The primitive unit cell of the Rb_2SnBr_6 was used and convergence tests were applied using 330, 650 and 900 eV of plane-wave cutoff energies along with $(2 \times 2 \times 2)$ and $(10 \times 10 \times 10)$ Monkhorst-Pack k-point meshes [107]. The cutoff energy of 650 eV and k-point mesh of $(2 \times 2 \times 2)$ were confirmed to guarantee the convergence threshold criteria considered of 0.5×10^{-5} eV/atom for total energy change, 0.01 eV/Å for total force per atom, 0.02 GPa for crystal pressure and maximum atomic displacement smaller than 0.5×10^{-3} Å. For numerical optimization, the Broyden-Flether-Goldfarb-Shanno (BFGS) algorithm was applied [108]. For simulation of core electrons, the Norm-Conserving Pseudopotentials (NCPP) [109] were used with following valence configurations: $3d^{10}\ 4s^2\ 4p^5$ for Br atom, $4s^2\ 4p^6\ 5s^1$ for Rb atom and $4d^{10}\ 5s^2\ 5p^2$ for Sn atom. The electronic minimization parameters applied in the Self-Consistent Field (SCF) cycles were 0.5×10^{-6} eV for total energy per atom and 0.1406×10^{-6} eV for eigen-energy tolerance with three cycles for convergence tolerance window. After convergence was reached, the Kohn-Sham band structure and density of states (DOS) were calculated. Phonon properties were calculated using the Density Functional Perturbation Theory (DFPT) [110] within the linear response formalism with GGA(PBE)+TS level of theory upon the optimized unit cell with a q-point grid interpolation spacing of 0.05 $Å^{-1}$ and a convergence tolerance of 1×10^{-5} $eV/Å^2$ on the interatomic force constants. For the electronic band structure, since pure

functionals like GGA(PBE) tends to underestimate the energy bandgap [111], the Heyd–Scuseria–Enzerhof hybrid functional (HSE06) was employed to improve the description of electronic structure and the bandgap prediction [112–114]. Due to computational costs, SOC was not included in the phonon properties calculations or in the electronic band structure calculations using HSE06. The conductivity effective masses of electrons and holes were calculated from the harmonic average [115,116] of their respective effective masses from the valence band maximum (VBM) and conduction band minimum (CBM) along the $\Gamma \rightarrow X$, $\Gamma \rightarrow K$ and $\Gamma \rightarrow L$ directions of the high symmetry points of the electronic band structure calculated with HSE06.

For (R-/S-MBA)$_2$PbBr$_4$ and (Rac-MBA)$_3$PbBr$_5$·H$_2$O, the *ab initio* calculations were performed within the DFT using GGA(PBE) exchange–correlation functional [117] as implemented in the Vienna *ab initio* simulation package [118,119]. Spin–orbit interaction was included in some calculations to introduce the effect of the noncollinear spin and relativistic corrections with cutoff energies of 500 eV, k-point sampling of (6 × 6 × 3) for the experimental atomic configurations. The electronic structure has been minimized with a converge criteria of 10^{-5}eV, while the geometry and forces have been set to the experimental configuration without additional atomic relaxation.

4 ELECTRON-PHONON COUPLING IN ALL-INORGANIC 0D HALIDE PEROVSKITES

Zero-dimensional metal halide perovskites (0D MHPs) represent a class of materials characterized by a crystal structure where the metal-halide octahedra or tetrahedra are completely isolated from one another by large organic or inorganic cations [120]. Unlike their 3D counterparts, which feature a continuous network of corner-sharing octahedra, 0D MHPs lack of corner, edge, or face-sharing connectivity, and some examples are illustrated in Figure 8 [121]. This lack of connectivity allows bulk crystals to retain the intrinsic optoelectronic properties of individual metal-halide units, resulting in high photoluminescence quantum yields and broadly tunable bandgaps [53]. The 0D MHPs are usually more stable than the 3D because the isolated metal-halide clusters are surrounded by the A cation, which shield them from degradation caused by oxygen, moisture, and light [122,123]. Furthermore, their structural versatility and tolerance for diverse, eco-friendly metal ions such as Sn^{2+}, Cu^{+}, and Bi^{3+} [124,125], enable precise control over crystal structures and electronic band configurations, facilitating high-performance applications in photodetectors, LEDs, and related optoelectronic devices [126,127].

Figure 8 – Some examples of 0D MHPs, where Ln represents lanthanide ions and M denotes divalent metal cations

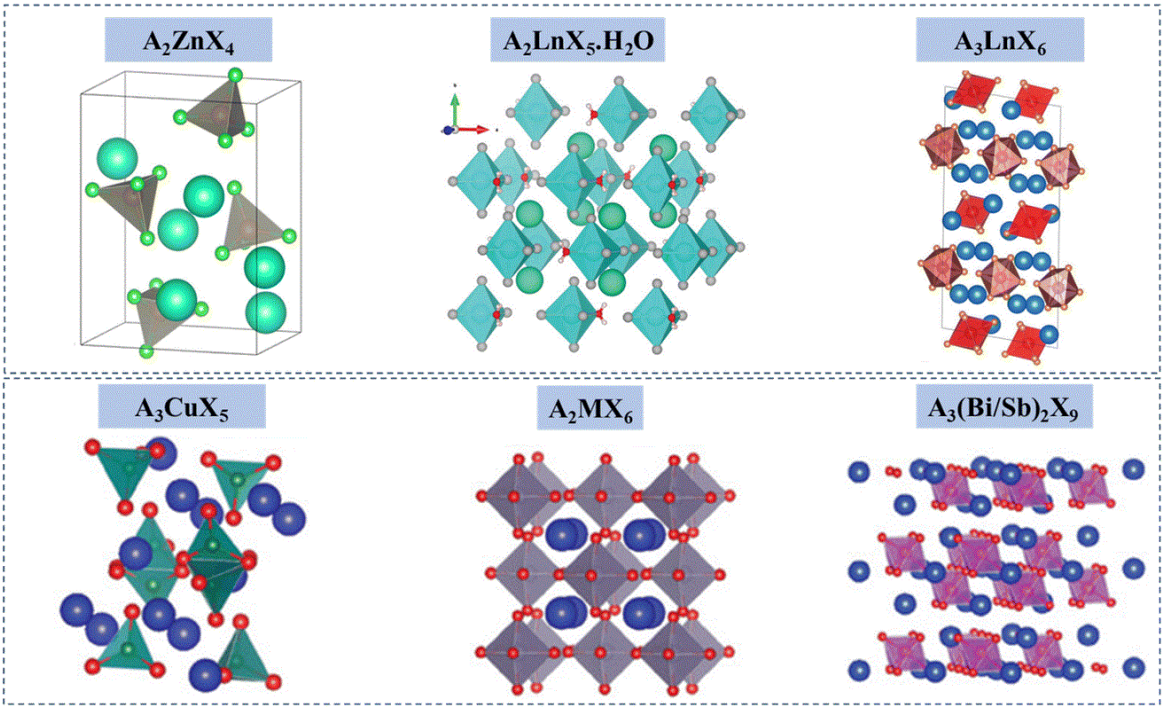

Source: adapted from reference [121].

In 0D MHPs, the electronic structure is mainly defined by the metal-halide units, where the VB and CB are composed hybridized states from the metal cation and halide anion orbitals [121]. However, the spatial isolation of these metal-halide clusters prevents the formation of continuous electronic bands and restricts carrier mobility to within the independent polyhedra. Therefore, this high degree of quantum confinement leads to localized electronic states confined within individual clusters, with negligible inter-cluster electronic delocalization which result in larger bandgaps, stronger exciton binding energy and smaller band dispersions compared to the 3D cases [120]. Upon photoexcitation, the confined photogenerated carriers interact strongly with the lattice through EPC, leading to formation of STE, as well as self-trapped electron and holes stabilized by the bond contraction of the clusters, resulting in broadband emission of with large Stokes shift energy [128].

These optoelectronic properties have been extensively investigated across various 0D MHPs. For instance, the organic–inorganic hybrid $(C_4H_{12}N)_2InCl_5 \cdot DMF$ has demonstrated near-unity photoluminescence quantum yield (PLQY) of 99.3% together with broadband yellow emission that could be tunned with Sb^{3+} doping [129]. Highly stable $Cs_3Cu_2X_5$ (X = Cl, Br, I) crystals have been demonstrated to possess high PLQYs of up to 90%, exhibiting broad luminescence from violet to green significant potential for photodetector applications where Jahn–Teller-like distortions upon photoexcitation acting as the principal mechanism governing carrier trapping [130]. $(TEBA)_2SbCl_5$ (TEBA = benzyltriethylammonium) samples have been shown to exhibit dual emission covering the entire visible spectrum due to STE, with long decay lifetimes and they have already been applied in white-light LED devices with high efficiency [131]. The series of 0D MHPs $A_2M_3I_9$ (A = Cs, Rb; M = Bi, Sb) has been shown to exhibit a variety of temperature-dependent PL behaviors governed by the EPC of each specific material, highlighting the versatile optoelectronic features of these low-dimensional perovskites [90].

To gain a deep understanding of the optoelectronic properties of the 0D MHPs, an investigation into EPC is essential. Accordingly, this chapter focuses on the study of EPC in two specific 0D MHPs: Cs_2SnBr_6 and Rb_2SnBr_6. The selection of all-inorganic constituents is motivated by their superior stability compared to hybrid organic-inorganic analogs, while the substitution of Pb with Sn addresses the demand for environmentally friendly materials [132,133]. These compounds are classified as vacancy-ordered double perovskites (VODPs), a derivative of the double perovskite structure $A_2B^IB^{III}X_6$, where B^I and B^{III} are monovalent and trivalent metal cations, respectively. In VODPs, half of the metal cations are removed to yield the form $A_2B\square X_6$, where $\square$ represents a structural vacancy and B is a

tetravalent cation [134]. By employing several techniques including temperature-dependent PL, vibrational spectroscopy, and theoretical analysis, this chapter investigates the strength of the EPC, the origin of PL behavior, and the phonons mediating carrier-lattice interactions. These findings provide insights into the fundamental nature of electron-phonon interactions within these 0D MHPs.

4.1 Strong electron–phonon coupling in vacancy-ordered Cs_2SnBr_6 double perovskite

Figure 9(a) illustrates the crystal structure of the VODP Cs_2SnBr_6 belonging to the $Fm\bar{3}m$ space group, which represents a defect variant of the 3D perovskite $CsSnX_3$ [135]. This structure is obtained by removing half of the Sn atoms at each center interval of the $[SnBr_6]^{2-}$ octahedron. The Cs atoms adopt regular 12-fold coordination, occupying the interstitial sites between $[SnBr_6]^{2-}$ [136]. The crystallographic data and structure refinement results from the SCXRD performed on the Cs_2SnBr_6 samples are presented in Table 1. It is interesting to point out that the measured Sn–Br bond length of 2.602 Å maintains constant along all octahedra, which is usual in conventional cubic double perovskite systems, which indicates the absence of bond length distortions in the $[SnBr_6]^{2-}$ octahedron [137,138].

Figure 9 – (a) Room-temperature crystal structure of the VODP Cs_2SnBr_6. (b) Raman spectrum recorded at room temperature using a wavelength excitation of λ_{exc} = 647 nm. The inset displays the Raman-active vibrational modes and their respective irreducible representations, as well as a representative image of the Cs_2SnBr_6 crystals used in the measurements. (c) Low-temperature Raman spectra obtained using λ_{exc} = 647 nm

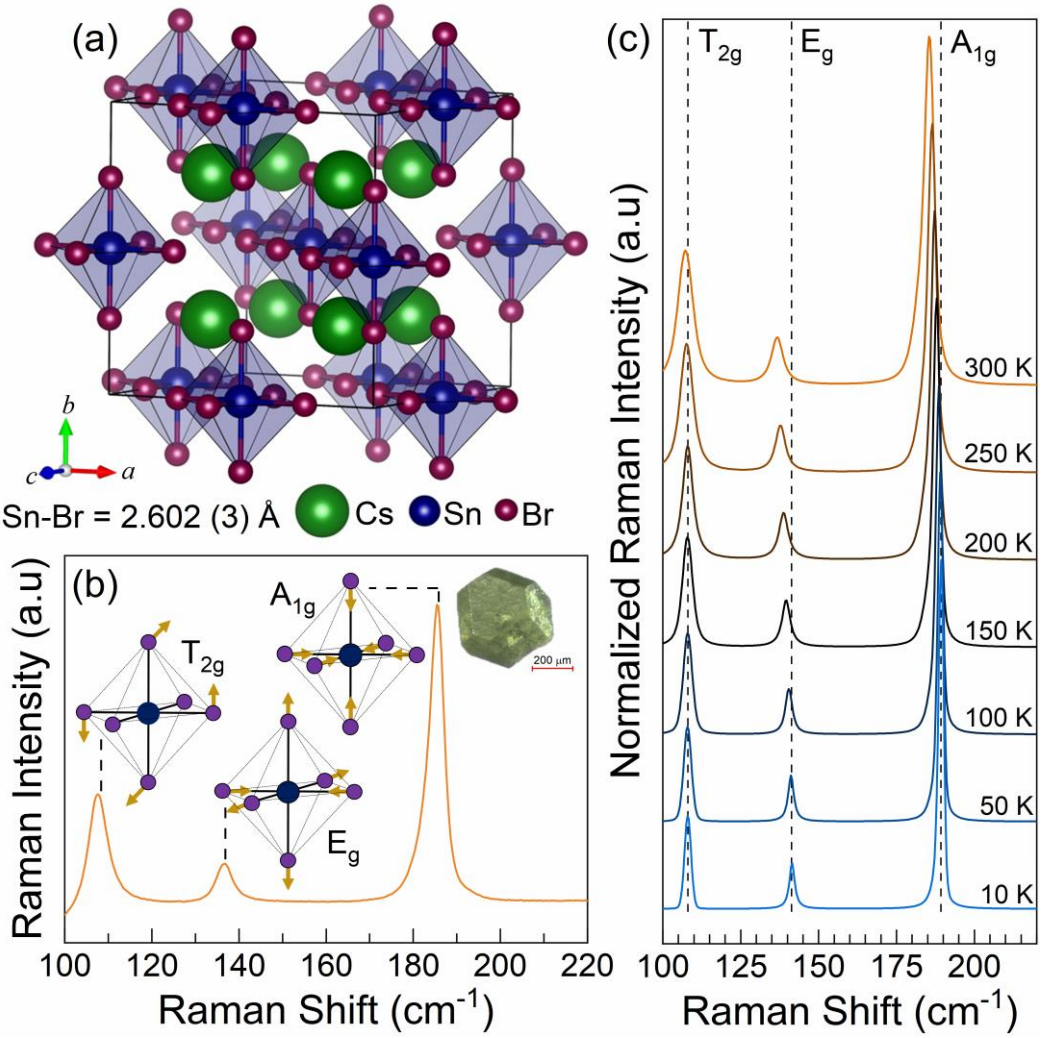

Source: elaborated by the author.

Table 1 – Crystal data and refinement parameters of Cs_2SnBr_6 from SCXRD measurements

Empirical formula	Cs_2SnBr_6
Formula weight	863.97
Temperature (K)	298
Crystal system	Cubic
Space group	$Fm\bar{3}m$
a (Å)	10.8416 (2)
Volume (Å^3)	1274.32 (7)
Z	4

ρ_{calc} (gcm^{-3})	4.503
μ (mm^{-1})	26.389
F(000)	1480
Crystal size (mm^3)	0.262×0.258×0.214
Crystal colour	Clear light yellow
Crystal shape	Block
Radiation	MoK_α (λ=0.71073 Å)
2θ range (°)	6.51 to 60.47
Index ranges	-15 ≤ h ≤ 15 -15 ≤ k ≤ 15 -15 ≤ l ≤ 15
Reflections collected	4542
Independent reflections	131
Completeness	100.0 %
Goodness-of-fit on F^2	1.469
Final R indexes	R_1 = 0.0314
(I≥2σ(I))	wR_2 = 0.0866
Final R indexes	R_1 = 0.0314
(all data)	wR_2 = 0.0866
Largest peak/hole (eÅ^{-3})	1.38/-2.03
Extinction coefficient	0.00050(10)

Source: elaborated by the author.

For the vibrational symmetry analysis of the Cs_2SnBr_6 crystal structure, the room-temperature group theory based on the site occupation predicts ten normal modes of vibrations Γ_M distributed among the irreducible representations of the O_h point group as $\Gamma_M = A_{1g} \oplus E_g \oplus T_{2u} \oplus 2T_{2g} \oplus 4T_{1u} \oplus T_{1g}$, of which T_{2u} and T_{1g} are silent, one T_{1u} is acoustic, three T_{1u} are IR active, and the remaining A_{1g}, E_g and $2T_{2g}$ are Raman-active [139,140]. Figure 9(b) presents the Raman spectrum at room temperature under an excitation source of λ_{exc} = 647 nm (1.92 eV), revealing three normal modes associated with vibrations of the $[SnBr_6]^{2-}$ octahedron: the symmetric stretching $\nu_s(A_{1g})$ = 187 cm^{-1} of the Sn–Br bonds; the asymmetric stretching $\nu_{as}(E_g)$ = 138 cm^{-1} related to equatorial and axial Sn–Br bonds; and the asymmetric bending $\delta_{as}(T_{2g})$ = 108 cm^{-1} concerning the Br–Sn–Br configurations [141]. The last lattice vibration $\nu_L(T_{2g})$ Raman mode is expected at lower Raman shift values below 100 cm^{-1} [142]. At low temperatures down to 10 K, Raman scattering did not reveal any evidence of structural phase transition in Cs_2SnBr_6, as shown in Figure 9(c), indicating high stability and preservation of the $Fm\bar{3}m$ symmetry. Upon heating, a usual thermal lattice anharmonicity was observed [139], accompanied by a substantial broadening of Raman peaks associated with the $[SnBr_6]^{2-}$. This is

expected, since the vacancy-ordered configuration stabilizes the isolated octahedral orientation, preventing induced phase transitions by tilting corner-sharing octahedra, as is usual in Pb-based halide perovskites undergoing lattice contraction [143,144].

Interestingly, the Raman spectrum with λ_{exc} = 458 nm presented additional unexpected overtones at higher wavenumbers as shown in Figure 10(a). It was apparent that the most intense Raman mode A_{1g} overtone could be observed up to the fourth-order (4th), together with another combination of modes. Analyzing the A_{1g} mode, the center of its high-order modes could be fitted using $\omega_n = n\omega$, in which ω is the first-order A_{1g} frequency, and n is the mode overtone. As illustrated in Figure 10(b), the fit of the four overtone centers provided a phonon frequency of ω = 174 ± 2 cm^{-1}, which follows the first-order A_{1g} mode, indicating that the multiphonon peaks arose from a common phonon mode [145]. Furthermore, the intensities of the overtones were much smaller compared to that of the first-order phonon and decreased rapidly with the order number as shown in Figure 10(b). The intensities followed the relation $I \propto K^n$, where I stands for intensity and K is the probability of scattering one phonon [137,146]. Fitting the relation for the A_{1g} overtones, the value of K = 0.22 ± 0.02 was obtained, which is quite large considering the appearance of multiphonon at room temperature. Unfortunately, PL phenomena prevented the analysis of high-order scattering at lower temperatures since the photoluminescence baseline hid the Raman signal, as already evident in the room-temperature case shown in Figure 10(a).

Figure 10 – (a) Unpolarized Raman spectrum of Cs_2SnBr_6 perovskite recorded using an excitation of λ_{exc} = 458 nm, highlighting the observation of up to the fourth A_{1g} harmonic and multiphoton assignments with the presence of PL emission. (b) Wavenumber and intensity of the A_{1g} overtone modes. (c) Comparison of the Raman scattering effect, conducted with different excitation energies. (d) Normalized Raman spectra with different wavelengths of excitation sources by the maximum A_{1g} mode. Note that with a 647 nm excitation line, there is no presence of PL emission, but signs of emission spectrum are present with 514 nm, 488 nm, and 458 nm excitation lines

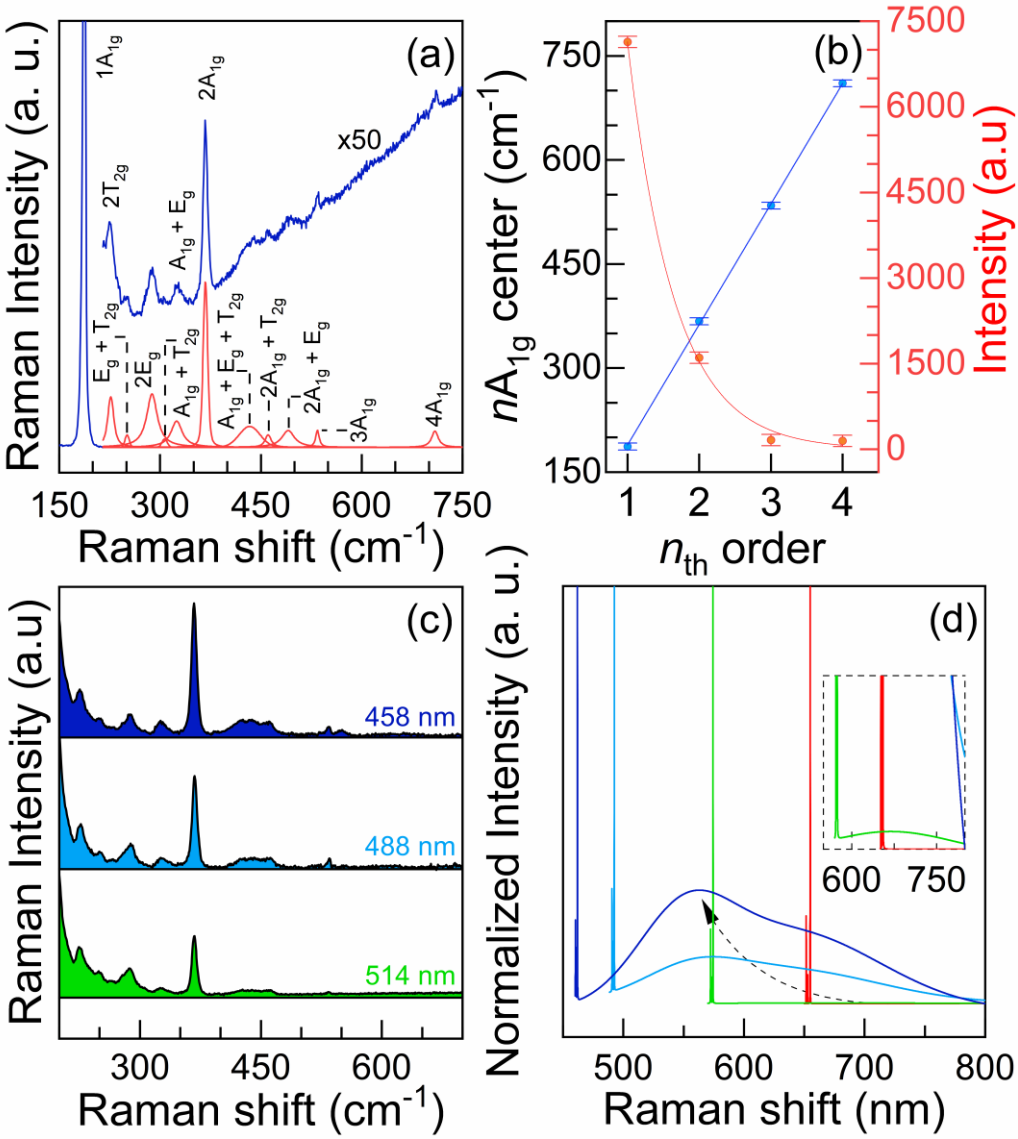

Source: elaborated by the author.

The observation of overtones up to the 4th order indicated a strong EPC present in Cs_2SnBr_6, compared to that reported for other similar double perovskites such as $Cs_2AgBiBr_6$ [147], $Cs_2NaFeCl_6$ [137], $Cs_2Ag_{0.4}Na_{0.6}InCl_6$ [146], and the 3D perovskite

$CsPbBr_3$ [148]. These overtones are discussed in terms of the formation of polarons and STE, which lead to and facilitate anharmonicity effects. In this scenario, the strong EPC at room-temperature could locally deform the crystal structure near a photoexcited carrier, leading to its self-trapping. Consequently, the excited electronic state possesses different atomic coordinates than the ground state. Furthermore, multiphonon Raman scattering, promoted by the Franck–Condon mechanism, is activated if the excitation photon energy becomes closer to an optical transition between the ground and excited state [149,150]. These observations align with the analyzed increase of multiphonon intensities with excitation energy at room-temperature Raman spectra excited with different excitation sources of λ_{exc} = 514 nm (2.41 eV), 488 nm (2.54 eV), and 458 nm (2.71 eV) in Figure 10(c) (where the spectra were normalized relative to the first-order A_{1g} mode and the background was removed to facilitate comparisons). Additionally, broad photoluminescence was observed in Figure 10(d) under the same excitation lines used in this paper (except for the 647 nm line, where no signs of luminescence and overtones were detected). These results suggest that electronic STE states drove high-order Raman scattering multiphonon emissions modulated by EPC strength.

The excited states involved in multiphonon scattering were investigated via optical absorption analysis using diffuse reflectance measurements in the ultraviolet-visible (UV-vis) range. Figure 11(a) shows the reflectance spectrum converted into absorbance using the Kubelka–Munk function $F(R)$. Different authors discuss discrepancies regarding the origin of the bandgap of Cs_2SnBr_6. Nanocrystals samples of this perovskite have exhibited one-band STE emission at 2.08 eV [151], while single crystals display a direct optical band gap ranging from 2.70–3.27 eV [141,151–158]. Using the Tauc-plot method applied on the absorbance data [159], a direct-bandgap energy of 3.16 eV was obtained. It was noted that the absorption edge was followed by two distinct absorption peaks at 3.73 eV and 4.29 eV. Since the correct use of Tauc-plot method relies on the determination of the bandgap energies between the maximum of valence band and the minimum of the conduction band, where no intermediate energies such as excitons or defect states are considered, such a method only gives a sense about the beginning of optical absorption rather than the true energy bandgap [160]. It is also important to point out that our measurements closely align with DFT calculations by Kavanagh *et al.* [106], indicating significant contributions from excitonic bands, localized bound excitons, and pronounced EPC, resulting in the formation of emissive STE states at room temperature [161,162].

Figure 11 – Room-temperature excitations and emissions of Cs_2SnBr_6. (a) Optical absorption derived from diffuse reflectance measurements. (b) PL spectrum obtained using a 458 nm line excitation. (c) Configuration of the coordinate diagram and a schematic of multiphonon and exciton emissions. GS: ground state, Abs: absorption; PL: photoluminescence; FE: free exciton; and STE: self-trapped exciton

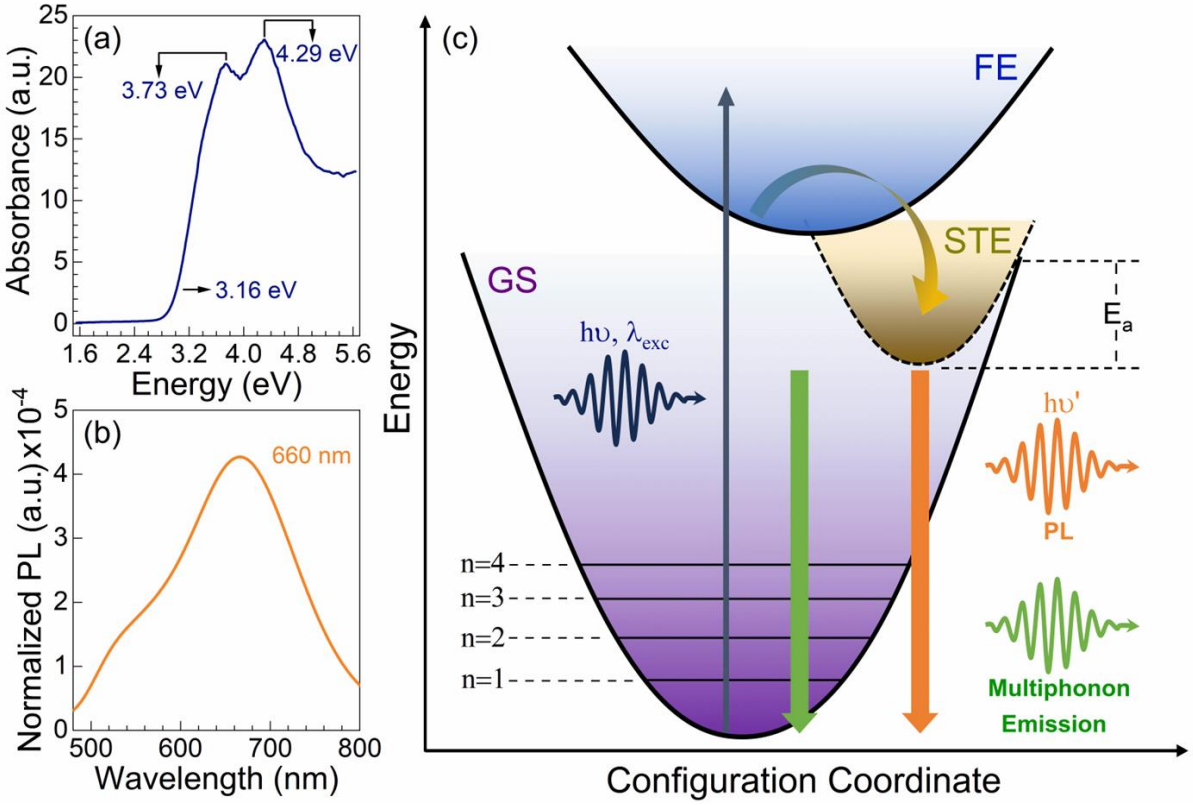

Source: elaborated by the author.

The room-temperature PL spectrum of Cs_2SnBr_6, excited at λ_{exc} = 458 nm, revealed an asymmetric broad and intense PL band from 1.58 to 2.60 eV. The PL emission center (at highest intensity) was at 660 nm (1.88 eV), as shown in Figure 11(b). Recent results showed that in halide VODPs with localized bound excitons the presence of a strong EPC gives rise to a broad PL emission as well as a large Stokes emission (higher than 0.5 eV), which are due to STE state formation [106,163]. Radiative recombination of STE typically exhibits broadband emissions with large Stokes shift energy, which can be followed by multiphonon emissions as depicted in Figure 11(c), which is consistent with our findings [164]. To further explore the strength of EPC and the STE process in Cs_2SnBr_6, the PL temperature dependence down to 10 K was evaluated, as shown in Figure 12(a). Two Gaussian curves were employed for the data fitting to account for the asymmetry in the PL. The maximum peak intensity of the spectra slightly shifts towards higher energy as the temperature decreases from 1.84 eV at room

temperature to 1.88 eV at 10 K. Concurrently, the bands exhibited increased symmetric shape and narrowness, particularly notable from 200 K to 10 K, where the spectra could be fitted with only one of the Gaussian curves. However, a large FWHM and Stokes shift energy (considering the excitation and emission energy) of 200 meV and 830 meV, respectively, were still observed at the lowest temperature.

Figure 12 – Temperature-dependent PL spectra of Cs_2SnBr_6. (a) Normalized PL emission as a function of temperature using a 458 nm laser excitation. (b) Highest-intensity PL position behavior with temperature. (c) Integrated PL intensity as a function of 1/T in logarithmic scale. (d) FWHM temperature-dependence

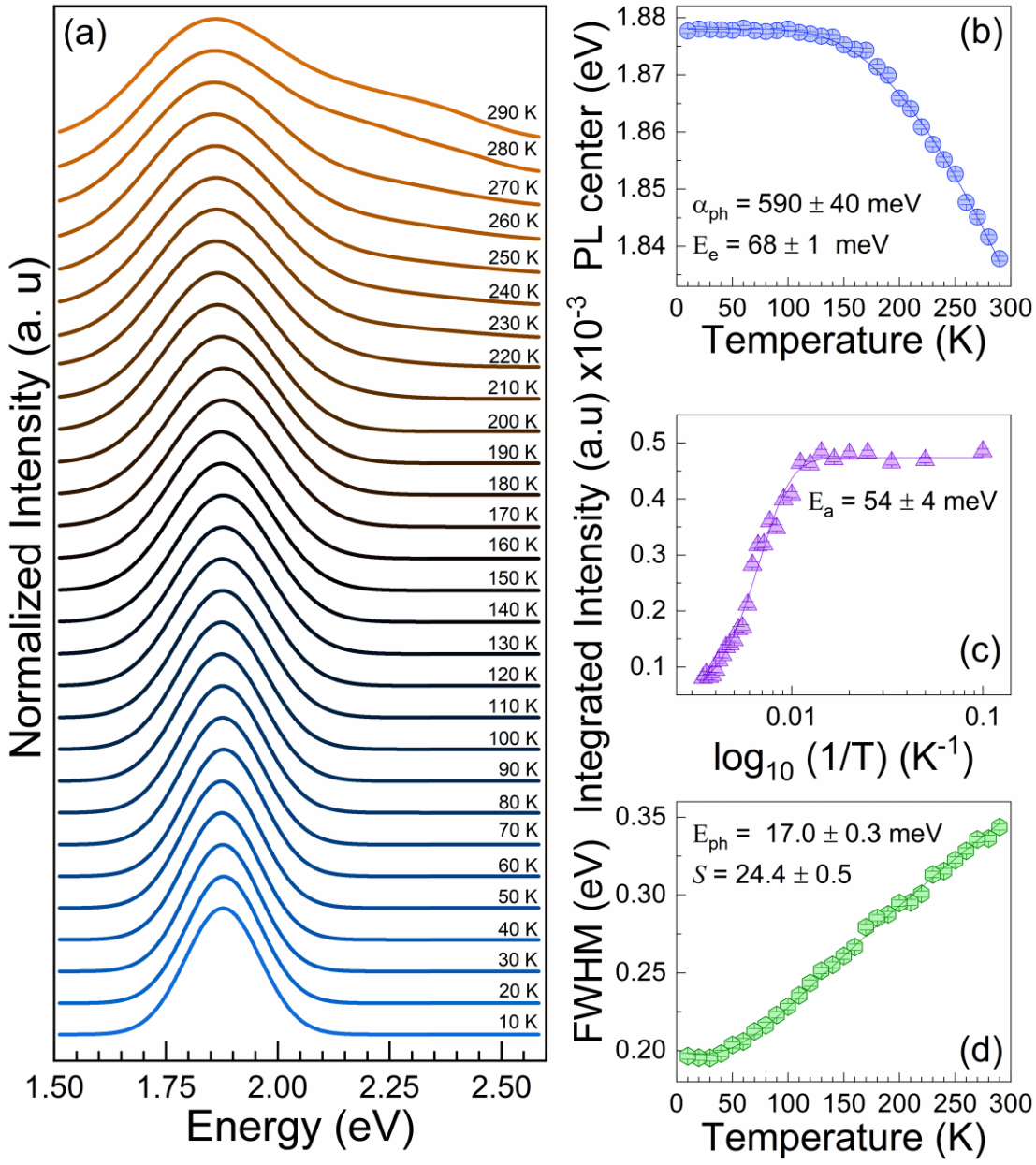

Source: elaborated by the author.

As previously discussed, the emission of electronic carriers in the compound were attributed to STE, influenced by the strong EPC. This interaction induces the shift of the emitted photon energy while increasing thermal broadening at higher temperatures, as indicated by the second Gaussian curve. This reduction may also be linked to the involvement of excited vibronic states in luminescence [165]. Interestingly, no distinct bands of FE were observed in the spectra of low-temperature dependence. The Bose–Einstein equation has been successfully applied to explore the impacts of EPC on PL energy E dependence on lead halide perovskites [166–168]. This model considers the electron interactions within the crystal lattice and is described by the following equation:

$$E = E_0 - \frac{\alpha_{ph}}{e^{\frac{E_e}{k_B T}} - 1}. \tag{10}$$

In Equation (10), the parameter α_{ph} is related to the strength of EPC, E_e represents the average energy of phonons interacting with the crystal, and E_0 denotes the zero-temperature energy. Figure 12(b) shows the fitted temperature-dependence energy, which gives the following values: E_0 = 1.878 ± 0.001 eV, α_{ph} = 590 ± 40 meV and E_e = 68 ± 1 meV. The notably high-energy E_e (551 cm^{-1}) could be attributed to phonon–phonon interactions as well as a multiphonon process occurring at high temperatures, and the considerable value of α_{ph} reveals strong EPC dependence on luminescence compared to other conventional semiconductors [169–171].

Thermal activation can induce the detrapping of STE, thereby reducing the radiative recombination rate. The STE activation energy E_a for the nonradiative decay mechanism can be evaluated through the relationship between the temperature and the integrated PL intensity $I_{PL}(T)$ using the Arrhenius equation:

$$I_{PL}(T) = \frac{I_0}{1 + Ae^{\frac{-E_a}{k_B T}}}, \tag{11}$$

where I_0 represents the integrated PL intensity at 0 K, and A is a factor related to the density of radiative recombination centers [172]. Figure 12(c) shows $I_{PL}(T)$ fitted using Equation (11) resulting in E_a = 54 ± 4 meV, confirming the possibility of formation of STE at room temperature ($k_B T \approx$ 25 meV). Observe that this is the STE activation energy, and not the STE

formation energy. The continuous decrease of $I_{PL}(T)$ for higher temperatures (lower $1/T$) suggests the reduction of radiative recombination by STE dissociation induced by thermal energy leading the electrons to return to ground states by nonradiative recombination pathways.

Regarding the dependence of the FWHM on temperature, a configuration coordinate model was employed to relate the emission broadening resulting from EPC and its strength through the Huang–Rhys factor S, as discussed in Chapter 2. Figure 12(d) shows the FWHM temperature dependence fitted according to Equation (9), obtaining S = 24.4 ± 0.5 and E_{ph} = 17.0 ± 0.3 meV. These values align with the approximate relation between S and the Stokes shift energy ΔE_{shift} given by $\Delta E_{shift} = 2SE_{ph}$ [87], where ΔE_{shit} = 829.6 meV, consistent with the previously mentioned 830 meV value for the Stokes shift energy observed in the Raman spectra, thereby illustrating the reliability of our results. The EPC in Cs_2SnBr_6 is stronger compared to other halide bromide perovskites such as $Cs_2AgBiBr_6$ (S = 15.4) [147,173] and $CsPbBr_3$ (S = 11.9) [174]. The obtained phonon energy of 17 meV (137 cm^{-1}) correlates well with Raman-active $\nu_{as}(E_g)$ related to the Sn–Br asymmetric stretching, which contributes to the anharmonicity of the $[SnBr_6]^{2-}$ octahedra and aligns with the similar non-VODP Cs_4SnBr_6 [175]. In VODPs, polarons are formed predominantly in the metal halide octahedra [BX_6] via modes concerning X–B–X bending and B–X stretching [176], and STE with Jahn–Teller octahedral distortions are known to be one of the reasons responsible for emission broadening [89]. This aligns with the Sn–Br asymmetric stretching since the atomic motion in the octahedra due to this mode is similar to the distortion caused by a Jahn–Teller interaction. Therefore, based on the above analyses, the strong EPC is responsible for the enhanced multiphonon and STE emissions, in which the contribution of the $\nu_{as}(E_g)$ mode predominates in the electronic carrier transition due to the natural contraction of two axial Sn–Br bonds and the elongation of four equatorial Sn–Br bonds along this mode.

4.2 Electron-phonon coupling mediated by Fröhlich interaction in 0D perovskite Rb_2SnBr_6

Figure 13(a) illustrates the crystalline structure of the 0D perovskite Rb_2SnBr_6 at room conditions, which belongs to the $Fm\bar{3}m$ space group. This structure is derived from the 3D $RbSnBr_3$ perovskite [177] by withdrawing half of Sn atoms that occupy the $[SnBr_6]^{2-}$ octahedra centers, with Rb^+ ions embracing 12-fold coordination at sites among the $[SnBr_6]^{2-}$ units. Similar to the previous case of Cs_2SnBr_6, the measured Sn-Br bond length of 2.5938 Å is

constant along all octahedra, indicating a lack of bond distortions in the $[SnBr_6]^{2-}$ octahedron. Table 2 summarizes the crystal data and parameters from SCXRD data refinement performed on synthesized Rb_2SnBr_6 microcrystals.

Figure 13 – (a) Crystalline structure of Rb_2SnBr_6 at room conditions. The inset shows one of the microcrystals synthesized in this work. (b) Phonon dispersion across the whole Brillouin zone and (c) phonon DOS of Rb_2SnBr_6 calculated at the GGA(PBE)+TS level of theory. The observed and calculated optical modes are displayed in the normalized spectrum of (d) IR reflectance and (e) Raman spectroscopy

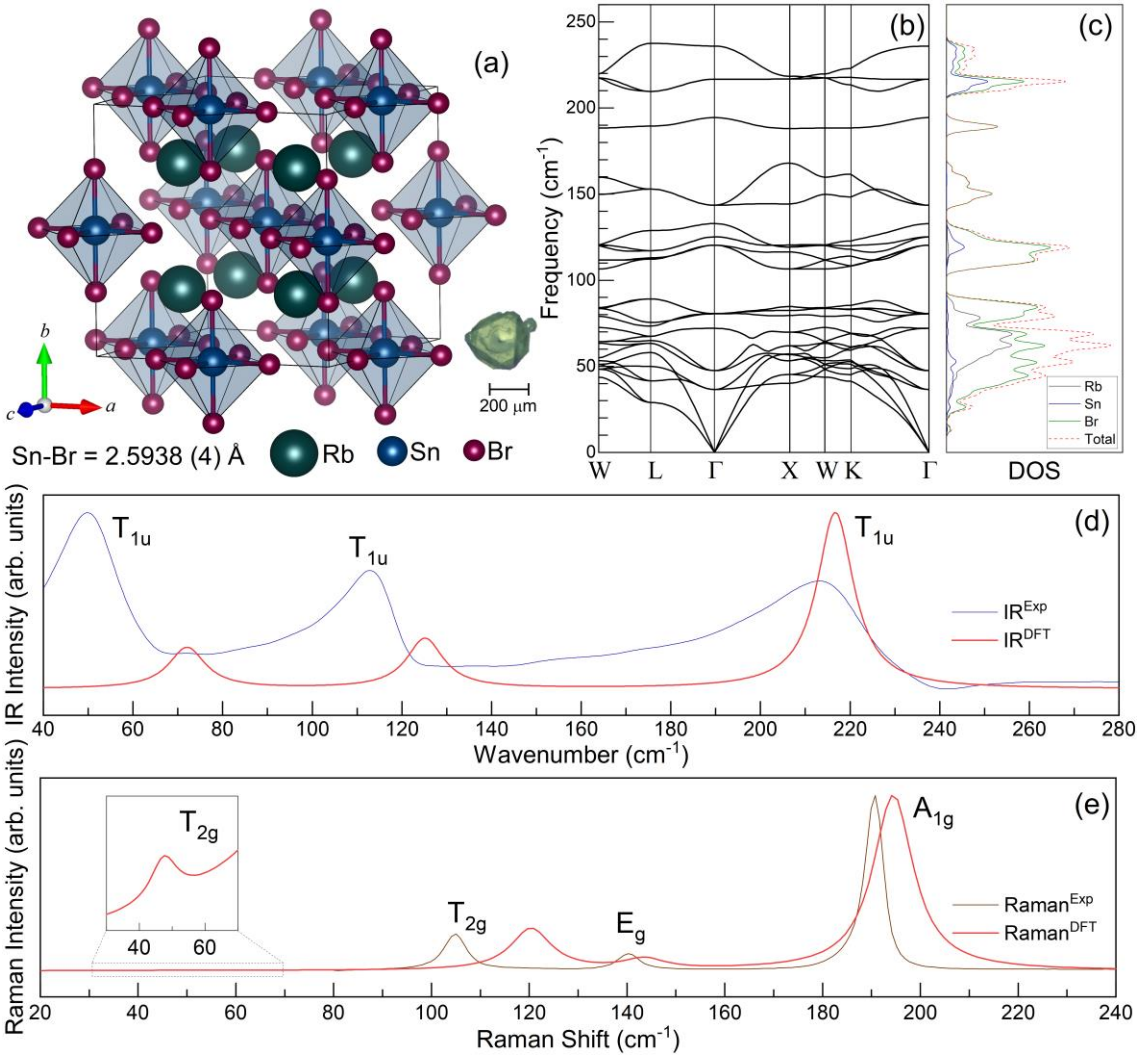

Source: elaborated by the author.

Tabel 2 – Crystal data and refinement parameters of Rb_2SnBr_6 from SCXRD measurements

Empirical formula	Rb_2SnBr_6
Formula weight	769.09
Temperature (K)	298

Crystal system	Cubic
Space group	$Fm\bar{3}m$
a (Å)	10.66180(10)
Volume (Å^3)	1211.97(3)
Z	4
ρ_{calc} (gcm^{-3})	4.215
μ (mm^{-1})	29.806
F(000)	1336
Crystal size (mm^3)	0.111×0.078×0.042
Crystal colour	Clear light yellow
Crystal shape	Block
Radiation	MoK_α (λ=0.71073 Å)
2θ range (°)	6.62 to 56.25
Index ranges	-14 ≤ h ≤ 14 -14 ≤ k ≤ 14 -14 ≤ l ≤ 14
Reflections collected	6006
Independent reflections	106
Completeness	100.0 %
Goodness-of-fit on F^2	1.225
Final R indexes	R_1 = 0.0107
(I≥2σ(I))	wR_2 = 0.0242
Final R indexes	R_1 = 0.0107
(all data)	wR_2 = 0.0242
Largest peak/hole (eÅ^{-3})	0.22/-0.41
Extinction coefficient	0.00177(8)

Source: elaborated by the author.

The group theory based on the site occupation of $Fm\bar{3}m$ space group from Rb_2SnBr_6 predicts ten normal modes, which can be decomposed among the irreducible representation of the $m\bar{3}m$ factor group as: $\Gamma_M = A_{1g} \oplus E_g \oplus T_{2u} \oplus 2T_{2g} \oplus 4T_{1u} \oplus T_{1g}$. As mentioned before for the case of Cs_2SnBr_6, among these modes, those with symmetries T_{1u} and T_{2u} are silent, one with symmetry T_{1u} is acoustic, three with symmetry T_{1u} are IR active, while the modes with symmetries A_{1g}, E_g and $2T_{2g}$ are Raman active. Figure 13(b) shows the calculated phonon dispersion by DFT along high-symmetry points (Γ, L, K, W, X) in the Brillouin zone. The vibrational frequencies are located in the range between 0 and 250 cm^{-1}, with distinct separation of vibrational branches. The acoustic modes exhibit typical linear behavior near the Γ-point, with the longitudinal acoustic (LA) and transverse acoustic (TA) modes displaying moderate dispersion, reflecting the rigidity and isotropy of the crystal

lattice [178,179]. The optical branches show significant splitting due to the pronounced mass contrast between Rb and Sn/Br and the macroscopic electric field inherent to the polar nature of Rb_2SnBr_6, a behavior observed in $CsBI_3$ (B = Pb, Sn) [180]. The absence of imaginary modes in the phonon dispersion indicates that the $Fm\bar{3}m$ crystal structure of Rb_2SnBr_6 is dynamically stable [138]. Figure 13(c) highlights the phonon DOS contributions of Rb, Sn, and Br atoms to the vibrational modes. Low-frequency modes below 50 cm^{-1} are primarily associated with the lattice vibrations dominated by the rattling motion of Rb atoms. Frequency modes in the 50–150 cm^{-1} range are attributed to bending vibrations of the $[SnBr_6]^{2-}$ octahedra, with contributions from both Sn and Br atoms. LO and TO splitting are observed around this region, while frequency modes above 150 cm^{-1} are dominated by stretching vibrations of the Sn–Br bonds, which reveals relatively low dispersion.

The normalized far-IR reflectance spectrum of Rb_2SnBr_6 at room temperature shown in Figure 13(d) presents the three IR modes predicted from theory [181]: the highest wavenumber mode $\nu_{as}(T_{1u})$ corresponds to asymmetric stretching of Sn-Br bonds, the intermediate wavenumber vibration $\delta_{as}(T_{1u})$ represents the Br-Sn-Br asymmetric bending, and the lowest wavenumber mode $\nu^{L}(T_{1u})$ is related to a lattice mode with out-of-phase displacements of $[SnBr_6]^{2-}$ octahedra and Rb^{+} cations. To obtain the frequencies of TO and LO modes, the Kramers-Kronig relations [182] were performed on the reflectance spectra to obtain the real $Re(\varepsilon)$ and imaginary $Img(\varepsilon)$ parts of the dielectric function $\varepsilon(\omega)$. The TO modes correspond to peaks in $Img(\varepsilon)$, whereas maxima in the imaginary part of the inverse of the dielectric function $-Img(1/\varepsilon)$ (also called as energy loss function) represent the LO modes. Both $Img(\varepsilon)$ and $-Img(1/\varepsilon)$ are shown in Figure 14. The obtained wavenumber values of the LO and TO modes, as well as the expected IR modes calculated through DFT at Γ point, are listed in Table 3.

Figure 14 – Imaginary part of the dielectric function [$Img(\varepsilon)$, (TO modes)] and energy loss function [$-Img(1/\varepsilon)$, (LO modes)]

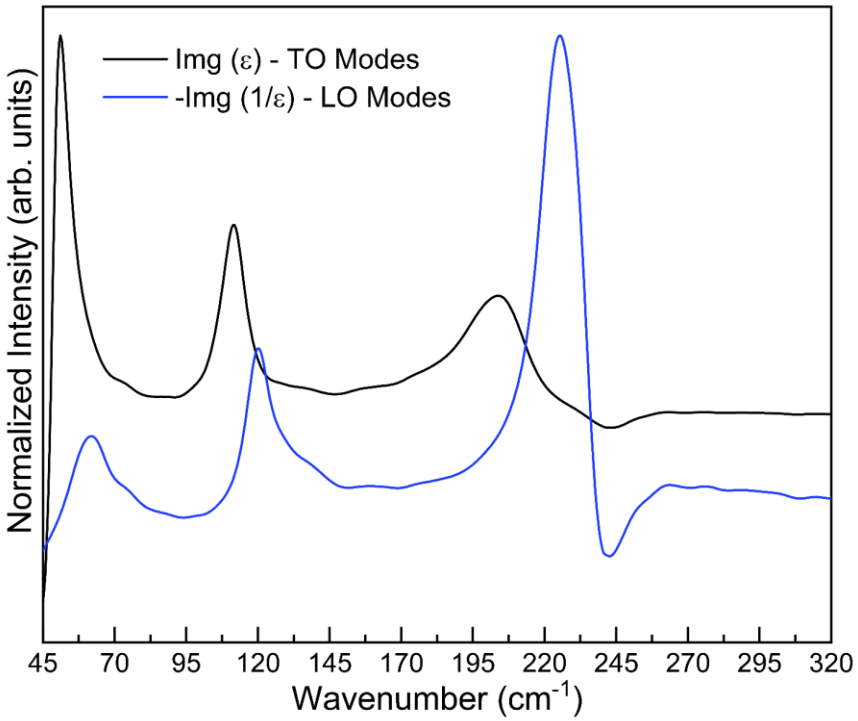

Source: elaborated by the author.

Table 3 – Observed and calculated IR and Raman modes of Rb_2SnBr_6 and their respective assignments. The symbols in the vibrational assignment stands for stretching (ν), bending (δ), asymmetric (as), symmetric (s), and lattice (L)

Experimental Data (cm^{-1})	Theorical DFT (cm^{-1})	Activity Mode	Mode Symmetry	Vibrational Assignment
-	47	Raman	T_{2g}	ν^L
51 (TO) 62 (LO)	72	IR	T_{1u}	ν^L
105	120	Raman	T_{2g}	δ_{as}
112 (TO) 120 (LO)	125	IR	T_{1u}	δ_{as}
140	144	Raman	E_g	ν_{as}
191	194	Raman	A_{1g}	ν_s
205 (TO) 225 (LO)	217	IR	T_{1u}	ν_{as}

Source: elaborated by the author.

To obtain the high-frequency dielectric constant ε_∞, the $Re(\varepsilon)$ was extrapolated at high frequencies and estimated ε_∞ = 3.71. The static dielectric constant ε_s was calculated through the generalized Lyddane-Sachs-Teller relation [141]:

$$\frac{\varepsilon_s}{\varepsilon_\infty} = \prod_i \left(\frac{\omega_{LO,i}}{\omega_{TO,i}}\right)^2, \tag{12}$$

where ω_{TO} and ω_{LO} are the TO and LO frequencies, respectively. Using the experimental values of the TO and LO modes in Equation (12), ε_s was evaluated as 7.57. These parameters are in accordance with previously reported theoretical values for isomorphous compounds Cs_2BX_4 (B = Sn, Ti; X = Cl, Br, I) [106].

Figure 13(e) presents the room-temperature Raman spectrum of Rb_2SnBr_6 under 457 nm excitation wavelength, which consists mainly of three peaks related to modes of $[SnBr_6]^{2-}$ vibrations, similar to the previous case seen for the Raman spectrum of Cs_2SnBr_6. These modes can be described, from lower to higher Raman shift, as follow [181]: $\delta_{as}(T_{2g})$ = 105 cm^{-1} asymmetric bending of Br-Sn-Br bonds, $\nu_{as}(E_g)$ = 140 cm^{-1} asymmetric Sn-Br stretching and $\nu_s(A_{1g})$ = 191 cm^{-1} symmetric stretching of Sn-Br. A fourth weak intensity peak at a higher Raman shift was assigned as the second-order mode of $\nu_s(A_{1g})$. The other $\nu^L(T_{2g})$ Raman active mode, corresponding to vibrations of Rb^+ cations within fixed $[SnBr_6]^{2-}$ lattice framework, is supposed to be at Raman shift values lower than 80 cm^{-1} (out of measured range). This mode aligns with the low-intensity calculated Raman DFT phonon around 47 cm^{-1}. These observations confirm strong agreement between experimental and DFT-calculated Raman modes at Γ point, which are all summarized in Table 3. Low-temperature Raman spectroscopy was performed to investigate possible structural phase transitions (SPT) or other anomalies in Rb_2SnBr_6. However, no substantial changes consistent with SPT or other anomalies were observed aside from expected thermal lattice anharmonicity accompanied by a narrowing of Raman peaks upon cooling, as shown in Figure 15. The changes in Raman shift modes with temperature were notably small, with the highest difference less than 5 cm^{-1} for the $\nu_s(A_{1g})$, showing that the cubic structure and bonding strength persist at lower temperatures, which can be related to the configuration of isolated octahedra that prevents phase transitions induced by tilting corner-sharing octahedra, commonly occurring in MHPs during lattice contraction upon decreasing temperature [143,183].

Figure 15 – (a) Temperature-dependent Raman spectra of Rb_2SnBr_6. Temperature dependence of the center and FWHM for (b) T_{2g}, (c) E_g, and (d) A_{1g} phonon modes

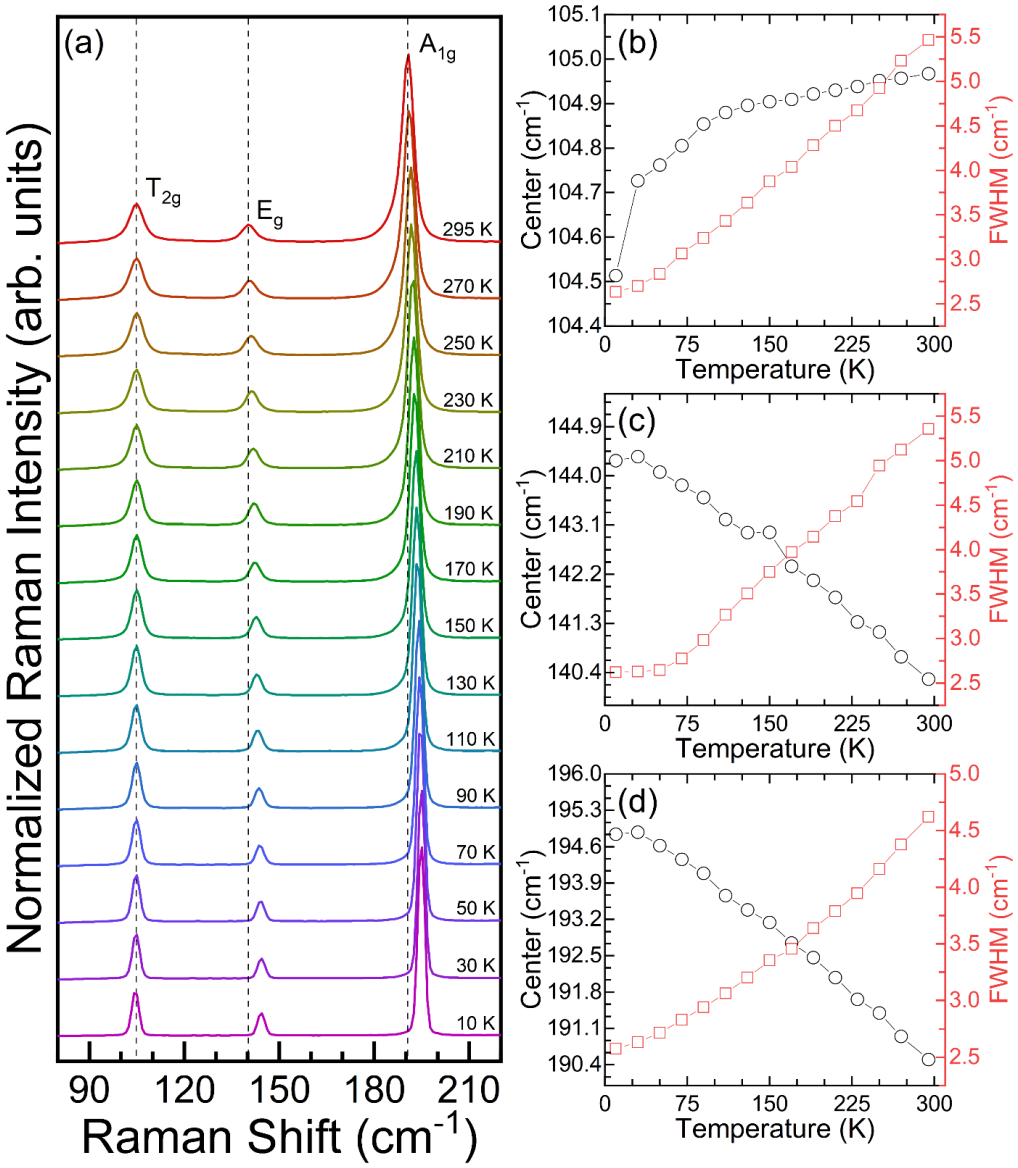

Source: elaborated by the author.

Figure 16(a) presents the calculated electronic band structure of Rb_2SnBr_6 by DFT. This 0D MHP exhibit a direct electronic transition at the Γ-point of 3.09 eV. From the DOS of the electronic band structure shown in Figure 16(b), the VBM and CBM are derived from the splitting of $[SnBr_6]^{2-}$ octahedra molecular orbital, with a nonbonding Br *p*-state at the VBM, and single bonding Sn-Br (*s*-*p*) state at the CBM [106,134].

Figure 16 – (a) Electronic band structure and (b) electronic DOS of Rb_2SnBr_6 calculated at the HSE06 level of theory. (c) Normalized (measured) absorbance spectrum of Rb_2SnBr_6 with the direct-Tauc plot in the inset. The calculated bandgap (3.09 eV) is consistent with the experimental optical bandgap (2.960 eV)

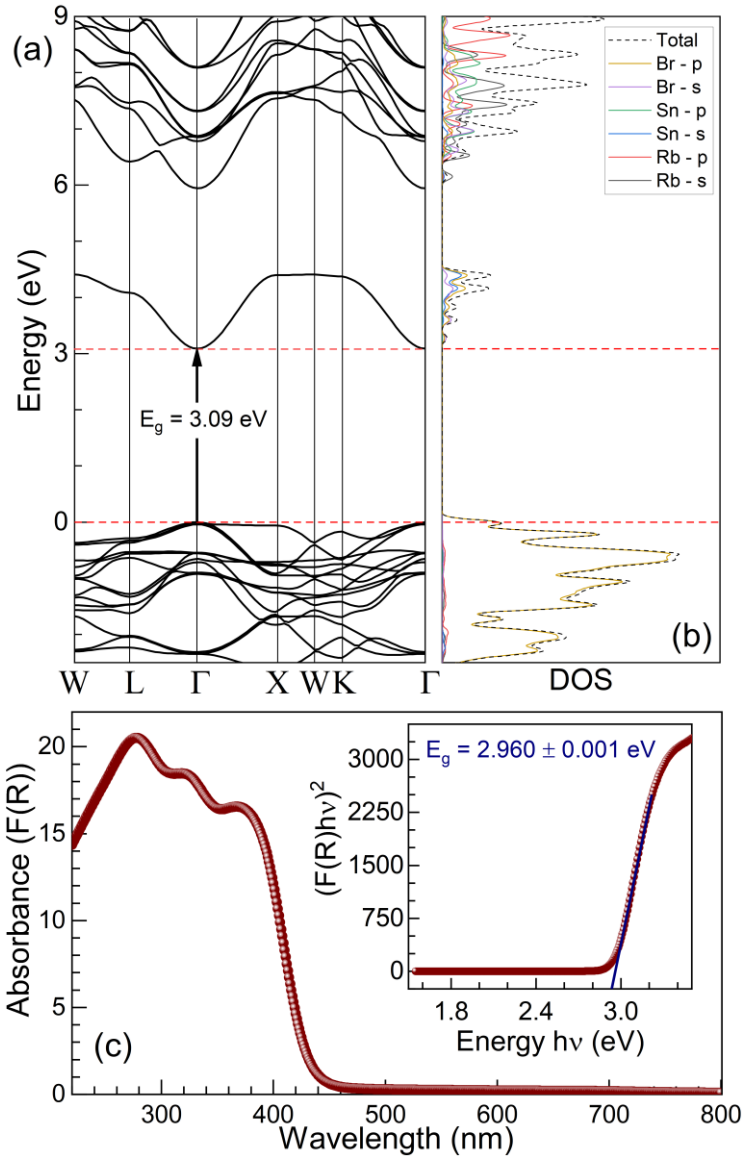

Source: elaborated by the author.

The CBM has a gradient band edge from the mixing and delocalization of Sn *s* and Br *p* states, while the VBM presents less dispersive features from the fully oxidized Sn^{4+}, unlike conventional 3D tin halide with partially oxidized Sn^{2+} and filled valence subshell [106], indicating the presence of light electrons and heavy holes as can be seen from the conductivity effective masses $\bar{m}_e$ and $\bar{m}_h$ of electron and hole, respectively, with values of $\bar{m}_e = 0.445m_0$ and $\bar{m}_h = 1.12m_0$ where m_0 is the electron rest mass. These values of $\bar{m}_e$ and $\bar{m}_h$ were calculated, as mentioned in Chapter 3, from the harmonic average of their respective effective

masses from the VBM and CBM along the $\Gamma \rightarrow X$, $\Gamma \rightarrow K$ and $\Gamma \rightarrow L$ directions [115,116], as illustrated in Figure 17.

Figure 17 – Effective masses of the electron and hole calculated from the VBM and CBM along the (a) $\Gamma \rightarrow X$, (b) $\Gamma \rightarrow K$ and (c) $\Gamma \rightarrow L$ directions of the high symmetry points from the harmonic approximation

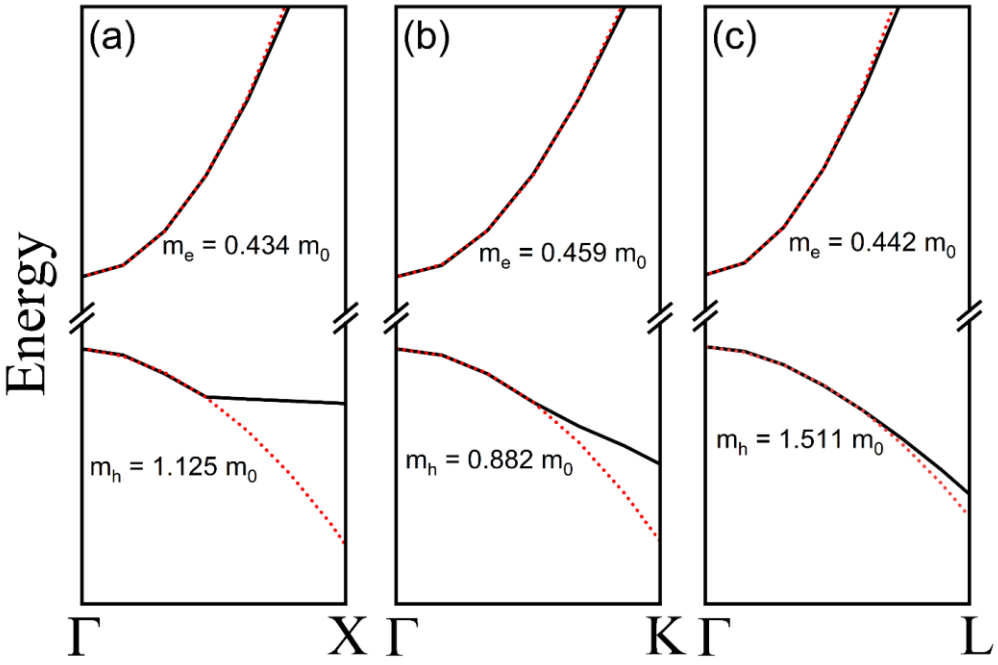

Source: elaborated by the author.

UV-Vis DRS in polycrystalline samples at room temperature was conducted to experimentally determine the optical bandgap of Rb_2SnBr_6, with the obtained reflectance spectrum converted to absorbance using the Kubelka-Monk function $F(R)$ as shown in Figure 16(c). The optical absorption edge was located around 450 nm and the energy bandgap E_g was estimated by extrapolating the linear direct-Tauc plot given by $[F(R)E]^2 \propto (E - E_g)$, where E is the energy, obtaining $E_g = 2.960 \pm 0.001$ eV. This experimental bandgap aligned very close with the theoretical bandgap obtained through DFT calculations and it is in good agreement with other isomorphous perovskites [184,185].

The PL spectrum of Rb_2SnBr_6 at 10 K under 405 nm excitation (3.06 eV) showed in Figure 18(a) revealed a broad emission around 1.93 eV (642 nm) and a FWHM of 202 meV, which was fitted by a Gaussian peak. Such broadband and large Stokes shift energy is usually found in 0D MHPs and are attributed to STE, where strong EPC plays a crucial role, or to a wide distribution of states inside the bandgap that behave as traps to charge carriers where

below-gap photons can be emitted [64,186]. To further verify the origin of the Rb_2SnBr_6 emission band, the integrated PL intensity dependence on excitation power at 10 K was performed, as illustrated in Figure 18(b). An increase in intensity and a small redshift of 1 meV on the PL peak was observed while the excitation power increased from 104 µW to 319 µW. The general relation of integrated PL intensity $I_{PL} = I$ at low-temperatures and excitation power P is described as $I \propto P^k$, where the exponent k lies on the ranges $0 < k < 1$ for free-to-bound transitions or donor-acceptor pairs (DAP) recombination and $1 < k < 2$ for excitonic emission [187]. Excitation energies close to the bandgap energy tend to result in a linear relation between I and P for excitonic recombination process that agreed with the obtained data, as illustrated in Figure 18(c), which shows the plot of I vs P with $k = 1.00 \pm 0.04$. The redshift behavior contrasts with the characteristic blueshift of DAP recombination, which excluded this possibility of emission mechanism [64].

Figure 18 – (a) PL spectrum at 10 K of Rb_2SnBr_6. (b) PL emission dependence of Rb_2SnBr_6 PL at 10 K on excitation power. (c) A plot of the integrated PL intensity vs power was obtained from (b)

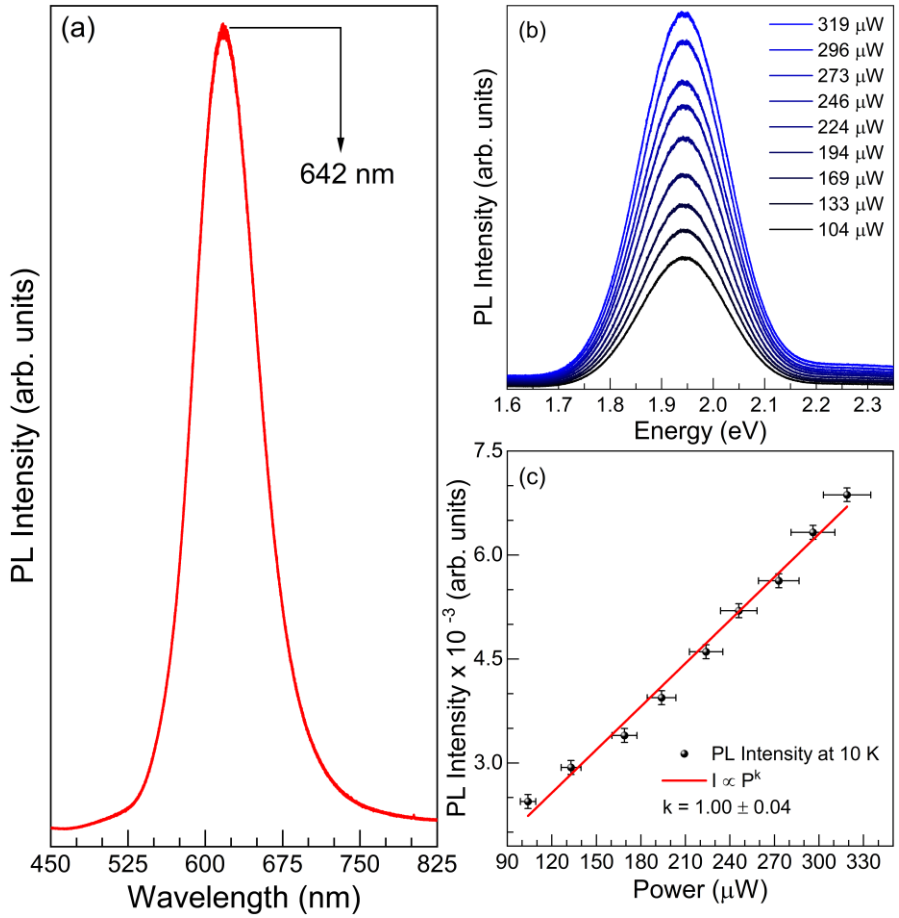

Source: elaborated by the author.

Additionally, free-to-bound transitions are identified as acceptor or donor levels that bind carriers and become ionized at higher temperatures, leading to emission bands from free carriers [90,188]. That was not observed on the temperature-dependent PL spectra in Figure 19(a) once the peak energy and intensity monotonically decreased from 10 K until its quenching around 180 K with no other radiative emission bands detected. Thus, the PL emission of Rb_2SnBr_6 was confirmed to arise from excitonic recombination mechanisms.

Figure 19 – (a) Temperature-dependent PL spectra of Rb_2SnBr_6. The inset shows the temperature dependence of peak energy. (b) Integrated PL intensity as function of temperature. The green curve represents the fit using the Arrhenius equation. (c) PL FWHM evolution on temperature. The red and blue curves represent the fits used in this work to evaluate the EPC strength

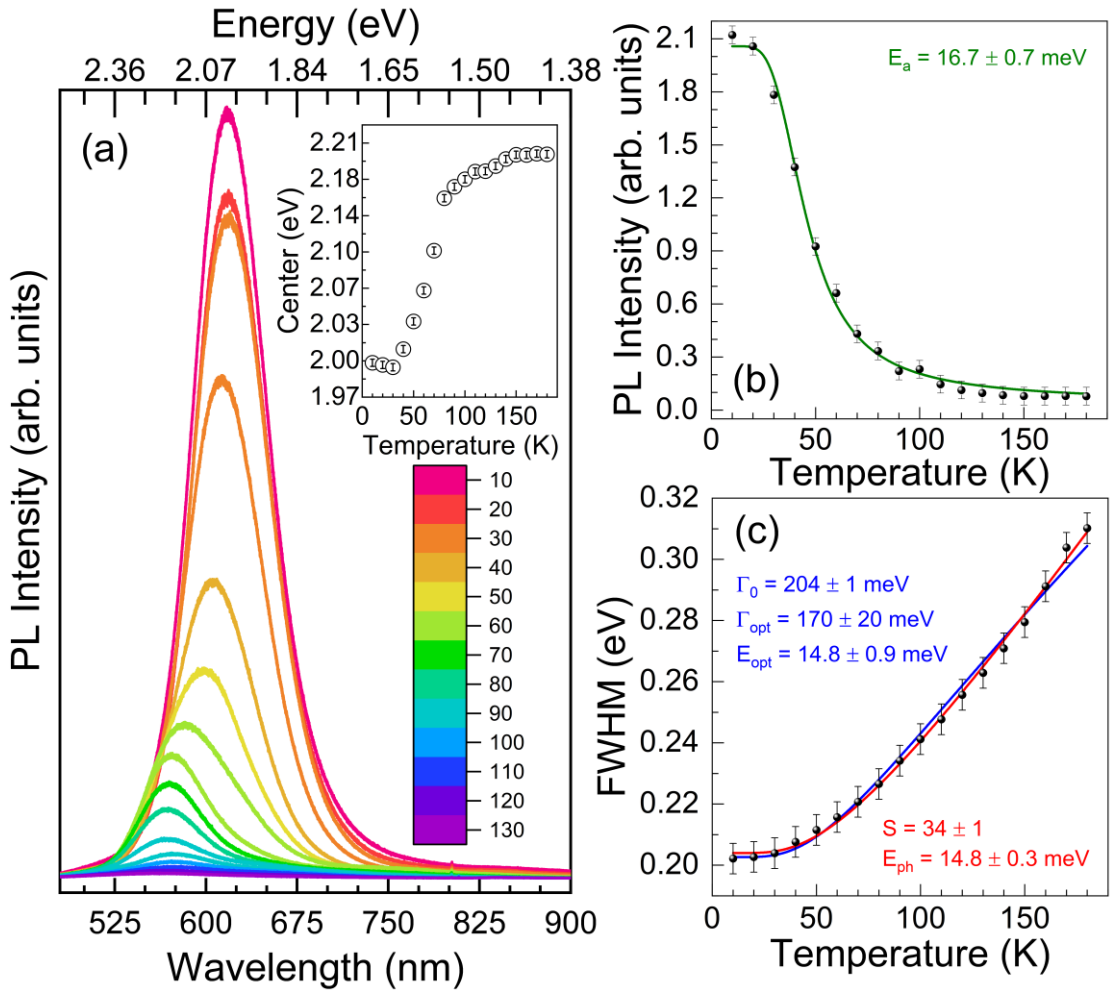

Source: elaborated by the author.

The PL emission center, under 405 nm excitation and upon increasing temperature from 10 K, redshifts from 1.93 eV to 2.20 eV until 180 K, where no PL emission

could be detected. Moreover, the PL thermal quenching behavior was modeled considering the Arrhenius equation described in Equation (11), as shown in Figure 19(b), with estimated activation energy E_a = 16.7 ± 0.7 meV, which was close to the quenching temperature of 180 K (≈ 16 meV). The absence of emission beyond 180 K suggested that the calculated activation energy is associated with the nonradiative recombination process.

To evaluate the EPC strength involved in the luminescence behavior of Rb_2SnBr_6, the temperature dependence of PL FWHM presented in Figure 19(c) was investigated based on two perspectives. The first model used to examine the PL linewidth was the one described by Equation (3) in Chapter 2 with respect to the extrinsic contributions from inhomogeneous broadening caused by local variations in electronic properties across the lattice, as well as for intrinsic contributions from homogeneous broadening due to optical and acoustic phonon scattering within the STE band. This provides insights into the dominant contributions to the temperature dependence of the PL linewidth. Based on the previous analysis about the integrated PL intensity dependence on excitation power that excluded DAP or free-to-bound recombination process and the linear increase of FWHM experimental data as it approximates the quenching temperature, as seen in Figure 19(c), which does not agree with the asymptotic behavior expected from the exponential term associated with ionized impurities in the last term on the right-hand side of Equation (3), the assumption of $\Gamma_{imp} = 0$ is valid. Furthermore, at the low-temperature range, the optical phonon contributions from the Bose-Einstein distribution function give a gradient of zero in the regime of $E_{opt} < k_B T$. However, the significantly lower energies of acoustic phonons result in a non-zero gradient of Γ_{ac} as predicted by the linear dependence on temperature of the FWHM as shown by the second term on the right-hand side of Equation (3) [74]. From Figure 19(c), it was seen that the gradient tends to vanish for the lowest temperatures, indicating negligible contribution from acoustic modes ($\Gamma_{ac} \approx 0$) which was further verified with the fit convergence when $\Gamma_{ac} \rightarrow 0$. Therefore, it was apparent that Fröhlich interactions through LO phonons played a major role in PL broadening temperature dependence.

Thus, after fitting the PL FWHM with Equation (3) considering only the coupling between excitons and LO phonons from the Fröhlich mechanism and the temperature-independent inhomogeneous broadening (blue curve in Figure 19(c)), the values of Γ_0 = 204 ± 1 meV, Γ_{LO} = 170 ± 20 meV, and E_{opt} = 14.8 ± 0.9 meV were obtained. The energy E_{opt} was closely related with $\delta_{as}(T_{1u})$ LO phonon mode at 120 cm^{-1} (≈ 15 meV) obtained by IR analysis, which suggested that long-range Fröhlich interactions mediated by LO phonons are the

dominant mechanisms of EPC that impact PL broadening, that is commonly expected in polar semiconductors as is the case for Rb_2SnBr_6 [56,148]. In the present case, the Γ_{LO} parameter measured the strength of EPC that was notably higher than in 3D perovskites [74,189], corroborating the strong EPC typically observed in LDMHPs.

The second model used to evaluate the EPC strength through the FWHM dependence on temperature was described by Equation (9) in Chapter 2 concerning the Huang–Rhys factor S related to the number of emitted phonons with energy E_{ph} along the PL emission and quantifies the degree of lattice distortions involved in the self-trapping mechanism. The temperature-dependent FWHM fitted with Equation (9) (red curve in Figure 19(c)) yielded E_{ph} = 14.8 ± 0.3 meV and S = 34 ± 1. The obtained phonon energy matches with the LO phonon energy $\hbar\omega_{LO}$ of the $\delta_{as}(T_{1u})$ mode previously found, supporting that the EPC of Rb_2SnBr_6 arises from Fröhlich interactions with LO phonons. The strong EPC revealed by the Huang–Rhys factor agreed with the high value obtained from Γ_{LO} and is compatible with the assumption of exciton self-trapping underlying the below-gap broad luminescence from STE [65,90,92,185].

In the Fröhlich theory, the polaron formation arises from the interactions between carriers and LO phonons, and the coupling strength of this carrier-vibration relation is determined by the Fröhlich parameter α as defined by Equation (2) in Chapter 2. Using the first-principles calculated effective masses as well as the experimental values for $E_{opt} = \hbar\omega_{LO}$, ε_∞ and ε_s, Equation (2) yielded Fröhlich parameters of 2.78 and 4.41 for the electron and hole, respectively. Although the calculated α for the electrons is in the same range of 1 – 3 for conventional 3D halide perovskites (for both electrons and holes) [56,148,190], the calculated hole-phonon coupling is well above this range as a direct consequence of the heavy hole mass compared to the electron found through DFT calculations. Upon hole interactions with surrounding lattice, its mass is further increased by the hole-polaron mass $\bar{m}_{hp} \approx (1 + 0.17\alpha + 0.025\alpha^2)\bar{m}_h = 2.49m_0$, that can lead to hole localization and consequently exciton trapping by its positive carrier [65]. Thus, it is proposed that STE formation in Rb_2SnBr_6 is mediated by hole localization upon Fröhlich interactions with the lattice vibration. This kind of exciton formation has been observed in organic and molecular crystals [191], and total inorganic salts such as AgCl [64,192]. Compared to the 3D halide perovskites, where the $[BX_6]$ octahedra are surrounded by a corner-sharing framework, the isolated $[BX_6]$ octahedra configuration of 0D MHPs possess more degrees of freedom and hence are easily distorted upon interaction between exciton's charge carriers and octahedra vibrations. This results in

stronger EPC and, together with the significant enhancement of the hole-polaron mass, can promote STE via hole trapping.

5 ELECTRON-PHONON COUPLING IN LOW-DIMENSIONAL HALIDE PEROVSKITES WITH CHIRAL ORGANIC SPACERS

In addition to 0D MHPs, low dimensionality can be achieved from 3D perovskites by incorporating organic spacer cations between the inorganic metal-halide octahedral layers, as illustrated in Figure 20(a). This structural modification gives rise to the so-called layered two-dimensional metal halide perovskites (2D MHPs), which are generally expressed by the chemical formula $S_pA_{n-1}B_nX_{3n+1}$ [193]. In this notation, n denotes the number of inorganics $[BX_6]^{4-}$ octahedral layers separated by the organic spacer S and, for $n > 1$, the compounds are sometimes called quasi-2D perovskites [194]. Depending on the nature of the organic cation, two principal 2D MHPs families can be formed, as illustrated in Figure 20(b). When the spacer is a monofunctional ammonium ($p = 2$), it leads to the formation of Ruddlesden–Popper phases, in which adjacent inorganic layers are held together by weak van der Waals interactions [195,196]. Conversely, bifunctional ammonium cations ($p = 1$) give rise to Dion–Jacobson phases, where the inorganic layers are directly connected through stronger hydrogen bonding or electrostatic interactions through the spacers, resulting in enhanced structural stiffness [193,197]. Through molecular engineering, parameters such as the interlayer distance, dielectric confinement, energy band structure (Figure 20(c)), and exciton dynamics occurring in the inorganic framework can be tuned [198,199]. Furthermore, these 2D organic–inorganic systems exhibit strong quantum and dielectric confinement, leading to larger exciton binding energies and tunable optical properties varying from narrow and small Stokes shifted PL as for most regular <100>–oriented 2D MHPs, to broadband emissions with large Stokes shift energy for <110>–oriented corrugated 2D MHPs [48].

Figure 20 – Schematic diagram of the 2D MHPs. (a) Comparison of 3D ABX_3 perovskite and its derived 2D and quasi-2D perovskites. (b) Differences of the crystal structure from Ruddlesden–Popper (RP) and Dion–Jacobson (DJ) configurations. (c) Energy band structures between the organic and inorganic layers of the 2D and quasi-2D perovskites

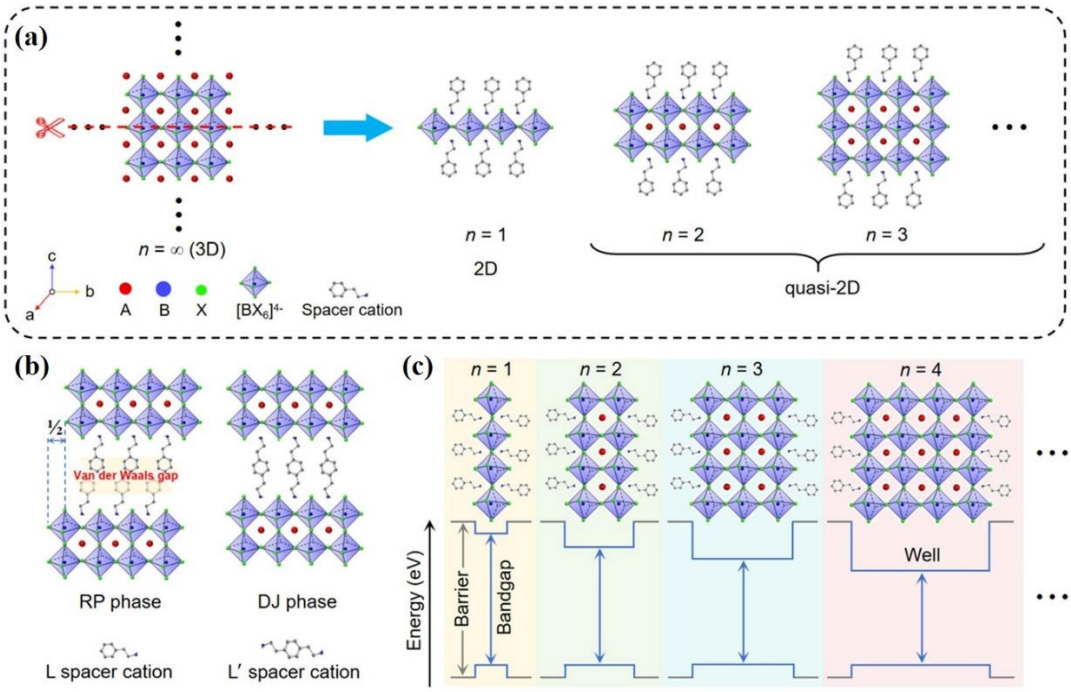

Source: adapted from reference [199].

Depending on the choice of organic cation, one-dimensional metal halide perovskites (1D MHPs) can be formed. These structures are characterized by corner-, edge-, or face-sharing metal halide octahedra, as illustrated in Figures 21(a–c), which form 1D networks held together by organic cations [200]. The configurations of these networked chains can be zigzag, linear, bilinear, or even tubular, with chemical formulas that vary based on the specific organic cations and connectivity methods employed [201]. Examples of some 1D MHPs are demonstrated in Figures 21(e,f). The reduced dimensionality relative to 2D MHPs enhances quantum confinement effects, generally leading to broadband PL emission, where the metal–halide octahedra exhibit bond lengths that are easily distorted, favoring carrier-lattice interactions and the formation of short-range polarons which in turn trap excitons into STE states [202,203].

Figure 21 – Schematic illustrations of (a) corner-sharing, (b) edge-sharing, and (c) face-sharing metal halide octahedral chains of 1D MHPs. (e) One-dimensional arrangement of 1D $(C_4H_{10}N)MnBr_3$ perovskite. (f) Crystal structure of 1D lead bromide $(C_5H_{16}N_2)Pb_2Br_6$ perovskite

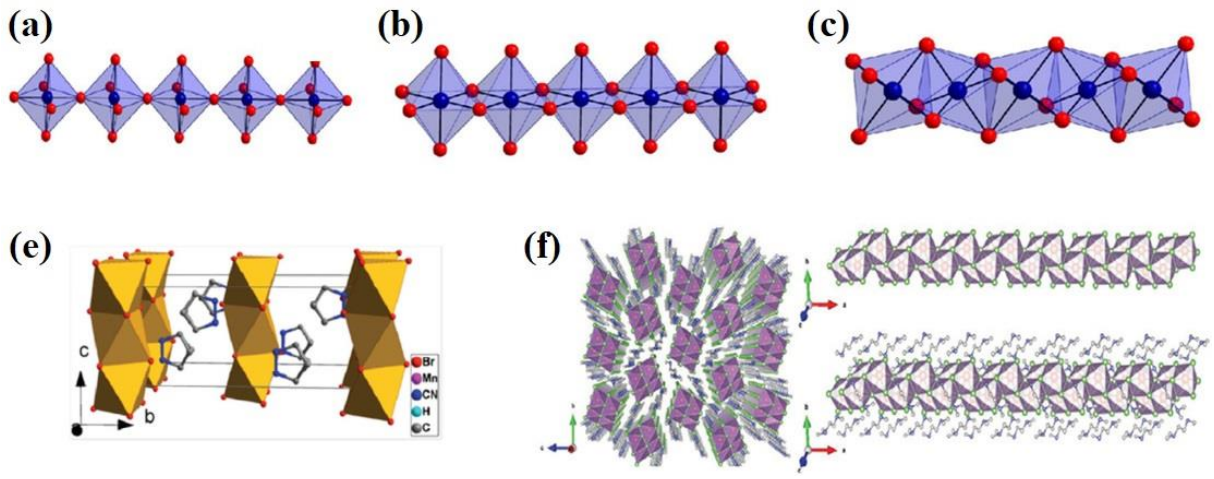

Source: adapted from reference [201].

Among the wide variety of organic molecules reported in the literature for synthesizing 2D and 1D MHPs, one family of spacers that has gained significant attention consists of chiral molecules that lack an internal plane of symmetry, meaning they are non-superimposable on their mirror images, which are known as enantiomers [204]. Some examples of chiral organic spacers are shown in Figure 22(a). Chiral materials exhibit a range of unique physical properties, including circular dichroism, circularly polarized photoluminescence (CPL), non-linear optical effects, and chirality-induced spin selectivity (CISS) [205–208]. The incorporation of such chiral molecules into LDMHPs induces lattice asymmetry through structural distortion, thereby giving rise to intrinsic chiroptical properties essential for applications in spintronics and polarization optics [209–211].

Figure 22 – (a) Some examples of chiral organic spacers used in chiral LDMHPs: MBA (α-methylbenzylammonium), CHEA (1-cyclohexylethylammonium), MPEA (β-methylphenethylammonium), 3APD (R-3-aminopiperidine), NEA (1-(1-naphthyl)ethylammonium), DACH (1,2-diaminocyclohexane), 2OA (2-octylamine), 3AQ (3-ammonioquinuclidinium), 3AP (3-ammoniopyrrolidinium), 3-FP (3-fluoropyrrolidinium), and CMBA (1-(4-chlorophenyl)-ethylammonium. (b) Crystal structures of 2D and 1D chiral lead iodide perovskites and of a 2D racemic achiral perovskite based on MBA

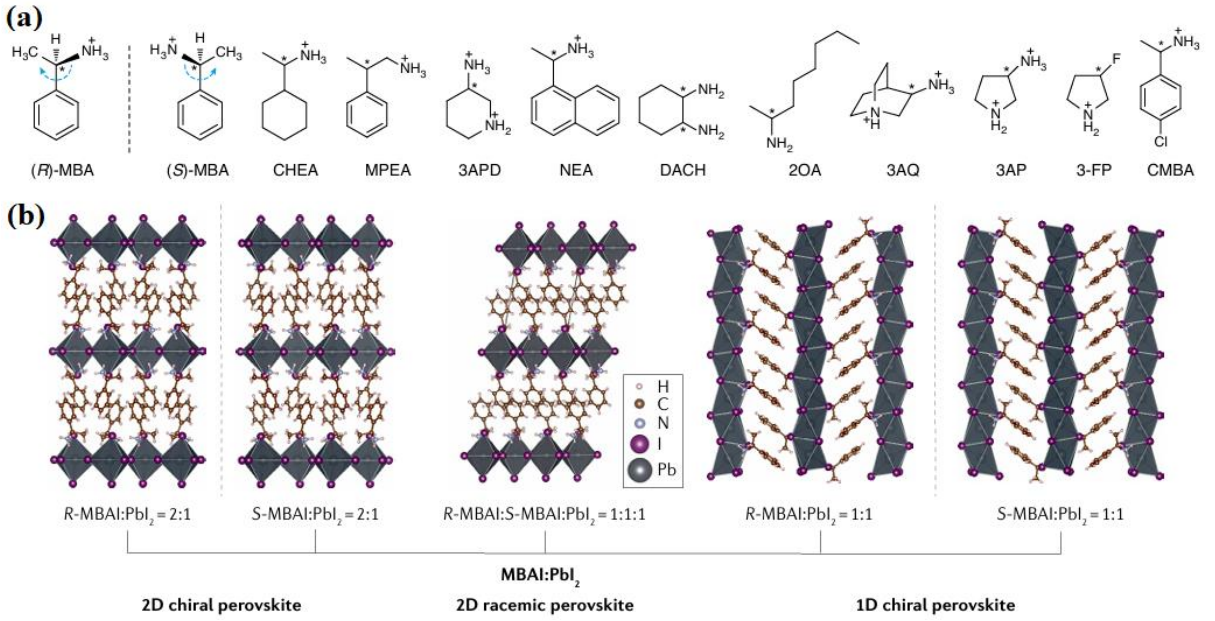

Source: adapted from reference [211].

Chiral LDMHPs crystallize in one of the 65 Sohncke space groups, which lack mirror or inversion symmetry as a necessary condition for chiral crystal structures. These materials are often synthesized using the enantiomers of the organic spacers to yield mirrored crystal structures, as illustrated in Figure 22(b) for lead iodide perovskites based on the R- and S-enantiomers of α-methylbenzylamine (MBA). The chirality transfer mechanism from the organic spacers to the inorganic framework occurs via asymmetric hydrogen-bonding interactions between the ammonium groups of the chiral cations and the halides of the inorganic lattice [212]. Beyond imparting chiroptical activity to the LDMHPs, these interactions lead to structural distortions within the inorganic octahedra that are fundamental to the EPC and significantly influence optoelectronic properties, including (non-polarized) PL and excitonic dynamics. Additionally, LDMHPs can be synthesized using a racemic mixture, which consists of equal amounts of both enantiomers, which typically retains the dimensionality of the corresponding chiral compounds. However, depending on the chemical composition, the use of

a racemic mixture may alter the inorganic arrangement or even trigger a dimensionality switch, thereby modulating the resulting optoelectronic properties [213,214].

To investigate how chiral organic spacers modify structural and optoelectronic properties, and how these modifications influence the EPC, this chapter is dedicated to the study of lead bromide perovskites based on MBA enantiomers and their corresponding racemic mixture (Rac-MBA). By using several characterization techniques, this chapter explores dimensionality shifting and its subsequent effects on EPC and PL behavior. These findings provide insights into the structural and optoelectronic behavior of LDMHPs incorporating chiral cations.

5.1 Dimensionality reduction and emission tuning in low-dimensional lead bromide perovskites with chiral α-methylbenzylammonium cations

Low-dimensional lead bromide perovskites were synthesized using R-/S-/Rac-α-methylbenzylamine (R-/S-/Rac-MBA) as organic cation spacers using the slow evaporation method described in Chapter 3. These organic spacers, when protonated and inserted in the perovskite compounds, comprise a secondary carbon bonded to a phenyl, a methyl, and an ammonium group, as illustrated in Figure 23.

Figure 23 – Chemical structure of the protonated organic cations S-α-methylbenzylamine (S-MBA, on left) and R-α-methylbenzylamine (R-MBA, on right)

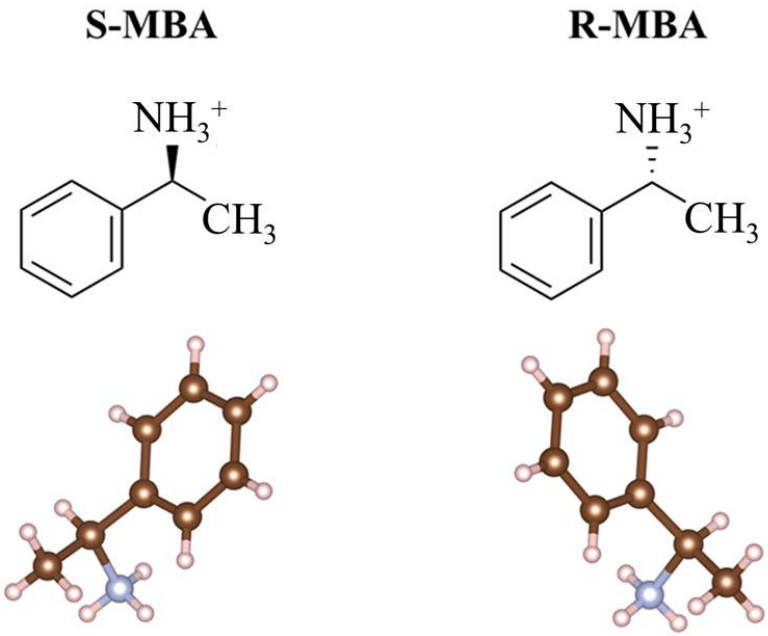

Source: elaborated by the author.

Figures 24(a,b) show the SEM images of the obtained microcrystals. The S-MBA based microcrystals were in the form of flat needle-like crystals ranging from 50 to 150 μm with lamellar conformation. The same crystals' shape and morphology were obtained for the R-MBA based perovskite. In contrast, the use of the racemic mixture yielded prolonged block-shaped crystals with axes ranging from 50 to 100 μm with three well-defined dimensions. Figures 24(c,d) show the room-temperature PXRD pattern along with Rietveld refinement of the as-prepared (R-/S-MBA) samples. Both compounds crystallized as mirror images of 2D Ruddlesden–Popper perovskites in the form of (R-/S-MBA)$_2$PbBr$_4$ with orthorhombic crystal structure and Sohncke $P2_12_12_1$ space group [215,216]. The PXRD also detected a very small amount of the (R-/S-MBA)PbBr$_3$ 1D phase, which could be observed along with the simulated PXRD patterns of both the 2D and the (R-/S-MBA)PbBr$_3$ phases, as illustrated in Figure 25.

Figure 24 – SEM images of the (a) (S-MBA)$_2$PbBr$_4$ and (b) (Rac-MBA)$_3$PbBr$_5$·H$_2$O microcrystals. PXRD data along with Rietveld refinements for the chiral perovskites (c) (S-MBA)$_2$PbBr$_4$ and (d) (R-MBA)$_2$PbBr$_4$. Tick marks below the XRD pattern indicate the expected Bragg reflection positions considering the orthorhombic phase with $P2_12_12_1$ space group symmetry for both samples. Asterisks (*) stands for the (002) plane from traces of (R-/S-MBA)PbBr$_3$. (e) PXRD and simulated Bragg reflections considering a monoclinic monohydrated 1D (Rac-MBA)$_3$PbBr$_5$·H$_2$O phase with a $C2/c$ space group symmetry. Green and blue arrows indicate the most intense diffraction peaks that distinguish the 2D and monohydrated 1D perovskites

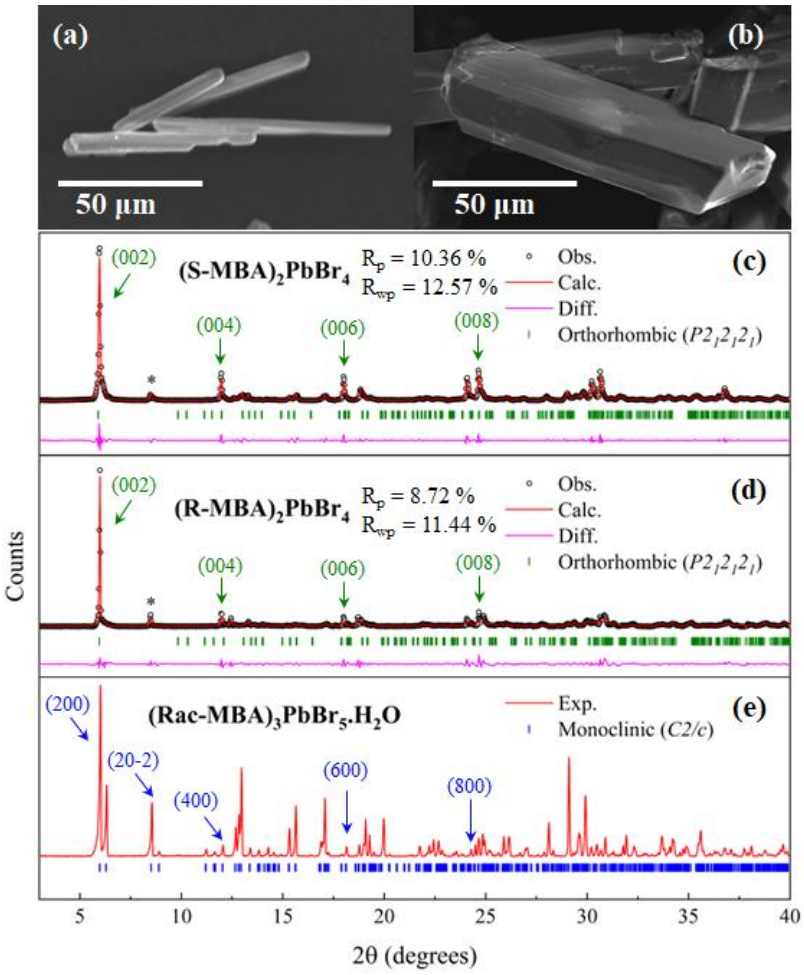

Source: elaborated by the author.

Figure 25 – Powder and simulated XRD of 2D and 1D lead bromide phases based on (a) S-MBA and (b) R-MBA cations

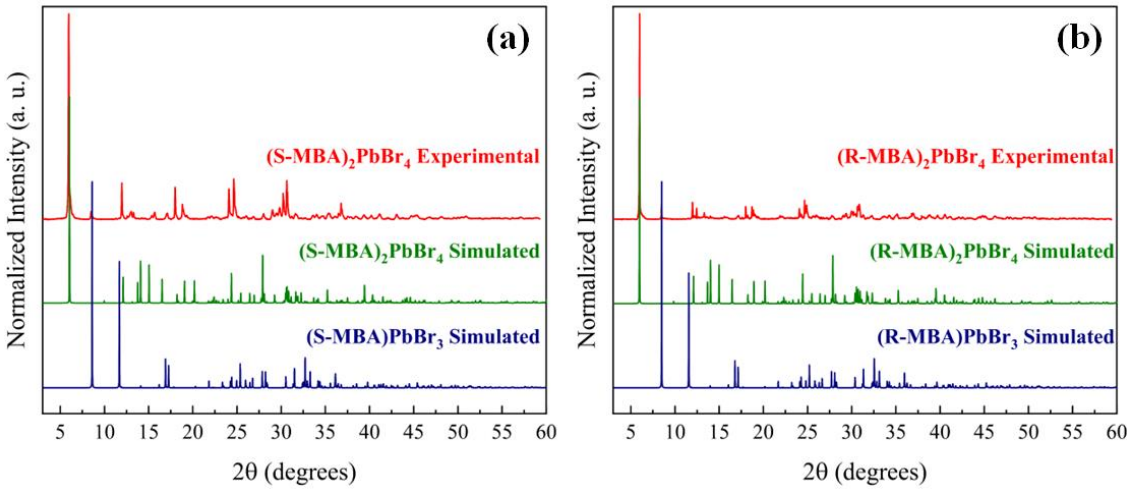

Source: elaborated by the author.

Although the same synthesis procedure was adopted to synthesize 2D perovskites with the racemic mixture in the organic cation site, the Bragg reflections did not belong to the 2D orthorhombic crystal structure as observed for chiral molecules. SCXRD of the obtained Rac-MBA based microcrystals revealed the formation of a completely different crystal phase belonging to a monoclinic monohydrated 1D $(Rac\text{-}MBA)_3PbBr_5 \cdot H_2O$ perovskite belonging to the *C2/c* space group that was first reported by Billing and Lemmerer [217,218], as shown in Figure 24(e).

The different dimensionalities of the synthesized LDMHPs are illustrated in Figure 26. The 2D Ruddlesden–Popper $(R\text{-}/S\text{-}MBA)_2PbBr_4$ perovskites consist of inorganic layers of corner-sharing $PbBr_6$ octahedra in the (0 0 2*l*) planes (where *l* is an integer) separated by bilayers of R-/S-MBA cations along the *c* axis as shown in Figure 26(a)**.** Weak van der Waals interactions stabilize the organic layers. In contrast, the bonding between the organic and inorganic layers is mediated by hydrogen bonding. On the other hand, the 1D $(Rac\text{-}MBA)_3PbBr_5 \cdot H_2O$ perovskite has chains of corner-shared $PbBr_6$ octahedra running along the *b* axis in a zigzag pattern. Organic cations surround each chain arranged radially, with their ammonium heads directed toward the chains to form hydrogen bonds with water molecules positioned between adjacent chains, as illustrated in Figure 26(b). Comparative lattice parameters of the $(R\text{-}/S\text{-}MBA)_2PbBr_4$ and $(Rac\text{-}MBA)_3PbBr_5 \cdot H_2O$ LDMHPs are displayed in Table 4 and SCXRD data together with refinement parameters are available in Table 5.

Figure 26 – (a) Crystal structures of the 2D perovskites $(S\text{-}MBA)_2PbBr_4$ and $(R\text{-}MBA)_2PbBr_4$. (b) (left) Schematic representation of the four families of $PbBr_6$ octahedra formed in the $(Rac\text{-}MBA)_3PbBr_5{\cdot}H_2O$ crystal inside a unit cell. (right) 1D arrangement of $(Rac\text{-}MBA)_3PbBr_5{\cdot}H_2O$

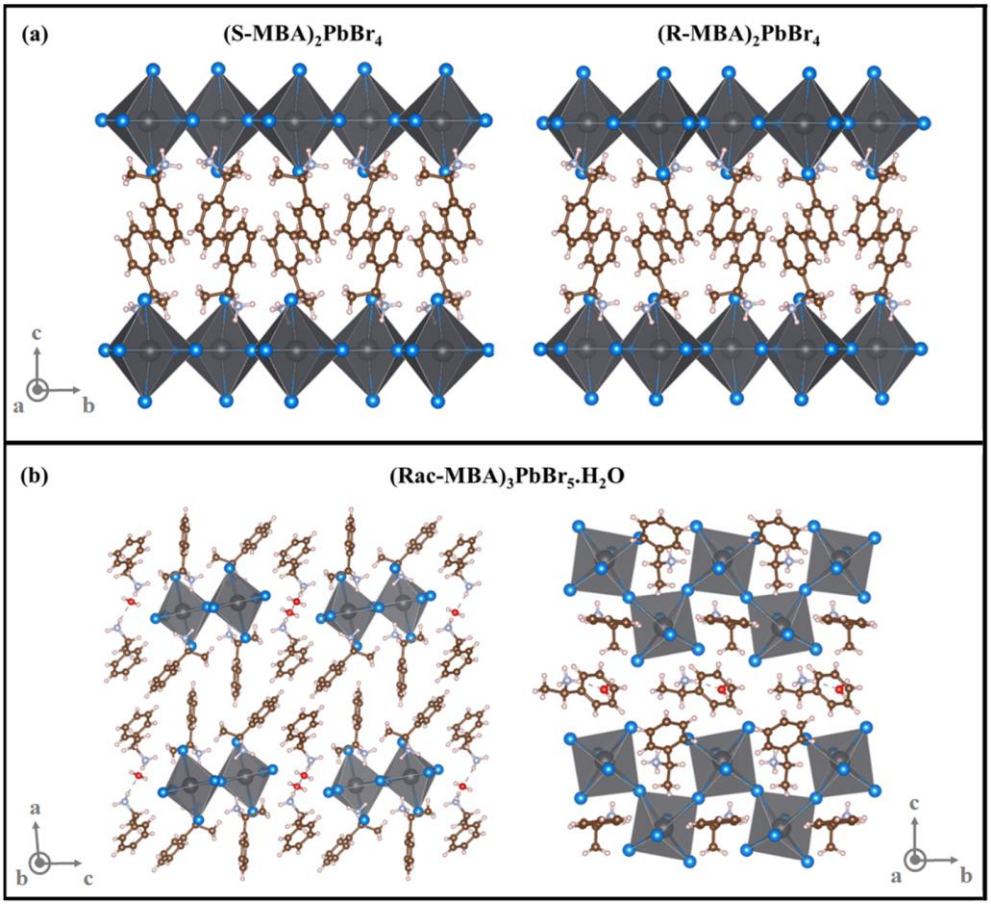

Source: elaborated by the author.

Table 4 – Experimental unit cell parameters of $(S\text{-}MBA)_2PbBr_4$, $(R\text{-}MBA)_2PbBr_4$ and $(Rac\text{-}MBA)_3PbBr_5{\cdot}H_2O$ LDMHPs

Compound	$(S\text{-}MBA)_2PbBr_4$	$(R\text{-}MBA)_2PbBr_4$	$(Rac\text{-}MBA)_3PbBr_5{\cdot}H_2O$
Crystal System	Orthorhombic	Orthorhombic	Monoclinic
Space group	$P2_12_12_1$	$P2_12_12_1$	$C2/c$
a (Å)	8.890(1)	8.83980(10)	29.333(4)
b (Å)	9.3016(2)	9.31140(3)	8.1618(9)
c (Å)	29.1967(3)	28.96556(6)	27.905(3)
β (°)	90.00	90.00	92.467(5)
Volume (Å^3)	2414.4(9)	2384.172(5)	6674.70(10)

Source: elaborated by the author.

Tabel 5 – Crystal data and refinement parameters of (Rac-MBA)$_3$PbBr$_5$·H$_2$O from SCXRD measurements

Empirical formula	$C_{24}H_{38}Br_5N_3OPb$
CCDC number	2466728
Formula weight	991.31
Temperature (K)	298
Crystal system	Monoclinic
Space group	*C*2/*c*
a (Å)	29.333(4)
b (Å)	8.1618(9)
c (Å)	27.905(3)
β (°)	92.467(5)
Volume (Å^3)	6674.70(10)
Z	8
ρ_{calc} (gcm^{-3})	1.973
μ (mm^{-1})	11.062
F(000)	3744
Crystal size (mm^3)	0.106×0.085×0.083
Crystal colour	Clear light colourless
Crystal shape	Block
Radiation	MoK_α (λ=0.71073 Å)
2θ range (°)	5.18 to 58.32
Index ranges	-40 ≤ h ≤ 40 -11 ≤ k ≤ 11 -38 ≤ l ≤ 38
Reflections collected	102570
Independent reflections	8992
Completeness	99.9 %
Goodness-of-fit on F^2	1.010
Final *R* indexes (*I*≥2σ(*I*))	R_1 = 0.0269 wR_2 = 0.0507
Final *R* indexes (all data)	R_1 = 0.0489 wR_2 = 0.0577
Largest peak/hole (eÅ^{-3})	0.65/-0.69

Source: elaborated by the author.

The formation of the 1D (Rac-MBA)$_3$PbBr$_5$·H$_2$O structure, instead of the 2D phases observed for both enantiopure (R-/S-MBA)$_2$PbBr$_4$ crystals and the iodide case of (R-/S-/Rac-MBA)$_2$PbI$_4$ [219], could be attributed to steric hindrance arising from the ammonium group bonded to a secondary carbon in each enantiomer of the racemic mixture. This steric effect may hinder the interaction between the ammonium groups and the inorganic network,

preventing the stabilization of a 2D framework and probably contributing to the 1D (R-/S-MBA)$PbBr_3$ phases shown in Figure 24 [210]. A similar effect occurs in the chloride phase, where the racemic mixture yields the (Rac-MBA)$_3PbCl_5 \cdot H_2O$ structure [217]. However, the larger radius of the iodide ion may compensate for these steric effects, thereby stabilizing the 2D inorganic framework in the form of (Rac-MBA)$_2PbI_4$.

Although the 2D lead halide perovskites based on α-methylbenzylamine cations have been widely studied in the literature [215,219–221], the monohydrated phase (Rac-MBA)$_3PbBr_5 \cdot H_2O$ remains largely underexplored [218,222]. To investigate the thermal stability of (Rac-MBA)$_3PbBr_5 \cdot H_2O$, DSC measurements were performed on the hydrated LDMHP in the temperature range of 65–180 °C, as shown in Figure 27(a), where red and blue curves correspond to the heating and cooling processes, respectively. In the first heating cycle, a weak endothermic peak is observed beginning around 85 °C, likely associated with residual solution that remained even after cleaning. In addition, another endothermic event is observed starting around 110 °C, which may be associated with the removal of water from the monohydrated 1D perovskite structure as previously reported by Zhou *et al.* through thermogravimetric analysis (TGA) [222]. A third endothermic peak appears at 150 °C during heating, followed by an exothermic event at 130 °C during cooling. In the second cycle, performed on the same sample, only the endothermic peak at 150 °C and the exothermic event at 130 °C are present during the heating and cooling processes, respectively, suggesting that an irreversible structural transformation of (Rac-MBA)$_3PbBr_5 \cdot H_2O$ occurred from the release of water. To confirm this phase transformation, the room-temperature PXRD patterns of the as-grown perovskite and the same sample after thermal treatment at 120 °C for 1 hour were compared. As can be seen in Figure 27(b), the PXRD patterns were markedly different, confirming the irreversible phase transformation indicated by the DSC data. Further investigations would be need to identify the new phase driven by water removal that is beyond the scope of this work.

Figure 27 – (a) DSC data of (Rac-MBA)$_3$PbBr$_5$·H$_2$O performed at the first and second cycles. (b) PXRD of the as-grown (Rac-MBA)$_3$PbBr$_5$·H$_2$O and the new phase after water release from thermal treatment, both at room-temperature. Green tick marks on the inset represent the expected Bragg reflection positions considering a monoclinic phase with *C*2/*c* space group symmetry of the hydrated perovskite

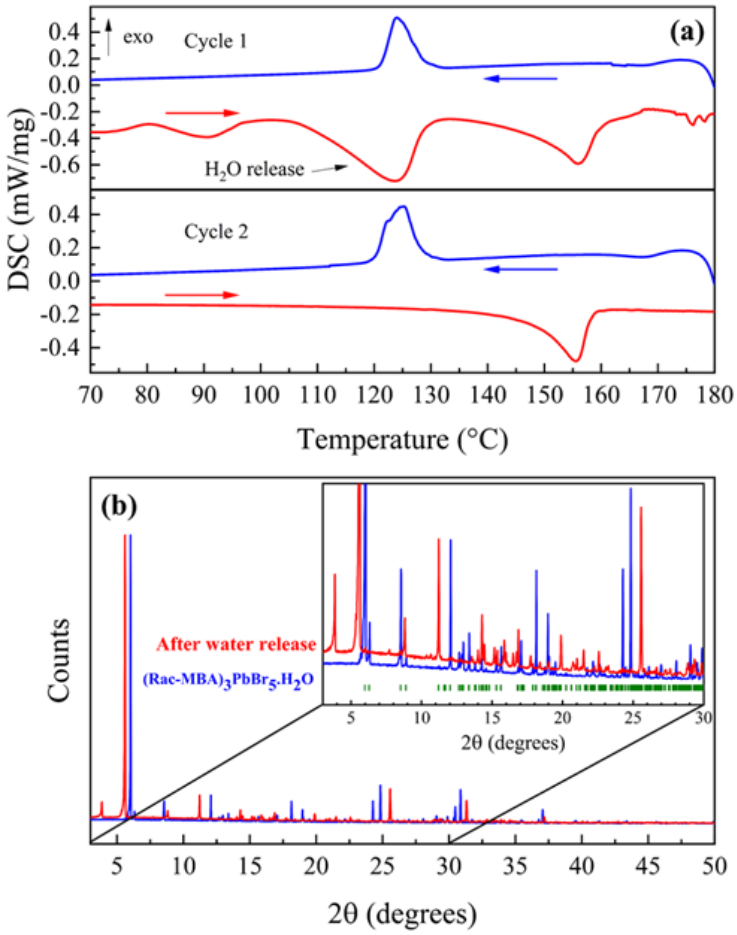

Source: elaborated by the author.

In an attempt to understand the influence of molecular chirality and dimensionality on the electronic structure of these LDMHPs, DFT calculations for both the enantiopure and racemic systems were performed, as shown in Figure 28. As expected from symmetry considerations, the R- and S-enantiomers based perovskites yielded identical band structures, with no discernible differences in electronic dispersion. The VBM comprises of Br *p*-orbitals in both cases. In contrast, the CBM is dominated by Pb *p*-states, which agrees with previous reports on halide perovskites [223,224]. The calculated bandgap was direct and located at the Γ-point, with a value of approximately 2.8 eV using the PBE functional as shown in Figure 27(a) for (S-MBA)$_2$PbBr$_4$, while the same results were obtained for (R-MBA)$_2$PbBr$_4$ (not

shown). Although this functional is known to underestimate the absolute bandgap, the relative trends remained reliable [225–227]. Notably, inclusion of SOC revealed a Rashba-like spin splitting at the CBM, with a momentum offset and energy splitting on the order of 10 meV (Figure 28(b)), as expected by the chiral-induced deformation in polar materials and the heavy Pb ion [228].

Figure 28 – Electronic band structures of enantiopure and racemic lead bromide perovskites. (a) $(S\text{-}MBA)_2PbBr_4$ without SOC, showing a direct bandgap at Γ. (b) Same system with SOC, revealing Rashba-type spin splitting at the band edges (~10 meV). The inset shows the spin texture (expectation value of the spin operator), with opposite spin components along the z-axis (S_z) depicted in green and purple. (c) $(Rac\text{-}MBA)_3PbBr_5{\cdot}H_2O$ without SOC, showing mid-gap states from undercoordinated Br atoms and a Fermi level near the conduction band

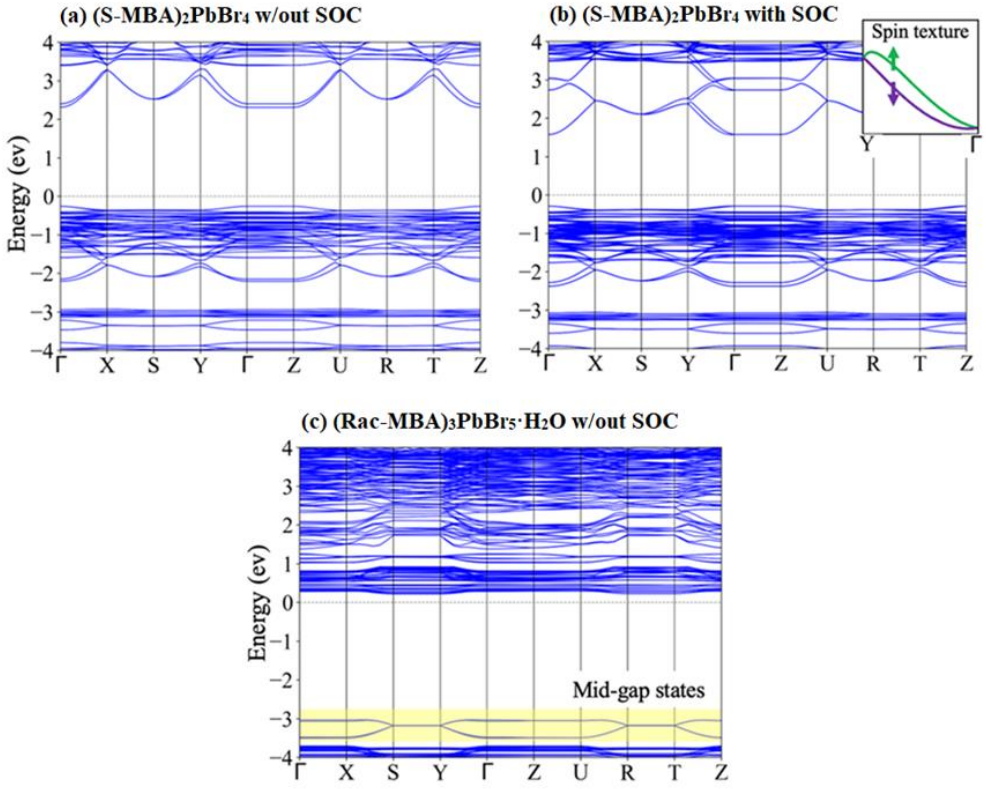

Source: elaborated by the author.

In contrast, the racemic compound $(Rac\text{-}MBA)_3PbBr_5{\cdot}H_2O$ exhibits mid-gap states derived from Br atoms probably from that lack full coordination due to the disrupted octahedral connectivity in the two-dimensional, as would be the case for the hypothetical 2D $(Rac\text{-}MBA)_2PbBr_4$ perovskite. Although partially stabilized by hydrogen bonding with water molecules, these undercoordinated Br orbitals introduce electronic states deep within the gap

region, as revealed in the unfolded band structure (Figure 46(c)). Furthermore, the Fermi level lies very close to the conduction band edge, indicating that the hydrated racemic phase behaves as an extrinsic semiconductor, likely a consequence of charge compensation mechanisms facilitated by interstitial water molecules.

Figure 29(a) shows the room-temperature UV-Visible absorption spectra of (R-/S-MBA)$_2$PbBr$_4$ and (Rac-MBA)$_3$PbBr$_5$·H$_2$O crystals. The absorption edges are situated around 345 nm for the enantiomer-based compounds, consistent with previously reported absorption spectra of powder samples of these perovskites [229]. For the monohydrated 1D phase, the absorption spectrum closely resembles that reported by Dang *et al.* [218], featuring a small peak centered around 400 nm, which can be attributed to defect-induced mid-gap states, and a strong peak at 350 nm, commonly assigned to excitonic absorption. The direct bandgap energies were determined via the Tauc plot method to be 3.74 eV and 3.47 eV for the 2D and 1D perovskites, respectively. To confirm whether the incorporation of chiral ligands resulted in chiral perovskites, circular dichroism (CD) spectroscopy was performed on thin films obtained by dissolving the crystals in DMF and spin-coating them onto quartz substrates. This approach was necessary since the as-synthesized crystals were too thick to yield a reasonable CD response. As shown in Figure 29(b), CD signals were observed for (R-/S-MBA)$_2$PbBr$_4$ around 350 nm with oppositely signed values near the absorption edge for each sample, which can be attributed to the Cotton effect [215,219], which suggested that chirality was transferred from the chiral ligands to the inorganic sublattices.

Figure 29 – Room-temperature optical properties of the (R-/S-MBA)$_2$PbBr$_4$ and (Rac-MBA)$_3$PbBr$_5$·H$_2$O perovskites. (a) Normalized absorption spectra with the Tauc plot in the inset. (b) CD spectra of the enantiomers-based perovskites. (c) Normalized PL spectra

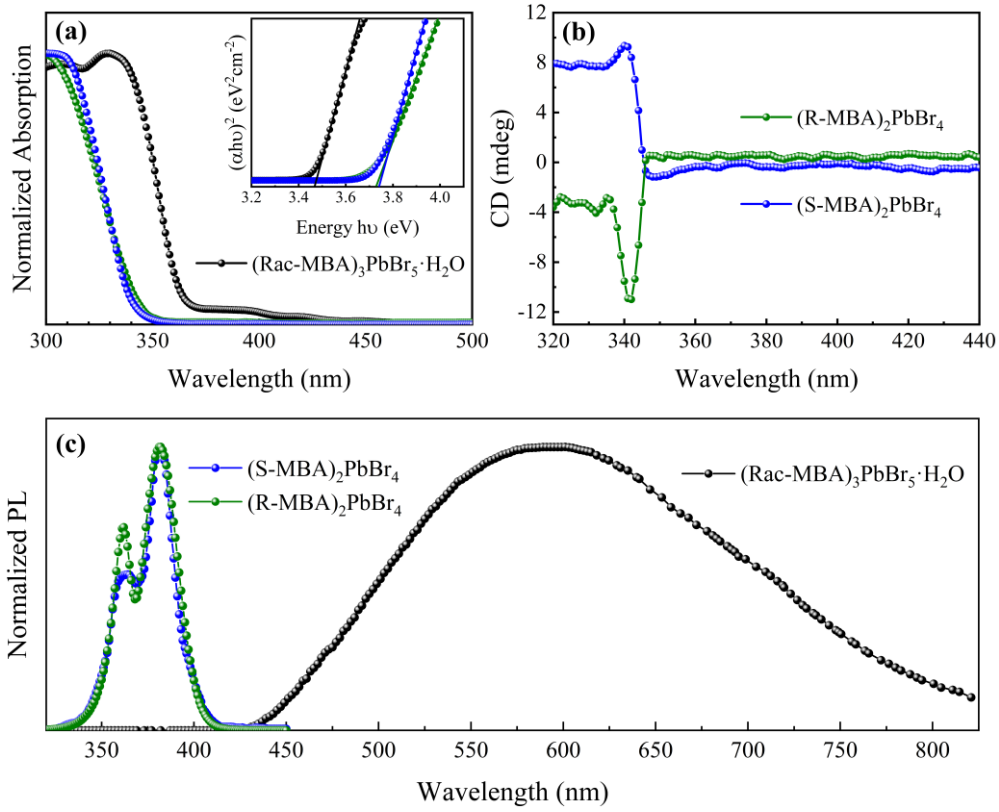

Source: elaborated by the author.

The steady-state PL spectra of the LDMHPs are shown in Figure 29(c). For the (R-/S-MBA)$_2$PbBr$_4$ compounds, two distinct narrow emissions were detected at 362 nm and 382 nm, both near the absorption edge. The higher-energy PL peak is widely attributed to free exciton emission in 2D halide perovskites [230,231], whereas the origin of the lower-energy emission remains under debate. Possible explanations include photon recycling mechanisms [232], difference between bulk and surface energy states [233], and spin splitting induced by SOC [234]. As discussed earlier, the inclusion of SOC revealed a Rashba-like spin splitting at the CBM in (S-MBA)$_2$PbBr$_4$. However, the calculated energy splitting (≈10 meV) was significantly smaller than the experimentally observed separation between the double-emission peaks (≈180 meV), suggesting that additional mechanisms may also be involved. Nevertheless, the definitive assignment of the PL peaks in the (R-/S-MBA)$_2$PbBr$_4$ compounds would require further investigations.

A different PL behavior was observed for the (Rac-MBA)$_3$PbBr$_5$·H$_2$O perovskite, which exhibited a broad-band emission (BE) centered around 600 nm, commonly STE emission

in halide perovskites [48,230]. Similar broad-band emissions were observed in the enantiomer-based 1D perovskites (R-/S-MBA)$PbBr_3$ [218], although in this case the emission is redshifted compared to the racemic monohydrated phase which can be related to the differences in the octahedral connectivity of the $PbBr_6$ octahedra from corner-sharing type for (Rac-MBA)$_3PbBr_5 \cdot H_2O$ and edge-sharing case (R-/S-MBA)$PbBr_3$. This difference in connectivity can modify the orbital overlap of Pb–Br bonds and alter the conduction/valence bandwidths and effective masses, which in turn can affect how deeply an exciton could localized in a STE state. The emergence of STE luminescence in the racemic compound underscores the effect of dimensionality and molecular packing on emission dynamics. The dimensional transition from 2D to 1D with the use of racemic mixture as organic spacers enhances the EPC due to reduced dielectric screening and stronger quantum confinement. This effect is further reinforced by interstitial water molecules, which are stabilized between the inorganic chains in the 1D structure and interact dynamically with the organic cations via hydrogen bonding, further softening the lattice and facilitating STE formation.

Temperature-dependent PL measurements were performed to investigate the emission behavior of (Rac-MBA)$_3PbBr_5 \cdot H_2O$, as shown in Figure 30(a). The BE observed at room temperature blueshifted and rapidly increased its intensity upon cooling until 110 K and reached saturation around 80-100 K. Below 80 K, the BE redshifted and its intensity decreased followed by the emergence of a narrow-band emission (NE) centered at 410 nm with minor emissions around 350–375 nm that exhibited a relatively large Stokes shift compared to the excitonic peak at 350 nm, but it correlates closely with the absorption feature near 400 nm as shown in Figure 29(a), suggesting that it originates from bound exciton emission associated with mid-gap defect states. The BE profile resembled overlapping emission bands as temperature decreases. Although multiple-peak fitting was attempted, the uncertainty in the number of contributing peaks and their irregular shifts with temperature rendered the fitting results unreliable. As well resolve bands were not observed in the range of the NE emission, the overall analysis was performed by considering the entire spectral range of the BE (450–700 nm) and NE (350–450 nm) regions to evaluate the following results.

Figure 30 – (a) PL temperature-dependence of $(Rac\text{-}MBA)_3PbBr_5 \cdot H_2O$ perovskites. (b) Normalized integrated PL intensity and (c) FWHM of BE dependences on temperature

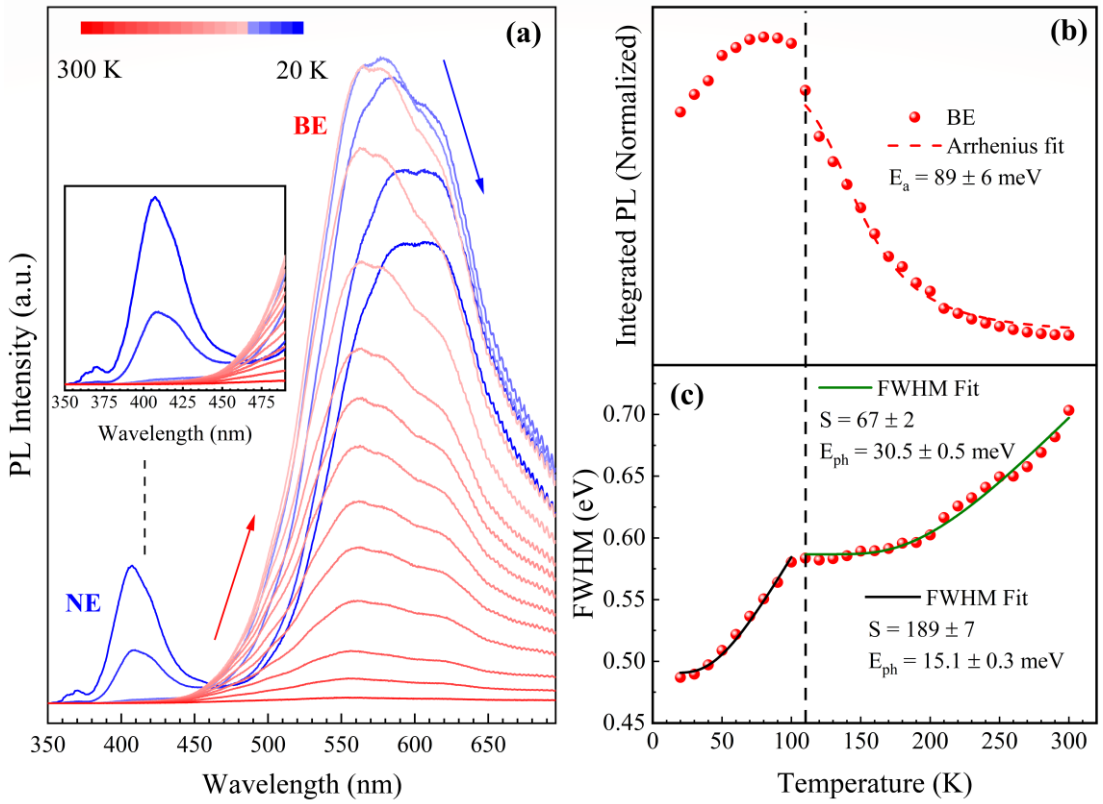

Source: elaborated by the author.

To estimate the activation energy E_a, the Arrhenius equation described in Equation (11) of Chapter 4 was applied to the integrated intensity of BE before saturation as shown in Figure 30(b). To estimate E_a for the NE, because of the weak intensities at temperatures close to 110 K, a linear fit of $\ln(I_0/I_{PL}(T) - 1)$ as a function of $(k_B T)^{-1}$ was performed as illustrated in Figure 31. The results yielded E_a = 89 ± 6 meV for the BE and E_a = 9.1 ± 0.2 meV for the NE. The activation energy for the BE could be related to the energy barrier for nonradiative recombination and was consistent with the presence of the broadband even at room temperature (thermal energy ≈ 25 meV). Since the emergence of the NE with increasing intensity occurred simultaneously with the reduction of the BE intensity, the low E_a value for the NE could be interpreted as the energy barrier for exciton trapping [82]. This interpretation is consistent with the appearance of the NE below 110 K (thermal energy ≈ 9.48 meV).

Figure 31 – Plot and linear fit of $\ln(I_0/I_{PL}(T) - 1)$ as a function of $(k_B T)^{-1}$ for the NE integrated PL intensity. On the vertical axis, $I = I_{PL}(T)$

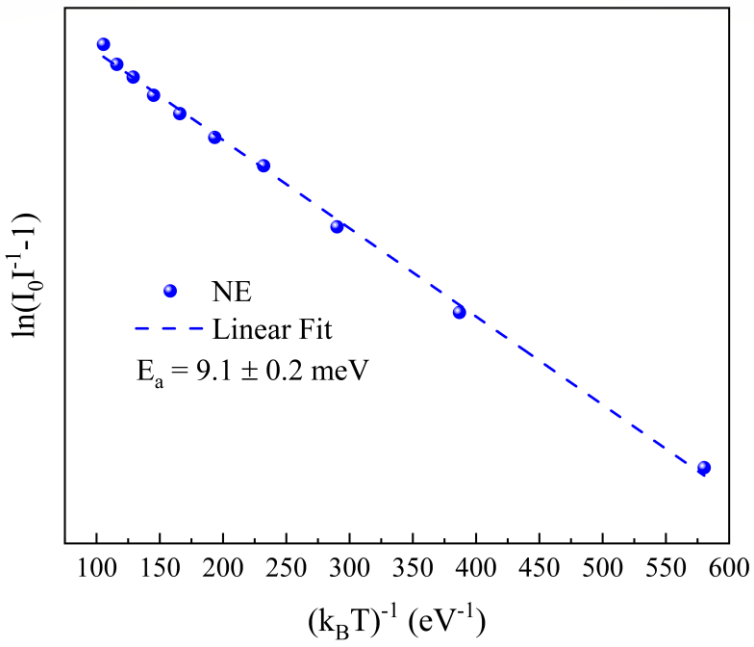

Source: elaborated by the author.

As before, the BE was attributed to STE emission, which are closely related to the interactions between charge carriers and lattice vibrations. To assess the strength of the EPC, the temperature dependence of the BE linewidth $FWHM(T)$ was analyzed, as shown in Figure 30(c). This dependence was modeled using the Equation (9) of Chapter 2 to extract the Huang–Rhys parameter S related to the EPC strength and the emitted phonons with energy $\hbar\omega$ following the radiative emission. Intriguingly, Figure 30(c) reveals two distinct regimes above and below 110 K. Shifting the zero-temperature to 110 K, to reflect thermally activated phonons, Equation (9) applied to the BE linewidth data above 110 K yielded E_{ph} = 30.5 ± 0.5 meV (~245 cm^{-1}) and S = 67 ± 2, which elucidated strong EPC usually found in STE emission. In contrast, the analysis below 110 K resulted in E_{ph} = 15.1 ± 0.3 meV (~122 cm^{-1}) and S = 189 ± 7. The phonon energies could be associated with those seen in the Raman spectrum at 143 cm^{-1} and 230 cm^{-1} as shown in Figure 32. Notably, the low-temperature Huang–Rhys factor of S = 189 ± 7 was almost three times higher than the high-temperature value and among the largest reported to date [48,91].

Figure 32 – Room-temperature Raman spectrum of $(Rac\text{-}MBA)_3PbBr_5{\cdot}H_2O$. The inset shows the range between 100 cm^{-1} to 250 cm^{-1} with the mode assignments from the results of EPC analysis

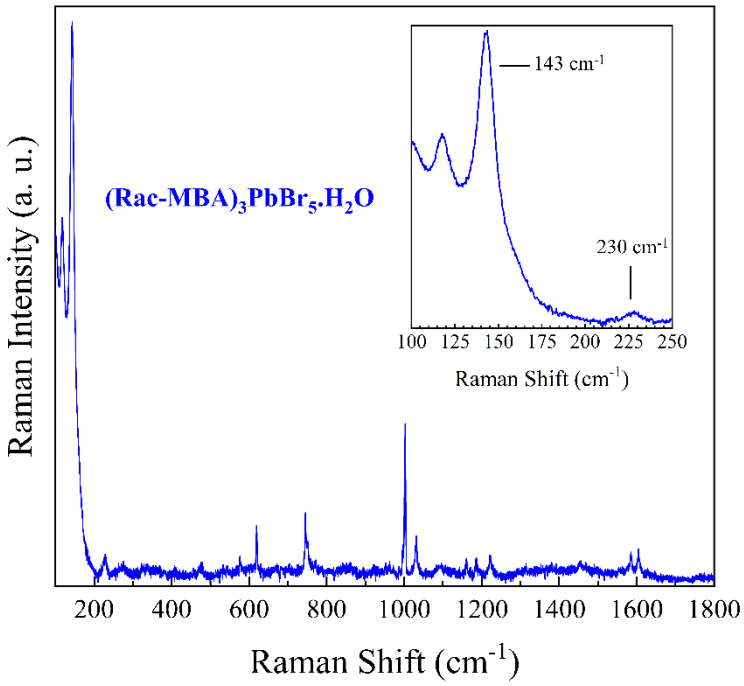

Source: elaborated by the author.

The two distinct behaviors of the $(Rac\text{-}MBA)_3PbBr_5{\cdot}H_2O$ linewidth presented in Figure 30(c) above and below 110 K could indicate that two STE states involved in the overall PL phenomena within the analyzed temperature range. The emergence and increase of the NE, accompanied by the decrease of BE as temperature lowers, is commonly associated with an energy barrier where excitons can thermally relax into STE states without modifying the internal dynamics of those states [82]. In principle, this should not influence the STE linewidth behavior if a single trapped state is assumed. Furthermore, an inspection of the BE shape before (red curves) and after (blue curves) 110 K reveals no clear correspondence between their overlapped peaks, further suggesting additional influences on the STE emissions involved in the PL behavior of $(Rac\text{-}MBA)_3PbBr_5{\cdot}H_2O$.

In order to correlate whether the changes observed in the PL were related to SPT, temperature-dependent PXRD measurements of $(Rac\text{-}MBA)_3PbBr_5{\cdot}H_2O$ powder were evaluated, as shown in Figure 33. Rietveld refinement of the diffractograms revealed a continuous decrease of the lattice parameters and unit cell volume from 380 K to 80 K while maintaining its monoclinic crystal structure, as illustrated in Figure 34(a,b). These results excluded the possibility of SPT at low temperatures that could modify the electronic structure

of (Rac-MBA)$_3$PbBr$_5$·H$_2$O and affect the PL behavior under 110 K as already discussed.

Figure 33 – Temperature-dependent PXRD diffractograms of (Rac-MBA)$_3$PbBr$_5$·H$_2$O

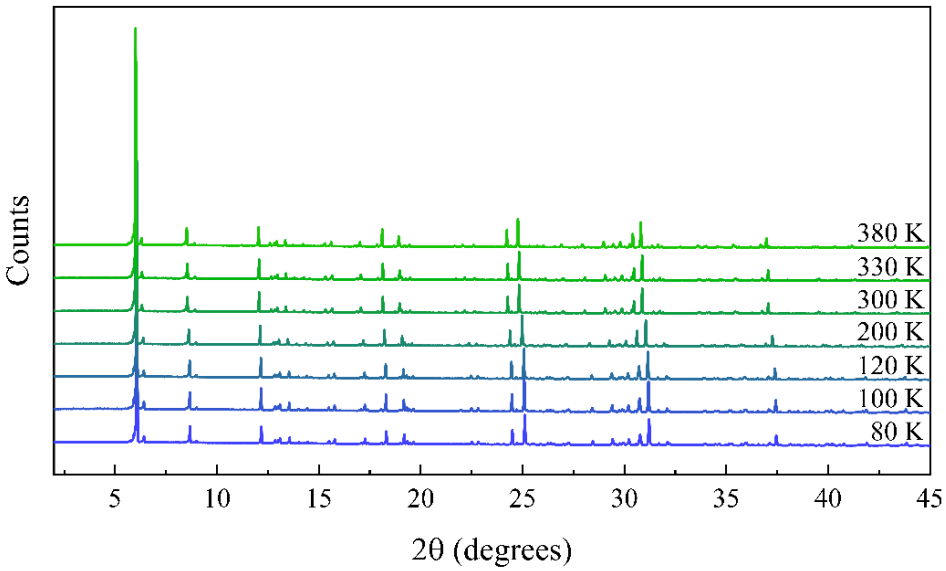

Source: elaborated by the author.

Figure 34 – Temperature dependence of the lattice parameters (a) *a*, *b*, *c*, and (b) *β* along with the unit cell volume of (Rac-MBA)$_3$PbBr$_5$·H$_2$O perovskite. (c) Behavior of octahedra distortions evaluated by the distortion index Δd and bond angle variance σ^2 with temperature

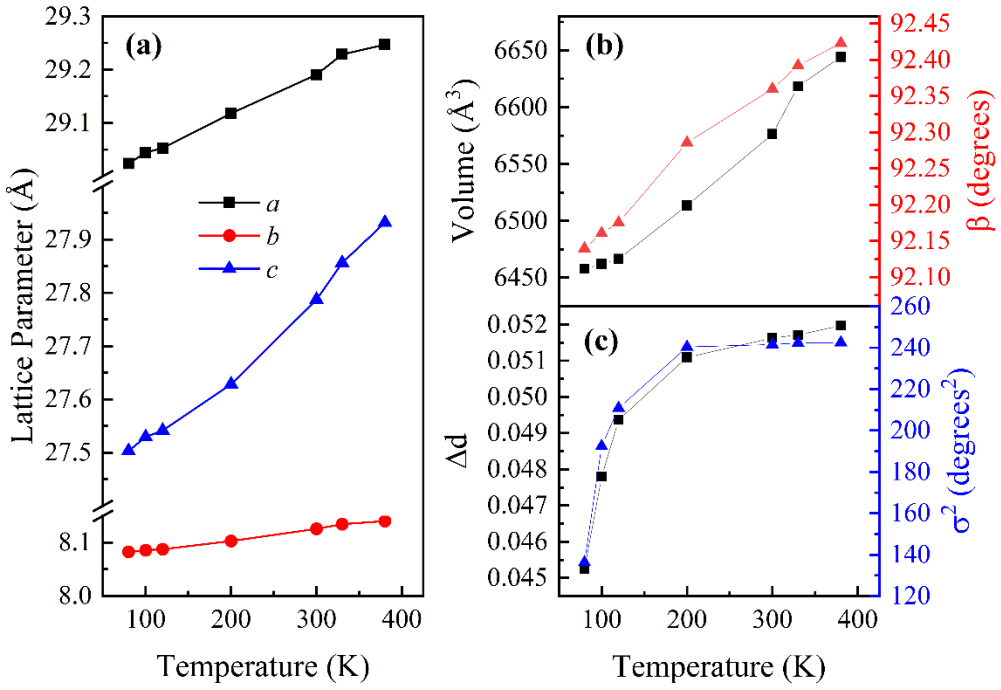

Source: elaborated by the author.

To get insights about the temperature behavior of the inorganic framework, as they are the most responsible for the optoelectronic properties of LDMHPs, the octahedra distortions were analyzed through the use of two parameters called distortion index Δd and bond angle variance σ^2 given by the following equations [235]:

$$\Delta \mathrm{d} = \sum_i \frac{|d_i - d|}{6d}, \tag{13}$$

$$\sigma^2 = \sum_i \frac{(\theta_i - 90°)^2}{11}, \tag{14}$$

where d_i is the i-th Pb-Br bond length in an octahedron, d is the average bond length, and θ_i represents the i-th Br-Pb-Br bond angle in an octahedron. As shown in Figure 34(c), the octahedra distortions slowly modified above 120 K, which indicated the persistence of the octahedra configuration. However, the opposite trend is observed in the range of 120 K to 80 K where octahedra distortions rapidly decreased with temperature, where the most significant decreased observed was for the σ^2 parameter from 242.48 degrees^2 at 380 K to 136.27 degrees^2 at 80 K. Octahedral distortions are known to contribute to the formation of STE in LDMHPs, where inorganic distorted environments favor exciton trapping [48,89,236]. However, lowering the temperature or applying pressure usually promotes exciton self-trapping by increasing octahedral distortions [237,238]. In contrast, (Rac-MBA)$_3$PbBr$_5$·H$_2$O possess an opposite behavior, where lowering temperature reduced octahedral distortions that play a central role in governing the PL behavior of the monohydrated 1D phase at low temperatures. Similar behavior has previously been observed in layered bromide perovskites under pressure [239]. Thus, it is proposed that the degree of octahedral distortion above 110 K is sufficient to allow STE states responsible for the BE emission. Below 110 K, however, these distortions are significantly reduced, meaning the high-temperature STE can no longer be stabilized. This makes way for the formation of different STE states with greater EPC strength upon interacting with lower-energy emitted phonons as higher-energy phonons are frozen out at low temperatures. Furthermore, both STE and detrapped states appear because the thermal energy barrier required to fully trap the excitons in the low-temperature STE states was approximately 110 K.

6 CONCLUSIONS

The primary aim of this thesis was to comprehensively investigate EPC in LDMHPs through a combination of diverse characterization techniques and theoretical approaches. The research explored EPC effects in multiphonon emission and STE luminescence of the VODP Cs_2SnBr_6. Additionally, it focused on the origin and characterization of the EPC mechanism regarding the low-temperature PL properties of 0D Rb_2SnBr_6. Furthermore, it explored the influence of chiral organic spacers, including both enantiomers and the racemic mixture, on lead bromide perovskites, which imparted a dimensional reduction from 2D (R-/S-MBA)$_2PbBr_4$ phases to a 1D monohydrated (Rac-MBA)$_3PbBr_5 \cdot H_2O$ structure, resulting in distinct regimes of STE emission and EPC under low-temperature conditions.

Through analysis of Raman spectroscopy and absorption and PL measurements, we observed the strong EPC and STE formation in the VODP Cs_2SnBr_6 belonging to the cubic $Fm\bar{3}m$ space group. At room temperature, excitation energies closer to the excitonic bandgap energy resulted in high-order multiphonon scattering, notably leading to intense $nA1_g$ overtones up to the fourth order mediated by strong EPC. The lattice distortions induced the formation of STE below the bandgap energy, which at room temperature display a direct-bandgap energy of 3.16 eV, with distinct excitonic absorption peaks at 3.73 eV and 4.29 eV. An intense red broadband emission centered at 660 nm with a large Stokes shift (830 meV) has also been observed. The Huang–Rhys factor S = 24.4 of the compound confirmed the high strength of EPC, with the contribution of the Raman-active $\nu_{as}(E_g)$ mode related to the Sn–Br asymmetric stretching predominating in the electronic transition, where the atomic motion in the octahedra due to this mode is similar to the distortion caused by a Jahn–Teller interaction, which is known to be one of the reasons responsible for emission broadening.

For the 0D Rb_2SnBr_6, SCXRD revealed a cubic symmetry in $Fm\bar{3}m$ space group with a direct energy bandgap E_g = 2.960 eV in the UV-Vis range obtained by DRS. Infrared and Raman spectroscopies showed the main vibrational modes associated with bending and stretching of $[SnBr_6]^{2-}$ octahedra, and low-temperature Raman analyses provided no evidence of any SPT down to 10 K. DFT results were very consistent with the vibrational and optical properties found at room temperature. Low-temperature PL spectrum indicated a broad emission with large Stokes shift energy consistent with excitonic self-trapping, as the power and temperature-dependent PL pointed out. The EPC was evaluated upon the PL linewidth broadening temperature dependence based on two perspectives where charge carries interplay with Br-Sn-Br asymmetric bending of LO phonons mediated by Fröhlich interactions were the

main mechanism responsible for the PL broadening through phonon-assisted radiative emission. Strong EPC was elucidated by the Huang–Rhys factor S = 34 coherent with STE emission commonly found in LDMHPs. The Fröhlich parameter α found through experimental data and theoretical calculations pointed out the main contributions of hole localization by large hole-polaron mass in STE formation.

Concerning the LDMHPs with chiral spacers, this work revealed the influence of the chiral organic molecules on the structural dimensionality, optoelectronic behavior, and EPC of low-dimensional lead bromide perovskites. Enantiopure MBA cations promoted the formation of ordered 2D Ruddlesden–Popper (R-/S-MBA)$_2$PbBr$_4$ perovskites with orthorhombic $P2_12_12_1$ space group, with narrow excitonic emission and evidence of chirality transfer from the chiral spacers to the inorganic framework from circular dichroism data. In contrast, the racemic MBA mixture induced packing frustrations that prevented layered ordering and favored the formation of a 1D monohydrated phase (Rac-MBA)$_3$PbBr$_5$·H$_2$O belonging to the monoclinic *C2/c* space group. This dimensional transition was accompanied by the emergence of broadband PL, attributed to the recombination of STE. Temperature-dependent PL studies revealed that this broadband emission arose from strong EPC comprised of two regimes above and below 110 K, with the emergence of a narrow emission below this threshold. The unusual modifications of the EPC on the PL properties were further analyzed based on structural origins, where the strong decrease in octahedra distortions, especially in the bond angle variance, was associated with changes in the octahedral environment that could lead to distinct STE emission behavior and the appearance of the narrow emission.

The works comprised in this thesis facilitate the understanding of how EPC impacts optoelectronic properties, particularly STE emergence and behavior, providing a comprehensive understanding of the interplay between lattice dynamics and electronic properties, offering insights into materials based on LDMHPs, and expanding the design space for next-generation optoelectronic devices.

7 PUBLICATIONS

7.1 Publications related to this thesis

1. **C. S. S. Soares,** J. S. Rodríguez-Hernández, M. A. P. Gómez, D. M. Andrade, P. B. A Fechine, A. P. Ayala, and C. W. A. Paschoal, Strong electron–phonon coupling in vacancy-ordered Cs_2SnBr_6 double perovskite, *J. Mater. Chem. C* **12**, 16758 (2024).
2. **C. S. S. Soares**, J. S. Rodríguez-Hernández, B. P. Silva, M. A. P. Gómez, V. S. Neto, A. P. Ayala, and C. W. A. Paschoal, Electron-phonon coupling mediated by Fröhlich interaction in perovskite Rb_2SnBr_6, *Phys. Rev. B* **112**, 235203 (2025).

3. **C. S. S. Soares**, C. M. Acosta, F. F. Ferreira, A. Tofanello, M. A. P. Gómez, A. P. Ayala, J. R. Toledo, Y. G. Gobato, M. A. Lemes, C. W. A. Paschoal, and J. A. Souza, Chirality-driven dimensionality and broadband emission in lead bromide perovskites, *Mater. Adv.* **6**, 9545 (2025).

7.2 Other publications

1. A. Nonato, J. S. Rodríguez-Hernández, D. S. Abreu, **C. C. S Soares**, M. A. P Gómez, A. García-Fernández, M. A. Señarís-Rodríguez, M. S. Andújar, A. P. Ayala, R. X. Silva, and C. W. A. Paschoal, Strong Electron–Phonon Coupling and Lattice Dynamics in One-Dimensional $[(CH_3)_2NH_2]PbI_3$ Hybrid Perovskite, Chem. Mater. **37**, 1013 (2025).

2. M. A. Lemes, **C. C. S Soares**, E. A. Morais, Y. J. Onofre, M. P. F. Godoy, C. W. A. Paschoal, J. J. S. Acuna, C. M. Acosta, and J. A. Souza, Unveiling Low-Energy Emission in 2D Organic–Inorganic Perovskites: A Photorecycling and Electron–Phonon Coupling Study, *ACS Phot.* **12**, 3815 (2025).

3. J. R. Franca, A. S. V., L. J. Q. Cuna**, C. C. S. Soares**, F. S. A. Abud, C. M. Acosta, C. C. P. Cid, and J. A. Souza, Tuning Crystalline Phase and Photoactivity through Charge and Temperature-Assisted Electrodeposition in Bi_2Se_3 Films, *ACS Appl. Electron. Mater.* (2026).

4. **C. S. S. Soares**, A. Tofanello, A. C. Handa, C. W. A. Paschoal, C. M. Acosta, and J. A. Souza, Chiral-deformation-induced polarons as design principle for white-light emission in 2D organic halide perovskites. *Phys. Rev. Mater.* **10**, 024608 (2026).

REFERENCES

[1] LIU, Y.; MA, Z.; ZHANG, J.; HE, Y.; DAI, J.; LI, X.; SHI, Z.; MANNA, L. Light-Emitting Diodes Based on Metal Halide Perovskite and Perovskite Related Nanocrystals, **Advanced Materials,** 37, 2025.

[2] XIONG, G.; LI, X.; GUO, H.; LI, M.; TSANG, S.; CHENG, Y. Recent Advances on Self-Powered Metal Halide Perovskite Photodetectors, **EcoEnergy**, 2026.

[3] XING, Z.; ZHOU, Y.; YANG, Z.; MA, C.; WU, D.; GAO, J.; CHEN, Y. From Nanoscale Science to Medical Imaging: Metal Halide Perovskites for Low-Dose Direct X-Ray Detection, **ACS Nano,** 20, 1775, 2026.

[4] SHIN, S. S.; PARK, B.; NOH, J. H.; SEOK, S. I. Interlayer engineering in metal halide perovskite photovoltaics, **Nat. Photonics,** 20, 11, 2026.

[5] ZHANG, X.; CAO, Z.; GONG, X. Device Architecture for Perovskite Photovoltaics, ACS Appl. **Mater. Interfaces**, 18, 4135 (2026).

[6] JUHI, J.; SASKI, M.; KOCHANIEC, M. K.; WIECZOREK, W.; DOMINKO, R.; LEWIŃSKI, J. Exploring metal halide perovskites as active architectures in energy storage systems, **J. Mater. Chem. A Mater.**, 13, 38753, 2025.

[7] SETHI, N. M.; PATRA, A.; KARAN, N. S.; PRADHAN, N. Excited-State Dynamics in Lead Halide Perovskite Nanocrystals: Effects of Size, Shape, Doping, and Surface Modifications, **Small**, 2026.

[8] GHASEMI, M.; LU, J.; LIA, B.; WEN, X.; Steady state and transient absorption spectroscopy in metal halide perovskites, **Chem. Soc. Rev.**, 54, 1644, 2025.

[9] AKKERMAN, Q. A.; MANNA, L.; What Defines a Halide Perovskite?, **ACS Energy Lett.**, 5, 604, 2020.

[10] KATZ, E. A. Perovskite: Name Puzzle and German-Russian Odyssey of Discovery, **Helv. Chim. Acta**, 103, 2020.

[11] SOLTANI, S.; HJIRI, M.; AHMED, N. I. A.; JBELI, A.; ALDUKHAVEL, A. M.; ALTHUMAIRI, N. A. Metal halide perovskites for energy applications: recent advances, challenges, and future perspectives, **RSC Adv.**, 15, 21811, 2025.

[12] WANG, Y.; WANG, Y.; DOHERTY, T. A. S.; STRANKS, S. D.; GAO, F.; YANG, D. Octahedral units in halide perovskites, **Nat. Rev. Chem.**, 9, 261, 2025.

[13] FEDOROVSKIY, A. E.; DRIGO, N. A.; NAZEERUDDIN, M. K. The Role of Goldschmidt's Tolerance Factor in the Formation of A_2BX_6 Double Halide Perovskites and its Optimal Range, **Small Methods**, 4, 2020.

[14] BARTEL, C. J.; SUTTON, C.; GOLDSMITH, B. R.; OUYANG, R.; MUSGRAVE, C. B.; GHIRINGHELI, L. M.; SCHEFFLER, M. New tolerance factor to predict the

stability of perovskite oxides and halides, **Sci. Adv.**, 5, 2019.

[15] KIESLICH, G.; SUN, S.; CHEETHAM, A. K. An extended Tolerance Factor approach for organic–inorganic perovskites, **Chem. Sci.**, 6, 3430, 2015.

[16] PROTESESCU, L.; YAKUNIN, S.; BODNARCHUCK, M. I.; KRIEG, F.; CAPUTO, R.; HENDON, C. H.; YANG, R. X.; WALSH, A.; KOVALENKO, M. V. Nanocrystals of Cesium Lead Halide Perovskites ($CsPbX_3$, X = Cl, Br, and I): Novel Optoelectronic Materials Showing Bright Emission with Wide Color Gamut, **Nano Lett.**, 15, 3692, 2015.

[17] STEELE, J. A.; LAI, M.; ZHANG, Y.; LIN, Z.; HOFKENS, J.; ROEFFAERS, M. B. J.; YANG, P. Phase Transitions and Anion Exchange in All-Inorganic Halide Perovskites, **Acc. Mater. Res.**, 1, 3, 2020.

[18] HOLLEY III, R.; BURLINGAME, Q. C.; LOO, Y.-L. Mapping the polymorphic phase transformations of $CsPbI_3$ perovskite thin films, **J. Mater. Chem. C Mater.**, 13, 19654, 2025.

[19] JIN, H.; ZEN, Y.-J.; STEELE, J. A.; ROEFFAERS, M. B. J.; HOFKENS, J.; DEBROYE, E. Phase stabilization of cesium lead iodide perovskites for use in efficient optoelectronic devices, **NPG Asia Mater.**, 16, 24, 2024.

[20] TIPPARAK, P. et al. The Impact of $MAPbI_3$ Quantum Dots on CsFA Perovskite Solar Cells: Interface and Hole Extraction Improvement, **ACS Appl. Energy Mater.**, 8, 355, 2025.

[21] WU, J. et al. Approaching 26% Efficiency in Inverted $FAPbI_3$ Perovskite Solar Cells Enabled by Tailored Fluoropyridine Derivative Additives, **Adv. Funct. Mater.**, 2026.

[22] NOMAN, M.; KHAN, Z.; JAN, S. T. A comprehensive review on the advancements and challenges in perovskite solar cell technology, **RSC Adv.**, 14, 5085, 2024.

[23] DENG, W.; WEI, J.; MA, Z.; FENG, W. Research Progress on Stability of $FAPbI_3$ Perovskite Solar Cells, **Crystal Research and Technology**, 60, 2025.

[24] SUN, K.; MÜLLER-BUSCHBAUM, P. Shedding Light on the Moisture Stability of Halide Perovskite Thin Films, **Energy Technology**, 11, 2023.

[25] AFTAB, A.; MURSHED, R. Recent progress in electron transport layers for enhancing the performance of tin-based perovskite solar cells, **Solar Energy**, 300, 113866, 2025.

[26] ZHANG, B.; ZENG, Z.; DON, H.; GAO, W.; RAN, C. Recent advances in tin halide perovskite solar cells: a critical review, **J. Mater. Chem. A Mater.**, 13, 30708, 2025.

[27] LIANG, C.; MZHANG, M.; YANG, Z.; TIAN, J. Advancements in Metal Halide Perovskites and their Derivatives for Direct-Type X-Ray Detectors, **Small**, 21, 2025.

[28] CARDENAS-MORCOSO, D.; GUALDRÓN-REYES, A. F.; VITORETI, A. B. F.; GARCÍA-TECEDOR, M.; YOON, S. J.; FUENTE, M. S.; MORA-SERÓ, I.;

GIMENEZ, S. Photocatalytic and Photoelectrochemical Degradation of Organic Compounds with All-Inorganic Metal Halide Perovskite Quantum Dots, **J. Phys. Chem. Lett.**, 10, 630, 2019.

[29] LI, Q.; WU, K.; ZHU, H.; YANG, Y.; HE, S.; LIAN, T. Charge Transfer from Quantum-Confined 0D, 1D, and 2D Nanocrystals, **Chem. Rev.**, 124, 5695, 2024.

[30] KAMBHAMPATI, P. Nanoparticles, Nanocrystals, and Quantum Dots: What are the Implications of Size in Colloidal Nanoscale Materials?, **J. Phys. Chem. Lett.**, 12, 4769, 2021.

[31] YE, J.; GAUR, D.; MI, C.; ZHEN, Z.; FERNÁNDEZ, I. L.; ZHAO, H.; DONG, Y.; POLAVARAPU, L.; HOYE, R. L. Z. Strongly-confined colloidal lead-halide perovskite quantum dots: from synthesis to applications, **Chem. Soc. Rev.**, 53, 8095, 2024.

[32] ZHOU, Y.; CHEN, J.; BAKR, O. M.; MOHAMMED, O. F. Metal Halide Perovskites for X-ray Imaging Scintillators and Detectors, **ACS Energy Lett.**, 6, 739, 2021.

[33] CHEN, Y.; FENG, Z.; PAL, A.; ZHANG, J. Recent Progress on the Performance of Lead-Based Halide Perovskite $APbX_3$ Detectors, **Physica Status Solidi a**, 219, 2022.

[34] LOZANO, G. The Role of Metal Halide Perovskites in Next-Generation Lighting Devices, J. Phys. **Chem. Lett.**, 9, 3987, 2018.

[35] VANORMAN, Z. A. et al. Metal Doping of Strongly Confined Halide Perovskite Nanocrystals under Ambient Conditions, **J. Am. Chem. Soc.**, 147, 16536, 2025.

[36] LIU, M.; ZHOU, J.; HAO, X.; LIU, H.; WANG, S.; LI, X. Mn^{2+}-doping enables improved crystallization of $CsPbI_3$ quantum dots for efficient deep-red light-emitting diodes, **J. Mater. Chem. C Mater.**, 12, 11174, 2024.

[37] BHANDARI, S.; PRAMANIK, S.; MANNA, M.; SINGHA, S.; AKHTAR, F. Surface modification unleashes light emitting applications of $APbX_3$ perovskite nanocrystals, **Chemical Communications**, 61, 817, 2025.

[38] LIU, G.; GHASEMI, M.; WEI, Q.; JIA, B.; YANG, Y.; WEN, X. Dynamic Defect Tolerance in Metal Halide Perovskites: From Phenomena to Mechanism, **Adv. Energy Mater.**, 15, 2025.

[39] MIAH, M. H.; RAHMAN, M. B.; NUR-E-ALAM, M.; ISLAM, M. A.; SHAHINUZZAMAN, M.; RAHMAN, M. R.; ULLAH, M. H.; KHANDAKER, M. U. Key degradation mechanisms of perovskite solar cells and strategies for enhanced stability: issues and prospects, **RSC Adv.**, 15, 628, 2025.

[40] DU, F.; LIU, X.; LIAO, J.; YU, D.; ZHANG, N.; CHEN, Y.; LIANG, C.; YANG, S.; FANG, G. Improving the Stability of Halide Perovskites for Photo-, Electro-, Photoelectro-Chemical Applications, **Adv. Funct. Mater.**, 34, 2024.

[41] ALI, A.; CRUGUEL, H.; GIANGRISOSTOMI, E.; OVSYANNIKOV, R.; SILLY, M.

G.; DUDY, L.; CAPPEL, U. B.; LHUILLIER, E.; WITKOWSKI, N.; JOHANSSON, F. O. L. The Electronic Impact of Light-Induced Degradation in $CsPbBr_3$ Perovskite Nanocrystals at Gold Interfaces, **J. Phys. Chem. Lett.**, 15, 3721, 2024.

[42] PAN, Q.; QZHAO, Q.; WEI, P.; LI, G. Surface Ligands for Perovskite Quantum Dots, **ChemSusChem**, 18, 2025.

[43] GHORAI, A.; MIDYA, A.; RAY, S. K. Surfactant-Induced Anion Exchange and Morphological Evolution for Composition-Controlled Caesium Lead Halide Perovskites with Tunable Optical Properties, **ACS Omega**, 4, 12948, 2019.

[44] RAFIQUE, H.; ABBAS, G.; MENDES, M. J.; BARQUINHA, P.; MARTINS, R.; FORTUNATO, E.; ÁGUAS, H.; JANA, S. Recent Advancements and Perspectives of Low-Dimensional Halide Perovskites for Visual Perception and Optoelectronic Applications, **Nanomicro Lett.**, 18, 44, 2026.

[45] YUSOFF, A. R. M.; NAZEERUDDIN, M. K. Low-Dimensional Perovskites: From Synthesis to Stability in Perovskite Solar Cells, **Adv. Energy Mater.**, 8, 2018.

[46] WANG, S.; ZHU, H.; SHENG, M.; SHAO, B.; HE, Y.; LIU, Z.; ZHOU, G. Advances of Low-Dimensional Organic-Inorganic Hybrid Metal Halide Luminescent Materials: A Review, **Crystals Basel.**, 15, 364, 2025.

[47] PENG, X.; LAI, Z.; SHAO, H.; SHEN, Y.; MENG, Y.; HO, J. C. Halide Perovskite Nanostructures: Processing Methods and Optoelectronics Applications, **Npj Nanophotonics**, 2, 42, 2025.

[48] HAN, Y.; CHENG, X.; CUI, B.-B. Factors influencing self-trapped exciton emission of low-dimensional metal halides, **Mater. Adv.**, 4, 355, 2023.

[49] MERCIER, N. Hybrid Halide Perovskites: Discussions on Terminology and Materials, **Angew. Chem. Int. Ed.**, 58, 17912, 2019.

[50] HONG, K.; LE, Q. V.; KIM, S. Y.; JANG, H. W. Low-dimensional halide perovskites: review and issues, **J. Mater. Chem. C Mater.**, 6, 2189, 2018.

[51] KATAN, C.; MERCIER, N. EVEN, J. Quantum and Dielectric Confinement Effects in Lower-Dimensional Hybrid Perovskite Semiconductors, **Chem. Rev.**, 119, 3140, 2019.

[52] ZHANG, H. et al. Ultrafast relaxation of lattice distortion in two-dimensional perovskites, **Nat. Phys.**, 19, 545, 2023.

[53] LIN, H.; ZHOU, C.; TIAN, Y.; SIEGRIST, T.; MA, B. Low-Dimensional Organometal Halide Perovskites, **ACS Energy Lett.**, 3, 54, 2018.

[54] XU, Z.; JIANG, X.; CAI, H.; CHEN, K.; YAO, X.; FENG, Y. Toward a General Understanding of Exciton Self-Trapping in Metal Halide Perovskites, **J. Phys. Chem. Lett.**, 12, 10472, 2021.

[55] CORTECCHIA, D.; YIN, J.; PETROZZA, A.; SOCI, C. White light emission in low-

dimensional perovskites, J. Mater. Chem. C Mater. **7**, 4956 (2019).

[56] YAMADA, Y.; KANEMITSU, Y. Electron-phonon interactions in halide perovskites, **NPG Asia Mater.**, 14, 48, 2022.

[57] PENG, H.; ZOU, B. Effects of Electron–Phonon Coupling and Spin–Spin Coupling on the Photoluminescence of Low-Dimensional Metal Halides, **J. Phys. Chem. Lett.**, 13, 1752, 2022.

[58] RAVALI, V.; GHOSH, T. Electron–phonon coupling in two-dimensional Ruddlesden–Popper hybrid perovskites, **Chemical Communications**, 61, 10898, 2025.

[59] FRANCHINI, C.; RETICCIOLI, M.; SETVIN, M.; DIEBOLD, U. Polarons in materials, **Nat. Rev. Mater.**, 6, 560, 2021.

[60] GHOSH, D.; WELCH, E.; NEUKIRCH, A. J.; ZAKHIDOV, A.; TRETIAK, S. Polarons in Halide Perovskites: A Perspective, **J. Phys. Chem. Lett.**, 11, 3271, 2020.

[61] BUIZZA, L. R. V.; HERZ, L. M. Polarons and Charge Localization in Metal-Halide Semiconductors for Photovoltaic and Light-Emitting Devices, **Advanced Materials**, 33, 2021.

[62] SMITH, M. D.; KARUNADASA, H. I. White-Light Emission from Layered Halide Perovskites, **Acc. Chem. Res.**, 51, 619, 2018.

[63] HERBERT, F. Theory of electrical breakdown in ionic crystals, **Proc. R. Soc. Lond. A Math. Phys. Sci.**, 160, 230, 1937.

[64] PELANT, I.; VALENTA, J. Luminescence Spectroscopy of Semiconductors, **Oxford University PressOxford**, 2012.

[65] CHEN, B.; CHEN, R.; HUANG, B. Strong Electron–Phonon Coupling Induced Self-Trapped Excitons in Double Halide Perovskites, **Advanced Energy and Sustainability Research**, 4, 2023.

[66] TOYOZAWA, Y. Optical Processes in Solids, **Cambridge University Press**, 2003.

[67] RONA, M.; AYASLI, S. Acoustic deformation-potential polaron, **Phys. Rev. B**, 15, 4822, 1977.

[68] BARDEEN, J.; SHOCKLEY, W. Deformation Potentials and Mobilities in Non-Polar Crystals, **Physical Review**, 80, 72, 1950.

[69] HUANG, Y. et al. Giant deformation potential induced small polaron effect in Dion–Jacobson two-dimensional lead halide perovskites, **Natl. Sci. Rev.**, 12, 2025.

[70] SIMBULA, A. et al. Exciton dissociation in 2D layered metal-halide perovskites, **Nat. Commun.**, 14, 4125, 2023.

[71] TAO, W.; ZHOU, Q.; ZHU, H. Dynamic polaronic screening for anomalous exciton

spin relaxation in two-dimensional lead halide perovskites, **Sci. Adv.**, 6, 2020.

[72] GAMMON, D.; RUDIN, S.; REINECKE, T. L.; KATZER, D. S.; KYONO, C. S. Phonon broadening of excitons in GaAs/$Al_xGa_{1-x}As$ quantum wells, **Phys. Rev. B**, 51, 16785, 1995.

[73] CHEN, Y.; KOTHIYAL, G. P.; SINGH, J.; BHATTACHARYA, P. K. Absorption and photoluminescence studies of the temperature dependence of exciton life time in lattice-matched and strained quantum well systems, **Superlattices Microstruct.**, 3, 657, 1987.

[74] WRIGHT, A. D.; VERDI, C.; MILOT, R. L.; EPERON, G. E.; PÉREZ-OSORIO, M. A.; SNAITH, H. J.; GIUSTINO, F.; JOHNSTON, M. B.; HERZ, L. M. Electron–phonon coupling in hybrid lead halide perovskites, **Nat. Commun.**, 7, 11755, 2016.

[75] RUDIN, S.; REINECKE, T. L.; SEGALL, B. Temperature-dependent exciton linewidths in semiconductors, **Phys. Rev. B**, 42, 11218, 1990.

[76] LEI, H. et al. Persistent Exciton Dressed by Weak Polaronic Effect in Rigid and Harmonic Lattice Dion–Jacobson 2D Perovskites, **ACS Nano**, 18, 31485, 2024.

[77] BAEK, S.; YANG, S. J.; YANG, H.; SHAO, W.; YANG, Y.; DOU, L. Exciton Dynamics in Layered Halide Perovskite Light-Emitting Diodes, **Advanced Materials**, 2024.

[78] LI, S.; LUO, J.; LIU, J.; TANG, J. Self-Trapped Excitons in All-Inorganic Halide Perovskites: Fundamentals, Status, and Potential Applications, **J. Phys. Chem. Lett.**, 10, 1999, 2019.

[79] YIN, J.; NAPHADE, R.; ARZALUZ, L. G.; BRÉDAS, J.-L.; BAKR, O. M.; MOHAMMED, O. F. Modulation of Broadband Emissions in Two-Dimensional ⟨100⟩-Oriented Ruddlesden–Popper Hybrid Perovskites, **ACS Energy Lett.**, 5, 2149, 2020.

[80] CHEN, L.; SHEN, X.; WEI, Q.; CAO, J.; ZOU, B. Sb^{3+}-Doping Induced Self-Trapped Excitons and Ultrafast Carrier Dynamics in 0D Hybrid Indium Halides, **Adv. Opt. Mater.**, 13, 2025.

[81] KAHMANN, S.; TEKELENBURG, E. K.; DUIM, H.; KAMMINGA, M. E.; LOI, M. A. Extrinsic nature of the broad photoluminescence in lead iodide-based Ruddlesden–Popper perovskites, **Nat. Commun.**, 11, 2344, 2020.

[82] SMITH, M. D.; JAFFE, A.; DOHNER, E. R.; LINDENBERG, A. M.; KARUNADASA, H. I. Structural origins of broadband emission from layered Pb–Br hybrid perovskites, **Chem. Sci.**, 8, 4497, 2017.

[83] XU, B.; LI, Y.; HONG, P.; ZHANG, P.; HAN, J.; XIAO, Z.; QUAN, Z. Pressure-controlled free exciton and self-trapped exciton emission in quasi-one-dimensional hybrid lead bromides, **Nat. Commun.**, 15, 7403, 2024.

[84] ZHOU, L.; LIAO, J.; KUANG, D. An Overview for Zero-Dimensional Broadband

Emissive Metal-Halide Single Crystals, **Adv. Opt. Mater.**, 9, 2021.

[85] MORANA, M.; KAISER, W.; CHIARA, R.; ALBINI, B.; MEGGIOLARO, D.; MOSCONI, E.; GALINETTO, P.; DE ANGELIS, F.; MALAVASI, L. Origin of Broad Emission Induced by Rigid Aromatic Ditopic Cations in Low-Dimensional Metal Halide Perovskites, **J. Phys. Chem. Lett.**, 14, 7860, 2023.

[86] JIANG, F.; WU, Z.; LU, M.; GAO, Y.; LI, X.; BAI, X.; JI, Y.; ZHANG, Y. Broadband Emission Origin in Metal Halide Perovskites: Are Self-Trapped Excitons or Ions?, **Advanced Materials**, 35, 2023.

[87] DE JONG, M.; SEIJO, L.; MEIJERINK, A.; RABOUW, F. T. Resolving the ambiguity in the relation between Stokes shift and Huang–Rhys parameter, **Physical Chemistry Chemical Physics**, 17, 16959, 2015.

[88] TOYOZAWA, Y. Theory of Line-Shapes of the Exciton Absorption Bands, **Progress of Theoretical Physics**, 20, 53, 1958.

[89] WANG, X.; MENG, W.; LIAO, W.; WANG, J.; XIONG, R.-G.; YAN, Y. Atomistic Mechanism of Broadband Emission in Metal Halide Perovskites, **J. Phys. Chem. Lett.**, 10, 501, 2019.

[90] MCCALL, K. M.; STOUMPOS, C. C.; KOSTINA, S. S.; KANATZIDIS, M. G.; WESSELS, B. W. Strong Electron–Phonon Coupling and Self-Trapped Excitons in the Defect Halide Perovskites $A_3M_2I_9$ (A = Cs, Rb; M = Bi, Sb), **Chemistry of Materials**, 29, 4129, 2017.

[91] HAN, Y. et al. Exciton Self-Trapping for White Emission in 100-Oriented Two-Dimensional Perovskites via Halogen Substitution, **ACS Energy Lett.**, 7, 453, 2022.

[92] LUO, H. et al. Regulating Exciton–Phonon Coupling to Achieve a Near-Unity Photoluminescence Quantum Yield in One-Dimensional Hybrid Metal Halides, **Advanced Science**, 8, 2021.

[93] SPEK, A. L. Single-crystal structure validation with the program *PLATON*, **J. Appl. Crystallogr.**, 36, 7, 2003.

[94] KRAUSE, L.; HERBST-IRMER, R.; SHELDRICK, G. M.; STALKE, D. Comparison of silver and molybdenum microfocus X-ray sources for single-crystal structure determination, **J. Appl. Crystallogr.**, 48, 3, 2015.

[95] SHELDRICK, G. M. SHELXT – Integrated space-group and crystal-structure determination, Acta Crystallogr. **A Found. Adv.**, 71, 3, 2015.

[96] SHELDRICK, G. M. Crystal structure refinement with *SHELXL*, **Acta Crystallogr. C Struct. Chem.**, 71, 3, 2015.

[97] DOLOMANOV, O. V.; BOURHIS, L. J.; GILDEA, R. J.; HOWARD, J. A. K.; PUSCHMANN, H. OLEX2 : a complete structure solution, refinement and analysis program, **J. Appl. Crystallogr.**, 42, 339, 2009.

[98] MOMMA, K.; IZUMI, F. *VESTA 3* for three-dimensional visualization of crystal, volumetric and morphology data, **J. Appl. Crystallogr.**, 44, 1272 , 2011.

[99] COELHO, A. A. TOPAS and TOPAS-Academic : an optimization program integrating computer algebra and crystallographic objects written in C++, **J. Appl. Crystallogr.**, 51, 210, 2018.

[100] WOJDYR, M. Fityk : a general-purpose peak fitting program, **J. Appl. Crystallogr.**, 43, 1126, 2010.

[101] MURPHY, A. B. Modified Kubelka–Munk model for calculation of the reflectance of coatings with optically-rough surfaces, **J. Phys. D Appl. Phys.**, 39, 3571, 2006.

[102] CLARK, S. J.; SEGALL, M. D.; PICKARD, C. J.; HASNIP, P. J.; PROBERT, M. I. J.; REFSON, K.; PAYNE, M. C. First principles methods using CASTEP, Z. **Kristallogr. Cryst. Mater.**, 220, 567, 2005.

[103] KOHN, W.; SHAM, L. J. Self-Consistent Equations Including Exchange and Correlation Effects, **Physical Review**, 140, A1133, 1965.

[104] PERDEW, J. P.; BURKE, K.; ERNZERHOF, M. Generalized Gradient Approximation Made Simple, **Phys. Rev. Lett.**, 77, 3865, 1996.

[105] TKATCHENKO, A.; SCHEFFLER, M. Accurate Molecular Van Der Waals Interactions from Ground-State Electron Density and Free-Atom Reference Data, **Phys. Rev. Lett.**, 102, 073005, 2009.

[106] KAVANAGH, S. R.; SAVORY, C. N.; LIGA, S. M.; KONSTANTATOS, G.; WALSH, A.; SCANLON, D. O. Frenkel Excitons in Vacancy-Ordered Titanium Halide Perovskites (Cs_2TiX_6), **J. Phys. Chem. Lett.**, 13, 10965, 2022.

[107] MONKHORST, H. J.; PACK, J. D. Special points for Brillouin-zone integrations, **Phys. Rev. B**, 13, 5188, 1976.

[108] PFROMMER, B. G.; CÔTÉ, M.; LOUIE, S. G.; COHEN, M. L. Relaxation of Crystals with the Quasi-Newton Method, **J. Comput. Phys.**, 131, 233, 1997.

[109] HAMANN, D. R.; SCHLÜTER, M.; CHIANG, C. Norm-Conserving Pseudopotentials, **Phys. Rev. Lett.**, 43, 1494, 1979.

[110] BARONI, S.; DE GIRONCOLI, S.; CORSO, A. D.; GIANNOZZI, P. Phonons and related crystal properties from density-functional perturbation theory, **Rev. Mod. Phys.**, 73, 515, 2001.

[111] PERDEW, J. P. et al. Understanding band gaps of solids in generalized Kohn–Sham theory, **Proceedings of the National Academy of Sciences**, 114, 2801, 2017.

[112] IZMAYLOV, A. F.; SCUSERIA, G. E.; FRISCH, M. J. Efficient evaluation of short-range Hartree-Fock exchange in large molecules and periodic systems, **J. Chem.**

Phys., 125, 2006.

[113] HEYD, J.; SCUSERIA, G. E. Assessment and validation of a screened Coulomb hybrid density functional, **J. Chem. Phys.**, 120, 7274, 2004.

[114] HEYD, J.; PERALTA, J. E.; SCUSERIA, G. E.; MARTIN, R. L. Energy band gaps and lattice parameters evaluated with the Heyd-Scuseria-Ernzerhof screened hybrid functional, **J. Chem. Phys.**, 123, 2005.

[115] GIBBS, Z. M.; RICCI, F.; LI, G.; ZHU, H.; PERSSON, K.; CEDER, G.; HAUTIER, G.; JAIN, A.; SNYDER, G. J. Effective mass and Fermi surface complexity factor from ab initio band structure calculations, **NPJ Comput. Mater.**, 3, 8, 2017.

[116] YETTAPU, G. R.; TALUKDAR, D.; SARKAR, S.; SWARNKAR, A.; NAG, A.; GHOSH, P.; MANDAL, P. Terahertz Conductivity within Colloidal $CsPbBr_3$ Perovskite Nanocrystals: Remarkably High Carrier Mobilities and Large Diffusion Lengths, **Nano Lett.**, 16, 4838, 2016.

[117] PERDEW, J. P.; BURKE, K.; ERNZERHOF, M. Generalized Gradient Approximation Made Simple, **Phys. Rev. Lett.**, 77, 3865, 1996.

[118] KRESSE, G.; FURTHMÜLLER, J. Efficient iterative schemes for *ab initio* total-energy calculations using a plane-wave basis set, **Phys. Rev. B**, 54, 11169, 1996.

[119] KRESSE, G.; JOUBERT, D. From ultrasoft pseudopotentials to the projector augmented-wave method, **Phys. Rev. B**, 59, 1758, 1999.

[120] SUN, S.; LU, M.; GAO, X.; SHI, Z.; BAI, X.; YU, W. W.; ZHANG, Y. 0D Perovskites: Unique Properties, Synthesis, and Their Applications, **Advanced Science**, 8, 2021.

[121] CHEN, Q.; WANG, C.; WANG, K.; SU, Y.; DONG, G.; YAN, H. Zero-dimensional lead-free halide perovskites: from structural design to optoelectronic applications, **J. Mater. Chem. A Mater.**, 2026.

[122] MA, Y.; SUN, Y.; XU, W.; LIU, X.; ZHONG, Q.; SONG, Y.; FU, H.; YUE, C.; LEI, X. Ultrastable 0D Organic Zinc Halides with Highly Efficient Blue Light Emissions, **Adv. Opt. Mater.**, 10, 2022.

[123] ZHANG, R.; MAO, X.; YANG, Y.; YANG, S.; ZHAO, W.; WUMAIER, T.; WEI, D.; DENG, W.; HAN, K. Air-Stable, Lead-Free Zero-Dimensional Mixed Bismuth-Antimony Perovskite Single Crystals with Ultra-broadband Emission, **Angew. Chem. Int. Ed.**, 58, 2725, 2019.

[124] ZHANG, F.; ZHAO, Z.; CHEN, B.; ZHENG, H.; HUANG, L.; LIU, Y.; WANG, Y.; ROGACH, A. L. Strongly Emissive Lead-Free 0D $Cs_3Cu_2I_5$ Perovskites Synthesized by a Room Temperature Solvent Evaporation Crystallization for Down-Conversion Light-Emitting Devices and Fluorescent Inks, **Adv. Opt. Mater.**, 8, 2020.

[125] CHEN, R.; WANG, S.; LIN, F.; ZHENG, Y.; ZHANG, W.; WANG, J.; GUO, F. Stable Broadband Bright Green Emission of Self-trapped Excitons Triggered by Sb^{3+} Doping

in Zero-Dimensional Cs_3BiCl_6, **Eur. J. Inorg. Chem.**, 27, 2024.

[126] TENG, Q.; TAN, Q.; HOU, M.; ZHANG, J.; YUAN, F. Bright and Stable Zero-Dimensional Hexagonal Organic–Inorganic Tin Iodide Perovskites for High Color Rendering Index White Light-Emitting Diodes, **ACS Energy Lett.**, 10, 3691, 2025.

[127] LI, B.; WANG, Y.; XU, Y.; XIA, Z. Emerging 0D Hybrid Metal Halide Luminescent Glasses, **Advanced Materials**, 37, 2025.

[128] YIN, J.; BRÉDAS, J.-L.; BAKR, O. M.; MOHAMMED, O. F. Boosting Self-Trapped Emissions in Zero-Dimensional Perovskite Heterostructures, **Chemistry of Materials**, 32, 5036, 2020.

[129] NIE, J.; YUN, X.; CHENG, F.; LAN, B.; CAO, R.; WANG, J. Near-unity photoluminescence quantum yield in zero-dimensional lead-free indium-based hybrid perovskites by antimony doping, **J. Mater. Chem. C Mater.**, 12, 2571, 2024.

[130] LIAN, L. et al. Photophysics in $Cs_3Cu_2X_5$ (X = Cl, Br, or I): Highly Luminescent Self-Trapped Excitons from Local Structure Symmetrization, **Chemistry of Materials**, 32, 3462, 2020.

[131] LI, Z.; LI, Y.; LIANG, P.; ZHOU, T.; WANG, L.; XIE, R.-J. Dual-Band Luminescent Lead-Free Antimony Chloride Halides with Near-Unity Photoluminescence Quantum Efficiency, **Chemistry of Materials**, 31, 9363, 2019.

[132] SEN, S.; GOPALAN, S.; SELLAPPAN, R.; GRACE, A. N.; SONAR, P. Tin-Based Eco-Friendly Perovskites for Sustainable Future, **Advanced Energy and Sustainability Research**, 4, 2023.

[133] ZHOU, Y.; ZHAO, Y. Chemical stability and instability of inorganic halide perovskites, **Energy Environ. Sci.**, 12, 1495, 2019.

[134] FAIZAN, M.; BHAMU, K. C.; MURTAZA, G.; HE, X.; KULHARI, N.; AL-ANAZY, M. M.; KHAN, S. H. Electronic and optical properties of vacancy ordered double perovskites A_2BX_6 (A = Rb, Cs; B = Sn, Pd, Pt; and X = Cl, Br, I): a first principles study, **Sci. Rep.**, 11, 6965, 2021.

[135] HUANG, L.; LAMBRECHT, W. R. L. Lattice dynamics in perovskite halides $CsSnX_3$ with X=I, Br, Cl, **Phys. Rev. B**, 90, 195201, 2014.

[136] YIN, Y.-Y.; ZHANG, L.-X.; AN, X.-Y.; WANG, C.-J.; ZHANG, Q.-Q.; BIE, L.-J. Lead-free defective halide perovskites Cs_2SnX_6 (X = Cl, Br, I) for highly robust formaldehyde sensing at room temperature, **Scr. Mater.**, 234, 115541, 2023.

[137] ZHANG, B.; KLARBRING, J.; JI, F.; SIMAK, S. I.; ABRIKOSOV, I. A.; GAO, F.; RUDKO, G. Y.; CHEN, W. M.; BUYANOVA, I. A. Lattice Dynamics and Electron–Phonon Coupling in Double Perovskite $Cs_2NaFeCl_6$, **The Journal of Physical Chemistry C**, 127, 1908, 2023.

[138] ZENG, X.; JIANG, J.; NIU, G.; SUI, L.; ZHANG, Y.; WANG, X.; LIU, X.; CHEN, A.;

JIN, M.; YUAN, K. Physical Insights on the Thermoelectric Performance of Cs_2SnBr_6 with Ultralow Lattice Thermal Conductivity, **J. Phys. Chem. Lett.**, 13, 9736, 2022.

[139] BELESSIOTIS, G. V.; ARFANIS, M.; KALTZOGLOU, A.; LIKODIMOS, V.; RAPTIS, Y. S.; FALARAS, P.; KONTOS, A. G. Temperature effects on the vibrational properties of the Cs_2SnX_6 'defect' perovskites (X = I, Br, Cl), **Mater. Chem. Phys.**, 267, 124679, 2021.

[140] YUAN, G.; HUANG, S.; NIU, J.; QIN, S.; WU, X.; DING, H.; LU, A. Compressibility of Cs_2SnBr_6 by X-ray diffraction and Raman spectroscopy, **Solid State Commun.**, 275, 68, 2018.

[141] KALTZOGLOU, A. et al. Optical-Vibrational Properties of the Cs_2SnX_6 (X = Cl, Br, I) Defect Perovskites and Hole-Transport Efficiency in Dye-Sensitized Solar Cells, **The Journal of Physical Chemistry C**, 120, 11777, 2016.

[142] BOUNOS, G. et al. Defect Perovskites under Pressure: Structural Evolution of Cs_2SnX_6 (X = Cl, Br, I), **The Journal of Physical Chemistry C**, 122, 24004, 2018.

[143] SCHRYVER, S.; LAMICHHANE, A. Temperature-driven structural phase transitions in $CsPbBr_3$, **Solid State Commun.**, 371, 115237, 2023.

[144] YANG, Y.; ROBBINS, J. P.; EZEONU, L.; MA, Y.; SPARTA, N.; KONG, X.; STRAUF, S.; PODKOLZIN, S. G.; LEE, S. S. Probing lattice vibrations of stabilized $CsPbI_3$ polymorphs *via* low-frequency Raman spectroscopy, **J. Mater. Chem. C Mater.**, 8, 8896, 2020.

[145] MARTIN, T. P. Multiple-order Raman scattering by a localized mode, **Phys. Rev. B**, 13, 3617, 1976.

[146] XU, K.-X.; LAI, J.-M.; GAO, Y.-F.; SONG, F.; SUN, Y.-J.; TAN, P.-H.; ZHANG, J. High-order Raman scattering mediated by self-trapped exciton in halide double perovskite, **Phys. Rev. B**, 106, 085205, 2022.

[147] STEELE, J. A. et al. Giant Electron–Phonon Coupling and Deep Conduction Band Resonance in Metal Halide Double Perovskite, **ACS Nano**, 12, 8081, 2018.

[148] IARU, C. M. et al. Fröhlich interaction dominated by a single phonon mode in $CsPbBr_3$, **Nat. Commun.**, 12, 5844, 2021.

[149] LAX, M. The Franck-Condon Principle and Its Application to Crystals, **J. Chem. Phys.**, 20, 1752, 1952.

[150] PEREBEINOS, V.; ALLEN, P. B. Multiphonon resonant Raman scattering predicted in $LaMnO_3$ from the Franck-Condon process via self-trapped excitons, **Phys. Rev. B**, 64, 085118, 2001.

[151] LAI, C.-F.; CHANG, Y.-C.; TIEN, Y.-C. Stable Lead-Free Cesium Tin Halide Double-Perovskite Nanocrystals Embedded in Polydimethylsiloxane for Candlelight Light-Emitting Diodes, **ACS Appl. Nano Mater.**, 4, 1924, 2021.

[152] LEE, B.; KRENSELEWSKI, A.; BAIK, S. I.; SEIDMAN, D. N.; CHANG, R. P. H. Solution processing of air-stable molecular semiconducting iodosalts, $Cs_2SnI_{6-x}Br_x$, for potential solar cell applications, **Sustain. Energy Fuels**, 1, 710, 2017.

[153] UMEDOV, S. T.; KHADKA, D. B.; YANAGIDA, M.; GRIGORIEVA, A.; SHIRAI, Y. A-site tailoring in the vacancy-ordered double perovskite semiconductor Cs_2SnI_6 for photovoltaic application, **Solar Energy Materials and Solar Cells**, 230, 111180, 2021.

[154] WANG, Z.-Y.; CHEN, Y.; ZHANG, C.; WANG, D.; LIANG, P.; HARENG, H.; XIE, R.-J.; WANG, L. Electronic Structure and Optical Properties of Vacancy-Ordered Double Perovskites $Cs_2PdBr_xCl_{6-x}$ by First-Principles Calculation, **The Journal of Physical Chemistry C**, 124, 13310, 2020.

[155] DALPIAN, G. M.; LIU, Q.; STOUMPOS, C. C.; DOUVALIS, A. P.; BALASUBRAMANIAN, M.; KANATZIDIS, M. G.; ZUNGER, A. Changes in charge density vs changes in formal oxidation states: The case of Sn halide perovskites and their ordered vacancy analogues, **Phys. Rev. Mater.**, 1, 025401, 2017.

[156] ZHOU, J. et al. Lead-Free Perovskite Derivative $Cs_2SnCl_{6-x}Br_x$ Single Crystals for Narrowband Photodetectors, **Adv. Opt. Mater.**, 7, 2019.

[157] ZENG, X.; NIU, G.; WANG, X.; JIANG, J.; SUI, L.; ZHANG, Y.; CHEN, A.; JIN, M.; YUAN, K.; YANG, X. Enhanced carrier transport in Cs_xSnBr_y perovskite by reducing electron-phonon coupling under compressive strain, **Materials Today Physics**, 40, 101296, 2024.

[158] HOANG, M. H.; LE, D. M.; LE, T. A.; NGUYEN, Q. K.; DO, T. A. T.; HO, T. G.; MAN, M. T. Lattice dynamics and self-trapped excitons in the Cs_2SnBr_6 double perovskites, **Journal of Physics: Condensed Matter**, 36, 285901, 2024.

[159] MAKUŁA, P.; PACIA, M.; MACYK, W. How To Correctly Determine the Band Gap Energy of Modified Semiconductor Photocatalysts Based on UV–Vis Spectra, **J. Phys. Chem. Lett.**, 9, 6814, 2018.

[160] KLEIN, J.; KAMPERMANN, L.; MOCKENHAUPT, B.; BEHRENS, M.; STRUNK, J.; BACHER, G. Limitations of the Tauc Plot Method, **Adv. Funct. Mater.**, 33, 2023.

[161] GUO, B.; LUO, C.; YAN, C.; SUN, B.; LI, W.; YANG, W. Understanding Excitonic Behavior in Light Absorption and Recombination Process, **The Journal of Physical Chemistry C**, 124, 26076, 2020.

[162] CUCCO, B.; KATAN, C.; EVEN, J.; KEPENEKIAN, M.; VOLONAKIS, G. Fine Structure of Excitons in Vacancy-Ordered Halide Double Perovskites, **ACS Mater. Lett.**, 5, 52, 2023.

[163] ZHANG, Y.; FAN, B.; LIU, Y.; LI, H.; KENG, K.; FAN, J. Quasi-self-trapped Frenkel-exciton near-UV luminescence with large Stokes shift in wide-bandgap Cs_4PbCl_6 nanocrystals, **Appl. Phys. Lett.**, 112, 2018.

[164] TAN, J.; LI, D.; ZHU, J.; HAN, N.; GONG, Y.; ZHANG, Y. Self-trapped excitons in soft semiconductors, **Nanoscale**, 14, 16394, 2022.

[165] MCCUMBER, D. E.; STURGE, M. D. Linewidth and Temperature Shift of the *R* Lines in Ruby, **J. Appl. Phys.**, 34, 1682, 1963.

[166] MANNINO, G.; DERETZIS, I.; SMECCA, E.; LA MAGNA, A.; ALBERTI, A.; CERATTI, D.; CAHEN, D. Temperature-Dependent Optical Band Gap in $CsPbBr_3$, $MAPbBr_3$, and $FAPbBr_3$ Single Crystals, **J. Phys. Chem. Lett.**, 11, 2490, 2020.

[167] YU, S.; XU, J.; SHANG, X.; MA, E.; LIN, F.; ZHENG, W.; TU, D.; LI, R.; CHEN, X. Unusual Temperature Dependence of Bandgap in 2D Inorganic Lead-Halide Perovskite Nanoplatelets, **Advanced Science**, 8, 2021.

[168] ZHANG, C.; ZHANG, H.; WANG, R.; YOU, D.; WANG, W.; XU, C.; DAI, J. Exciton photoluminescence of $CsPbBr_3@SiO_2$ quantum dots and its application as a phosphor material in light-emitting devices, **Opt. Mater. Express**, 10, 1007, 2020.

[169] BIRKETT, M.; LINHART, W. M.; STONER, J.; PHILLIPS, L. J.; DUROSE, K.; ALARIA, J.; MAJOR, J. D.; KUDRAWIEC, R.; VEAL, T. D. Band gap temperature-dependence of close-space sublimation grown Sb_2Se_3 by photo-reflectance, **APL Mater.**, 6, 2018.

[170] ISIK, M.; GASANLY, N. M.; DARVISHOV, N. H.; BAGIEV, V. E. Structural and temperature-tuned band gap energy characteristics of $PbMoO_4$ single crystals, **Opt. Mater. Amst**., 126, 112210, 2022.

[171] SARSWAT, P. K.; FREE, M. L. Free, A study of energy band gap versus temperature for Cu_2ZnSnS_4 thin films, **Physica B Condens. Matter.**, 407, 108, 2012.

[172] WANG, X.; ZHANG, X.; YAN, S.; LIU, H.; ZHANG, Y. Nearly-Unity Quantum Yield and 12-Hour Afterglow from a Transparent Perovskite of $Cs_2NaScCl_6$:Tb, **Angew. Chem. Int. Ed.**, 61, 2022.

[173] ZELEWSKI, S. J. et al. Revealing the nature of photoluminescence emission in the metal-halide double perovskite $Cs_2AgBiBr_6$, **J. Mater. Chem. C Mater.**, 7, 8350 2019.

[174] PAN, F.; LI, J.; MA, X.; NIE, Y.; LIU, B.; YE, H. Free and self-trapped exciton emission in perovskite $CsPbBr_3$ microcrystals, **RSC Adv.**, 12, 1035, 2022.

[175] WU, H.; LIN, Z.; SONG, J.; ZHANG, Y.; GUO, Y.; ZHANG, W.; HUANG, R. Boosting the Self-Trapped Exciton Emission in Cs_4SnBr_6 Zero-Dimensional Perovskite via Rapid Heat Treatment, **Nanomaterials**, 13, 2259, 2023.

[176] MAUGHAN, A. E.; GANOSE, A. M.; SCANLON, D. O.; NEILSON, J. R. Perspectives and Design Principles of Vacancy-Ordered Double Perovskite Halide Semiconductors, **Chemistry of Materials**, 31, 1184, 2019.

[177] RAVIDAS, B. K.; ROY, M. K.; SAMAJDAR, D. P. Design Insights and Photovoltaic Performance Analysis of Non-Lead Inorganic $RbSnX_3$ (X = I, Br, Cl) Perovskites

through Coupled Density Functional Theory and *SCAPS-1D* Simulation Frameworks, **ACS Appl. Electron. Mater.**, 6, 5126, 2024.

[178] MA, H.; MA, Y.; Wang, H.; SLEBODNICK, C.; ALATAS, A.; URBAN, J. J.; TIAN, Z. Experimental Phonon Dispersion and Lifetimes of Tetragonal $CH_3NH_3PbI_3$ Perovskite Crystals, **J. Phys. Chem. Lett.**, 10, 1, 2019.

[179] FU, J.; RAMESH, S.; LIM, J. W. M.; SUM, T. C. Quasi-particles, and Collective Excitations in Halide Perovskites, **Chem. Rev.**, 123, 8154, 2023.

[180] ZHANG, K.-C.; SHEN, C.; ZHANG, H.-B.; LI, Y.-F.; LIU, Y. Effect of quartic anharmonicity on the carrier transport of cubic halide perovskites $CsSnI_3$ and $CsPbI_3$, **Phys. Rev. B**, 106, 235202, 2022.

[181] TORRES, D. I.; FREIRE, J. D.; KATIYAR, R. S. Lattice dynamics of crystals having R_2MX_6 structure, **Phys. Rev. B**, 56, 7763, 1997.

[182] KUZMANY, H. Solid-State Spectroscopy: An Introduction, **Springer Berlin Heidelberg, Berlin, Heidelberg,** 2009.

[183] HOFFMAN, A. E. J.; SAHA, R. A.; BORGMANS, S.; PUECH, P.; BRAECKEVELT, T.; ROEFFAERS, M. B. J.; STEELE, J. A.; HOFKENS, J.; VAN SPEYBROECK, V. Understanding the phase transition mechanism in the lead halide perovskite $CsPbBr_3$ via theoretical and experimental GIWAXS and Raman spectroscopy, **APL Mater.**, 11, 2023.

[184] PAL, D. A Comprehensive Analysis of Eco-Friendly Cs_2SnI_6 Based Tin Halide Perovskite Solar Cell through Device Modeling, **Adv. Theory Simul.**, 6, 2023.

[185] TAN, Z. et al. Tailoring the electron and hole dimensionality to achieve efficient and stable metal halide perovskite scintillators, **Nanophotonics**, 10, 2249, 2021.

[186] STONEHAM, A. M. Theory of Defects in Solids: Electronic Structure of Defects in Insulators and Semiconductors, **Oxford University Press**, 2001.

[187] SCHMIDT, T.; LISCHKA, K.; ZULEHNER, W. Excitation-power dependence of the near-band-edge photoluminescence of semiconductors, **Phys. Rev. B**, 45, 8989, 1992.

[188] LEROUX, M.; GRANDJEAN, N.; BEAUMONT, B.; NATAF, G.; SEMOND, F.; MASSIES, J.; GIBART, P. Temperature quenching of photoluminescence intensities in undoped and doped GaN, **J. Appl. Phys.**, 86, 3721, 1999.

[189] ZHOU, X.; ZHANG, Z. Electron–phonon coupling in $CsPbBr_3$, **AIP Adv.**, 10, 2020.

[190] FROST, J. M. Calculating polaron mobility in halide perovskites, **Phys. Rev. B**, 96, 195202, 2017.

[191] LANZANI, G. The Photophysics behind Photovoltaics and Photonics, First Edition, **Wiley**, 2012.

[192] VOGELSANG, H.; HUSBERG, O.; KÖHLER, U.; VON DER OSTEN, W.; MARCHETTI, A. P. Exciton self-trapping in AgCl nanocrystals, **Phys. Rev. B**, 61, 1847, 2000.

[193] LI, X.; HOFFMAN, J. M.; KANATZIDIS, M. G. The 2D Halide Perovskite Rulebook: How the Spacer Influences Everything from the Structure to Optoelectronic Device Efficiency, **Chem. Rev.**, 121, 2230, 2021.

[194] CRESP, M.; LIU, M.; RAGER, M.; ZHENG, D.; PAUPORTÉ, T. 2D Ruddlesden-Popper versus 2D Dion-Jacobson Perovskites: Of the Importance of Determining the "True" Average *n* -Value of Annealed Layers, **Adv. Funct. Mater.**, 35, 2025.

[195] GUO, S. et al. Exciton engineering of 2D Ruddlesden–Popper perovskites by synergistically tuning the intra and interlayer structures, **Nat. Commun.**, 15, 3001, 2024.

[196] WANG, C.; DONG, X.; CHEN, F.; LIU, G.; ZHENG, H. Recent progress of two-dimensional Ruddlesden–Popper perovskites in solar cells, **Mater. Chem. Front.**, 7, 5786, 2023.

[197] FU, H. Dion–Jacobson halide perovskites for photovoltaic and photodetection applications, **J. Mater. Chem. C Mater.**, 9, 6378, 2021.

[198] SMITH, M. D.; CONNOR, B. A.; KARUNADASA, H. I. Tuning the Luminescence of Layered Halide Perovskites, **Chem. Rev.**, 119, 3104, 2019.

[199] ZHANG, J.; YAN, C.; ZHAO, H.; YIN, C.; BAI, S. Modulations of Quasi-Two-Dimensional Metal Halide Perovskites toward High-Performance Blue Light-Emitting Diodes, **Adv. Funct. Mater.**, 2025.

[200] JUNG, M.-H. Broadband white light emission from one-dimensional zigzag edge-sharing perovskite, **New Journal of Chemistry**, 44, 171, 2020.

[201] RAHAMAN, M. Z.; GE, S.; LIN, C.-H.; CUI, Y.; WU, T. One-Dimensional Molecular Metal Halide Materials: Structures, Properties, and Applications, **Small Struct.**, 2, 2021.

[202] NONATO, A. et al. Strong Electron–Phonon Coupling and Lattice Dynamics in One-Dimensional $[(CH_3)_2NH_2]PbI_3$ Hybrid Perovskite, **Chemistry of Materials**, 37, 1013, 2025.

[203] YUAN, Z. et al. One-dimensional organic lead halide perovskites with efficient bluish white-light emission, **Nat. Commun.**, 8, 14051, 2017.

[204] R. Babu, J. E. Heger, T. Dutta, X. Hu, N. Pradhan, P. Müller-Buschbaum, S. Gómez-Graña, and L. Polavarapu, Chiral Molecules in Action: Chemistry of Chiral Perovskite and Perovskite-Inspired Materials, **ACS Energy Lett.**, 10, 5703, 2025.

[205] KIM, Y.-H. et al. Chiral-induced spin selectivity enables a room-temperature spin light-emitting diode, **Science**, 371, 1129, 2021.

[206] DAS, R.; HOSSAIN, M.; MAHATA, A.; SWAIN, D.; DE ANGELIS, F.; SANTRA, P. K.; SARMA, D. D. Unique Chiro-optical Properties of the Weakly-2D (R-/S-MBA)$_2$CuBr$_4$ Hybrid Material, **ACS Mater. Lett.**, 5, 1556, 2023.

[207] CHEN, C.; GAO, L.; GAO, W.; GE, C.; DU, X.; LI, Z.; YANG, Y.; NIU, G.; TANG, J. Circularly polarized light detection using chiral hybrid perovskite, **Nat. Commun.**, 10, 1927, 2019.

[208] BLOOM, B. P.; PALTIEL, Y.; NAAMAN, R.; WALDECK, D. H. Waldeck, Chiral Induced Spin Selectivity, **Chem. Rev.**, 124, 1950, 2024.

[209] LONG, G. et al. Spin control in reduced-dimensional chiral perovskites, **Nat. Photonics**, 12, 528, 2018.

[210] SCALON, L.; NEW, A.; GE, Z.; MONDAL, N.; CAMPOS, R. D.; QUARTI, C.; BELJONNE, D.; NOGUEIRA, A. F.; BAKULIN, A. A.; VAYNZOF, Y. Understanding and Controlling the Photoluminescence Line Shapes of 2D Perovskites with Chiral Methylbenzylammonium-Based Cations, **Chemistry of Materials**, 36, 4331, 2024.

[211] LONG, G.; SABATINI, R.; SAIDAMINOV, M. I.; LAKHWANI, G.; RASMITA, A.; LIU, X.; SARGENT, E. H.; GAO, W. Chiral-perovskite optoelectronics, **Nat. Rev. Mater.**, 5, 423, 2020.

[212] SON, J. et al. Unraveling chirality transfer mechanism by structural isomer-derived hydrogen bonding interaction in 2D chiral perovskite, **Nat. Commun.**, 14, 3124, 2023.

[213] ABHERVÉ, A.; ALLAIN, M.; MERCIER, N. Perovskite versus Nonperovskite: Modulating the Nature and Optical Properties of One-Dimensional Chiral Lead–Bromide Networks, **Inorg. Chem.**, 63, 5916, 2024.

[214] LI, M. et al. Chiral Ligand-Induced Structural Transformation of Low-Dimensional Hybrid Perovskite for Circularly Polarized Photodetection, **Chemistry of Materials**, 34, 2955, 2022.

[215] YANG, L.-S.; LIN, E.-C.; HUA, Y.-H.; HSU, C.-A.; CHIU, H.-Z.; LO, P.-H.; CHAO, Y.-C. Circularly Polarized Photoluminescence of Chiral 2D Halide Perovskites at Room Temperature, **ACS Appl. Mater. Interfaces**, 14, 54090, 2022.

[216] DAN, S.; PARAMANIK, S.; PAL, A. J. Why Mixed Halides in 2D Chiral Perovskites Weaken Chirality-Induced Spin Selectivity, **ACS Nano**, 18, 35644, 2024.

[217] BILLING, D. G.; LEMMERER, A. Synthesis and crystal structures of inorganic–organic hybrids incorporating an aromatic amine with a chiral functional group, **CrystEngComm**, 8, 686, 2006.

[218] DANG, Y.; LIU, X.; SUN, Y.; SONG, J.; HU, W.; TAO, X. Bulk Chiral Halide Perovskite Single Crystals for Active Circular Dichroism and Circularly Polarized Luminescence, **J. Phys. Chem. Lett.**, 11, 1689, 2020.

[219] MA, J.; FANG, C.; CHEN, C.; JIN, L.; WANG, J.; WANG, S.; TANG, J.; LI, D. Chiral 2D Perovskites with a High Degree of Circularly Polarized Photoluminescence, **ACS Nano**, 13, 3659, 2019.

[220] AHN, J.; MA, S.; KIM, J.-Y.; KYHM, J.; YANG, W.; LIM, J. A.; KOTOV, N. A.; MOON, J. Chiral 2D Organic Inorganic Hybrid Perovskite with Circular Dichroism Tunable Over Wide Wavelength Range, **J. Am. Chem. Soc.**, 142, 4206, 2020.

[221] SHEIKH, T.; MAQBOOL, S.; RAJPUT, P. K.; MANDAL, P.; NAG, A. Effect of chirality on the optical properties of layered hybrid perovskite R- and S-α-methylbenzylammonium lead iodide, **Chemical Communications**, 58, 7650, 2022.

[222] ZHOU, Y.; LI, W.; CHEN, X.; LI, X.-Z.; WANG, X.-J.; BAI, B.; CHEN, Y.; FANG, H.-H. Efficient second-order nonlinear response and upconversion emission from a wide-bandgap quasi-1D lead bromide perovskite, **J. Mater. Chem. C Mater.**, 10, 15424 ,2022.

[223] MANOUSAKIS, E. Towards understanding the electronic structure of the simpler members of two-dimensional halide-perovskites, **Phys. Rev. B**, 108, 045130, 2023.

[224] TAO, S.; SCHMIDT, I.; BROCKS, G.; JIANG, J.; TRANCA, I.; MEERHOLZ, K.; OLTHOF, S. Absolute energy level positions in tin- and lead-based halide perovskites, **Nat. Commun.**, 10, 2560, 2019.

[225] BJÖRKMAN, T.; GULANS, A.; KRASHENINNIKOV, A. V.; NIEMINEN, R. M. van der Waals Bonding in Layered Compounds from Advanced Density-Functional First-Principles Calculations, **Phys. Rev. Lett.**, 108, 235502, 2012.

[226] KLIMEŠ, J.; BOWLER, D. R.; MICHAELIDES, A. Van der Waals density functionals applied to solids, **Phys. Rev. B**, 83, 195131, 2011.

[227] KOHN, W.; MEIR, Y.; MAKAROV, D. E. van der Waals Energies in Density Functional Theory, **Phys. Rev. Lett.**, 80, 4153, 1998.

[228] ACOSTA, C. M.; OGOSHI, E. ; FAZZIO, A.; DALPIAN, G. M.; ZUNGER, A. The Rashba Scale: Emergence of Band Anti-crossing as a Design Principle for Materials with Large Rashba Coefficient, **Matter**, 3, 145, 2020.

[229] ZHOU, C. et al. Photoluminescence spectral broadening, chirality transfer and amplification of chiral perovskite materials (R-X-*p*-mBZA)$_2$PbBr$_4$ (X = H, F, Cl, Br) regulated by van der Waals and halogen atoms interactions, **Physical Chemistry Chemical Physics**, 22, 17299, 2020.

[230] YANG, C.; WEI, Q.; GONG, Y.; LONG, M.; ZHOU, G.; XING, G.; WU, B. Correlated Self-Trapped Excitons and Free Excitons with Intermediate Exciton–Phonon Coupling in 2D Mixed-Halide Perovskites, **J. Phys. Chem. Lett.**, 14, 10046, 2023.

[231] GUO, S. et al. Exciton engineering of 2D Ruddlesden–Popper perovskites by synergistically tuning the intra and interlayer structures, **Nat. Commun.**, 15, 3001, 2024.

[232] LYU, D.; MIAO, Y.; LI, B.; XIAO, Z.; WU, X.; HU, X.; JIANG, X.-F.; XU, Q.-H. Dual Blue Emission in Ruddlesden–Popper Lead-Bromide Perovskites Induced by Photon Recycling, **The Journal of Physical Chemistry C**, 125, 18308, 2021.

[233] SHEIKH, T.; SHINDE, A.; MAHAMUNI, S.; NAG, A. Possible Dual Bandgap in $(C_4H_9NH_3)_2PbI_4$ 2D Layered Perovskite: Single-Crystal and Exfoliated Few-Layer, **ACS Energy Lett.**, 3, 2940, 2018.

[234] LAFALCE, E.; AMERLING, E.; YU, Z.-G.; SERCEL, P. C.; WHITTAKER-BROOKS, L.; VARDENY, Z. V. Rashba splitting in organic–inorganic lead–halide perovskites revealed through two-photon absorption spectroscopy, **Nat. Commun.**, 13, 483, 2022.

[235] HAUTZINGER, M. P.; MIHALYI-KOCH, W.; JIN, S. A-Site Cation Chemistry in Halide Perovskites, **Chemistry of Materials**, 36, 10408, 2024.

[236] MA, Z.; LI, F.; SUI, L.; SHI, Y.; FU, R.; YUAN, K.; GAXO, G.; ZOU, B. Tunable Color Temperatures and Emission Enhancement in 1D Halide Perovskites under High Pressure, **Adv. Opt. Mater.**, 8, 2020.

[237] JIN, J.; QUAN, L. N.; GAO, M.; CHEN, C.; GUO, P.; YANG, P. Octahedral Distortion and Excitonic Behavior of $Cs_3Bi_2Br_9$ Halide Perovskite at Low Temperature, **The Journal of Physical Chemistry C**, 127, 3523, 2023.

[238] ZHANG, L.; WU, L.; WANG, K.; ZOU, B. Pressure-Induced Broadband Emission of 2D Organic–Inorganic Hybrid Perovskite $(C_6H_5C_2H_4NH_3)_2PbBr_4$, **Advanced Science**, 6, 2019.

[239] GAO, F.-F. et al. Unusual Pressure-Induced Self-Trapped Exciton to Free Exciton Transfer in Chiral 2D Lead Bromide Perovskites, **ACS Nano**, 18, 3251, 2024.